NMR studies of some styrene-based diblock copolymers

Steven Gerard Breen

NMR STUDIES OF SOME STYRENE-BASED DIBLOCK COPOLYMERS

submitted by
Steven Gerard Breen

for the degree of Master of Science
at the University of Durham
Department of Chemistry

1996

To Michael
who will always be in my thoughts.

ACKNOWLEDGMENTS

I would like to acknowledge Robin Harris for his continued supervision throughout my time at Durham University. I also acknowledge EPSRC and the IRC for continued financial support. A special thank you goes to Barry Say and Alan Kenwright for their input on proton relaxation studies and to Ulrich Scheller for his valuable assistance in the WISE two-dimensional experiments. May I also thank Tom Kiff, from the IRC, for his valuable knowledge of synthesis of polymers and Randal Richards for his expertise in the field of polymer statistics.

Finally, I would like to thank all the solid-state NMR group for their discussions and assistance, both on practical and theoretical aspects of solid-state NMR.

CONTENTS PAGE

Abstract

A selection of styrene-based diblock copolymers were investigated using the technique known as Nuclear Magnetic Resonance spectroscopy (NMR) in both the solid- and solution-state. These diblock copolymers undergo phase separation due to the incompatibility of the glassy and rubbery blocks and this was to be detected using NMR.

The microstructure of these copolymers was analysed using solution-state ^{13}C and ^{1}H NMR. An extensive study of the relaxation characteristics of these polymers was undertaken in the solid-state to try and understand the nature of molecular motions that occur in these polymers before and after phase separation. Due to the large number of variables involved a number of techniques were used to analyse the consistency of the data obtained.

The Goldman-Shen experiment was used to monitor the process of spin-diffusion, which is an indicator of the distances that nuclear interactions can occur, and was to be used as an indicator of the degree of phase separation that can occur in these polymers.

The WISE heteronuclear correlation experiment was used to try and correlate the mobilities of proton nuclei in differing blocks to individual resonances of chemically distinct carbon nuclei and ultimately to monitor the process of spin-diffusion whilst understanding the competing relaxation processes that occur during measurement.

1 INTRODUCTION

1.1 Block Copolymers: Uses and Characteristics

Block copolymers are used extensively in industry and are found in abundance in everyday life. They are used industrially for their processability and performance as thermoplastic elastomers, pressure-sensitive hot-melt adhesives, viscosity stabilizers for engine oils and so on.

Partially incompatible block copolymers are known to undergo phase transitions at specific temperatures between disordered and ordered states. In the disordered state their melt viscosities are low, so they are easily processable and interfacial wetting between adhesives (block copolymers) and substrates is favourable. In the ordered state, they have a high viscosity (characterized by non-Newtonian flow behaviour) and so are difficult to process. The dispersed domains of rigid blocks act as reinforcing fillers for the elastomer phase, thus improving the impact strength of elastomers and adhesives. When incorporated into oils the viscosity changes of the oil at working (elevated) and resting temperatures are counterbalanced by the mixing and non-mixing of the block copolymer as it undergoes phase changes within the oil.

The order-disorder transition of block copolymers is a thermodynamic transition balancing the enthalpic and entropic interactions of the blocks of the copolymer. The incompatibility of the blocks favours phase separation - the enthalpic driving force - but the physical constraint of the block junctions only allows phase separation to occur up to an extended chain conformation. This extended chain conformation results in a loss of the degrees of freedom of the polymer segments and hence gives rise to a decrease in the entropy of the system. Due to the counter effects of entropy and enthalpy, neither can be easily studied in isolation, so the Gibbs free energy of the system is a good indicator of the dynamic processes occurring during phase separation.

The investigation into the phenomenon of microdomain separation and morphological ordering in block copolymers has been pursued for a number of years.

The principle analytical tools that have been used to probe these systems have been SAXS (Small Angle X-ray Scattering), TEM (Transmission Electron Microscopy) and SANS (Small Angle Neutron Scattering). Each of these techniques has its advantages but unfortunately also has its inherent disadvantages.

SAXS and SANS may not have the resolution needed for analysis of the phenomenon of microdomain separation. TEM also requires the use of osmium tetroxide as a staining agent to distinguish between the two blocks, which in turn affects the equilibrium of the domains and thus causes changes in the size of the microdomains.

Solid-state NMR has the advantages of being non-destructive (as with SAXS and SANS), has the required spatial resolution needed for determination of the magnitude of microdomains, and has no effect on the equilibrium position of the microdomains. However, the major disadvantage of solid-state NMR is that the detection of the size of microdomains is made indirectly through the magnitude of homonuclear and heteronuclear dipolar interactions that occur between neighbouring nuclei.

1.2 The Principles Behind Solid-state Nuclear Magnetic Resonance[1]

In solution-state NMR the medium's mobility causes the nuclear interactions present to be isotropic. However, in solid-state NMR these interactions are not averaged but are orientation-dependent. The Hamiltonian describing the NMR experiment is given by a sum of interaction Hamiltonians-

$$\mathcal{H}_{NMR}=\mathcal{H}_Z+\mathcal{H}_{RF}+\mathcal{H}_S+\mathcal{H}_{SR}+\mathcal{H}_D+\mathcal{H}_J+\mathcal{H}_Q \qquad \text{Eqn. 1.1}$$

The Zeeman ($\mathcal{H}_Z$) and radio frequency ($\mathcal{H}_{RF}$) terms represent the nuclear spins' interactions with the applied static magnetic field (B_0) and radiofrequency magnetic fields, respectively. The shielding ($\mathcal{H}_S$), spin-rotation ($\mathcal{H}_{SR}$), dipolar ($\mathcal{H}_D$), indirect coupling ($\mathcal{H}_J$) and quadrupolar ($\mathcal{H}_Q$) interactions are of interest, but the spin-rotation

interaction in the solid state is almost insignificant. In addition, since these polymer systems contain only ^{13}C and ^{1}H - both with nuclear spins of I=1/2 - then the quadrupolar interaction is not applicable.

1.2.1 The Shielding Interaction

The Shielding Hamiltonian ($\mathcal{H}_S$) - this results from shielding of nuclei by their surrounding electrons. If their distribution is not symmetrical around a given nucleus then this results in anisotropic shielding (designated by the tensor - σ). For example - chloroform-

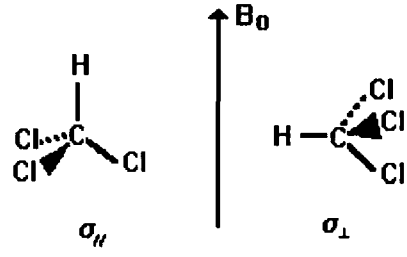

Figure 1.1 Shielding tensors for a chloroform molecule.

Thus, when the molecular axis is at an angle θ to B_0 then the effective shielding is described as-

$$\sigma_{ZZ} = 1/3(\sigma_{/\!/} + 2\sigma_{\perp}) + 1/3(3\cos^2\theta - 1)(\sigma_{/\!/} - \sigma_{\perp}) \qquad \text{Eqn. 1.2}$$

where the z-direction is parallel to the static magnetic field and $1/3(\sigma_{/\!/} + 2\sigma_{\perp})$ is the isotropic average tensor. Now for a random powder pattern (as in the diblock copolymers) all values of θ are allowed. This results in a shielding anisotropy powder-pattern spectrum-

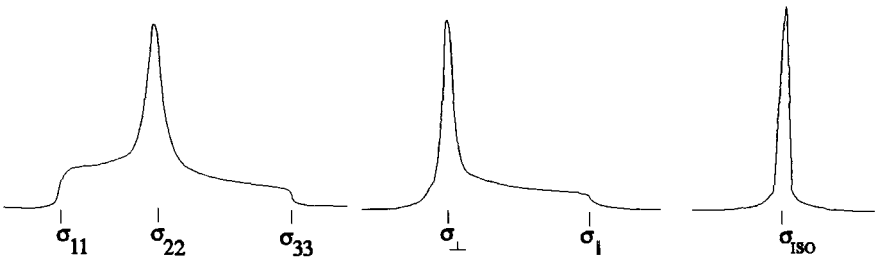

Asymmetric pattern Axially symmetric pattern Isotropic pattern

Figure 1.2 Shielding anisotropy powder patterns.

To overcome this broadening, the sample under investigation is rotated at the magic angle, for which $(3\cos^2\theta - 1) = 0$, i.e. $\theta = 54.77°$, so that the effective shielding tensor reaches its isotropic average value.

1.2.2 The Dipolar Interaction $(\%_D)^2$

Classically, the dipolar interaction between two magnetic dipole moments is given by

$$U_D = \left\{ \frac{\mu_1 . \mu_2}{r^3} - \frac{3(\mu_1 . r)(\mu_2 . r)}{r^5} \right\} \frac{\mu_0}{4\pi} \qquad \text{Eqn. 1.3}$$

where μ_0 is the permeability constant and μ_1 and μ_2 are the two magnetic dipole moments, separated by a distance r. However, in quantum mechanical terms the dipole moments are described in terms of operators to give the alphabet expansion-

$$\hat{H}_D = r^{-3}\gamma_1\gamma_2\hbar^2[A + B + C + D + E + F]\mu_0 / 4\pi \qquad \text{Eqn. 1.4}$$

where g is the magnetogyric ratio for a particular nucleus. The letters in the expansion describe interactions of step up/down ladder operators. These operators represent the

number of spin changes that occur between two nuclei and the static magnetic field and are directly related to nuclear spin transitions-

$$A = \hat{I}_{1z}\hat{I}_{2z}\left(1-3\cos^2\theta\right) \qquad \text{secular term} \qquad \text{Eqn. 1.5}$$

$$B = -\tfrac{1}{4}\left[\hat{I}_{1+}\hat{I}_{2-} + \hat{I}_{1-}\hat{I}_{2+}\right]\left(1-3\cos^2\theta\right) \qquad \text{flip-flop term} \qquad \text{Eqn. 1.6}$$

These two terms represent the common interactions that occur within polymer systems. The other terms represent single- and double-quantum transitions. The flip-flop term is important in that it is the route through which spin-diffusion operates (spin-diffusion will be described in more detail later in this chapter). This flip-flop term is non-secular (no energy change) but with homonuclear dipolar interactions (adjacent protons in polymer systems) then this flip-flop term becomes secular (affects nuclear energies)[3].

1.3 Nuclear Relaxation

There are three main types of relaxation that are evident in NMR-

1.3.1 T_1 - Spin-lattice Relaxation

T_1 - this represents the spin-lattice (or longitudinal) relaxation process. It is a time constant that governs the decay of the bulk magnetisation along the z-axis, i.e. the applied magnetic field axis. Relaxation to the lattice is achieved by non-radiative processes such as modulation of local magnetic fields by molecular motion of the proper frequency (i.e. of the order of tens to hundreds of MHz). This relaxation is at its most efficient when the frequencies of these motions are at the Larmor frequency - this is the precessional frequency with which the bulk magnetisation evolves as a result of a 90° pulse of radiofrequency.

Measurement of T_1 is usually achieved by the Inversion-recovery sequence. This uses a 180° pulse to leave the magnetisation along the negative z-axis followed by a progressingly incremented time - tau - before the application of a 90° pulse to push the magnetisation into the positive y- or detection-axis. If the magnetisation has had sufficient time to relax into the positive z-axis then application of the 90° pulse pushes the magnetisation into the positive y-axis so that it is detected as a positive signal. The point in which the signal passes from the negative to the positive axes is known as the null-point, and a quick approximation of the T_1 value can be obtained using the equation-

$$\text{null-time} = T_1 \ln 2 \qquad \text{Eqn. 1.6}$$

However, the full equation describing the rate of decay of the magnetisation to the lattice is of simple first-order type-[4]

$$\ln(M_\infty - M_t) = \ln(M_\infty - M_0) - \tau/T_1 \qquad \text{Eqn. 1.7}$$

M_∞ is the magnetisation at time = ∞, M_t = the magnetisation at time tau, M_0 = the magnetisation at time zero and τ is the delay between the 180° and 90° pulses. In the approximation $\ln[(M_\infty - M_0)/(M_\infty - M_t)] = \ln 2$. This assumes that both the initial and final signals, detected, represent accurately the initial (M_0) and final (M_∞) magnetisations so that the null-point is assumed to be exactly mid-way between the two extremes. However, due to the fact that T_1 can be of the order of hours the time needed between each acquired point is inordinately long so that M_∞ may not be achieved.

Another method to measure T_1 is a sequence called the saturation-recovery method. This consists of an initial 90° nutation pulse followed by a series of successive 90° pulses in order to cause dephasing of the magnetisation to leave none of the original magnetisation. The magnetisation is left to relax to the positive z-direction but the system does not start its relaxation from a state of thermal equilibrium so that the

next acquired point need not be taken after the delay of $5T_1$ as in the inversion-recovery sequence. The limitation of this sequence is that $T_1 >> T_2$.

1.3.2 T_2 - Spin-spin Relaxation

T_2 - is the spin-spin (or transverse) relaxation time. It is the rate constant for the decay of the bulk magnetisation in the xy-plane. It represents entropic relaxation or the randomisation of spins resulting in the spins becoming out of phase with respect to each other. The time taken for this dephasing directly affects the time-and frequency-domains, i.e. this is seen as variable decay in the time-domain and variable line-width - (peak width at half height: $\nu_{1/2} = (\pi T_2)^{-1}$) - in the frequency domain, to give the well-known Lorentzian lineshape as seen in solution-state spectra. However, in solid-state spectroscopy the average lineshape is generally Gaussian and can even be somewhere in between the two lineshapes! The range of motions T_2 probes is of the magnitude of Hz so this can probe slow motions, but in some systems more information is obtained using $T_{1\rho}$.

A further complication is that in the frequency-domain the individual resonances for magnetically inequivalent nuclei are generally of differing lineshapes - varying between Gaussian and Lorentzian statistics - so exponential decay behaviour cannot be assumed. This is investigated further in chapter 3.

1.3.3 $T_{1\rho}$ - Rotating-frame Relaxation

$T_{1\rho}$ - this is called the spin-locked or rotating-frame relaxation time. This describes the decay of the magnetisation whilst under the influence of a second magnetic field (~40 kHz in magnitude) usually along the detection axis. This is also used to probe the correlation time (time for one rotation of a radian for a molecule under the influence of the applied magnetic field), which varies for differing chains within heterogeneous polymers - denoted τ_c. The motions of importance for $T_{1\rho}$ are of

the order of tens of kHz. The equation describing $T_{1\rho}$, as part of a cross-polarisation experiment, is defined as-[3]

$$M(t) = M_0\lambda^{-1}\left[1-\exp\left(-\lambda t / T_{CH}\right)\right]\exp(-t / T_{1\rho}^{H}) \qquad \text{Eqn. 1.8}$$

$$\text{Where } \lambda \equiv 1 + T_{CH} / T_{1\rho}^{C'} - T_{CH} / T_{1\rho}^{H} \qquad \text{Eqn. 1.9}$$

T_{CH} = time for cross-polarisation from protons to carbons

$T_{1\rho}^{C'}$ = spin-lock relaxation time for carbon nuclei - occurs simultaneously as $T_{1\rho}^{H}$ but is large in comparison to $T_{1\rho}^{H}$ (the superscript H will be omitted in this study, which is only concerned with proton $T_{1\rho}$).

Using an approximation where $T_{CH}/T_{1\rho}^{C'} = 0$, since $T_{1\rho}^{C'} >> T_{CH}$ then the equation becomes-

$$M(t) = M_0(1 - T_{CH} / T_{1\rho}^{H})^{-1}\left[1-\exp\left(-(1 - T_{CH} / T_{1\rho}^{H})t / T_{CH}\right)\right]\exp(-t / T_{1\rho}^{H}) \qquad \text{Eqn. 1.10}$$

This can subsequently be used to fit experiments of CPMAS (Cross-polarised Magic Angle Spinning) using variable contact-times between the proton and carbon channels. However, this relaxation time can also be analysed using direct detection of proton nuclei. Since there may be a range of correlation times for heterogeneous samples then a number of exponential decay components can be fitted to give an overall equation describing a set of i detectable motions, e.g.-

$$M_t = \sum_i M_{0,i}\exp\left(\frac{-t}{T_{1\rho}}\right) \qquad \text{Eqn. 1.11}$$

1.3.4 Cross-polarisation[3,4]

When protons are spin-locked they are said to have a low spin-temperature (in Boltzmann distribution terms - the higher Zeeman energy levels are less populated), but a high heat capacity (relative to Curie's Law), in comparison with the carbons. Thus, the carbons can transfer spin-temperature to the protons (the energy gap between the carbon Zeeman energy levels is the same as the energy gaps for the proton nuclei hence the creation of carbon magnetisation through the transfer of energy from the proton to the carbon reservoirs so causing the higher energy states to be populated). This results in the creation of an overall bulk magnetisation for the carbon nuclei. The system can then be investigated by observing the decay of the carbon magnetisation. An important point to note is that the maximum signal achieved is set by the Hartmann-Hahn condition because it allows transfer of magnetisation induced by the flip-flop term whilst being energy-conserving in the rotating frame, i.e.-

$$\gamma_H B_{1H} = \gamma_C B_{1C} \qquad \text{Eqn. 1.12}$$

γ is the gyromagnetic ratio, which is proportional to the Zeeman splitting energy, and B_1 is the spin-locking RF field strength.

Overall, the relaxation times T_1, $T_{1\rho}$ and T_2 respond to correlation times or motions of frequency in the regions - 100's of MHz, 10's of kHz and ca. zero respectively. In the solution-state these relaxation times are all equal - called the extreme narrowing limit - but for rigid solids they are in the order $T_1 > T_{1\rho} >> T_2$, with values in the region of ~s, ~ms and ~μs. In heterogeneous polymers, because of the variation of lineshapes and the ambiguity in defining lineshape, then only T_1 and $T_{1\rho}$ are of any distinct significance.

An additional complication is in the fact that the relaxation times T_1 and $T_{1\rho}$ are usually not just single-exponential functions and generally cannot be readily assigned to individual components within heterogeneous polymer systems - such as the two 'pure'

regions and the interface within phase-separated copolymers, as well as crystalline and amorphous regions for homopolymers.[5,6]

1.3.5 Spin-diffusion[3, 4, 8-10]

An important model used in the analysis of heterogeneous polymer systems has been the "spin-diffusion" model, which makes use of the aforementioned secular/non-secular (in homonuclear/heteronuclear dipolar interactions, respectively) flip-flop term in the alphabet expansion to calculate the probability and rate of spin-diffusion to result in an indirect measurement of the size of microdomains within heterogeneous block copolymers. Spin-diffusion is greatly influenced by the spatial mixing of the polymeric chains, and so is a measure of homogeneity. In cross-polarisation the carbon magnetisation follows the decrease of proton polarisation via the $T_{1\rho}^{H}$ process. If chains are intimately mixed then rapid spin-diffusion yields a single value for $T_{1\rho}^{H}$.

Only two extremes of spin-diffusion have been fully studied theoretically-

'Slow spin-diffusion' allowing the observation of intrinsic relaxation times.
'Fast spin-diffusion' giving the observation of population weighted averages for relaxation-

$$R_{(obs)} = \frac{\sum(P_i R_i)}{\sum P_i} \qquad \text{Eqn. 1.13}$$

P_i is the population of region i and R_i is the relaxation rate (= $1/T_1$) for region i.

The Fick's diffusion equation to be solved is-

$$\dot{m}(r,t) = D\nabla^2 m(r,t) \qquad \text{Eqn. 1.14}$$

where D is the diffusion constant (units of $cm^2\ s^{-1}$) and m(r, t) is the local magnetisation density. Solutions are expressed in terms of a response function R(t), which measures the recovery of magnetisation of the crystalline domain (since this domain is the region where magnetisation is usually lost and recovered rapidly as a result of spin-diffusion). From Goldman-Shen[11] experimental data-

$$R(t) = 1 - [M_c(t) - M_c(t \rightarrow \infty)]/[M_c(t = 0) - M_c(t \rightarrow \infty)] \qquad \text{Eqn. 1.15}$$

Where M_c is the magnetisation from the crystalline region.

With appropriate boundary conditions and Poisson distribution for spacing between domains, then the response function has been solved for one, two and three dimensions. $\bar{b}$ - the average domain dimension is the parameter that describes the dimensionality of the situation, e.g. for one-dimensional diffusion $\bar{b} = b_x << b_y, b_z$ - which is the situation apparent in a lamellar morphology (infinitely long sheets of finite thickness).

One-dimensional (lamellar)-

$$R(t) = 1 - \phi(t) \qquad \text{Eqn. 1.16}$$

$$= (2/\pi^{1/2})(Dt/\bar{b}^2)^{1/2} \qquad \text{for } t << \bar{b}^2/D \qquad \text{Eqn. 1.17}$$

$$= 1 - \pi^{-1/2}(\bar{b}^2/Dt)^{1/2} \qquad t >> \bar{b}^2/D \qquad \text{Eqn. 1.18}$$

Two-dimensional (rod-like morphology)-

$$R(t) = 1 - \phi(t)^2 \qquad \text{Eqn. 1.19}$$

$$= (4\pi^{-1/2})(Dt/\bar{b}^2)^{1/2} \qquad \text{for } t << \bar{b}^2/D \qquad \text{Eqn. 1.20}$$

$$= 1 - (\bar{b}^2/\pi Dt) \qquad t >> \bar{b}^2/D \qquad \text{Eqn. 1.21}$$

Three-dimensional (sphere/cubic morphology)-

$$R(t) = 1 - \phi(t)^3 \qquad \text{Eqn. 1.22}$$

$$= 6\pi^{-1/2}(Dt/\bar{b}^2)^{1/2} \qquad \text{for } t << \bar{b}^2/D \qquad \text{Eqn. 1.23}$$

$$= 1 - (\bar{b}^2/\pi Dt)^{3/2} \qquad \text{for } t >> \bar{b}^2/D \qquad \text{Eqn. 1.24}$$

However, this model does not take into account relaxation effects and uses the assumption that the diffusion rates between each region are the same. In diblock copolymers this is not a valid assumption. A better model is the one used by Booth and Packer[8]. The basis for their model is-

$$\dot{M}(r,t) = \nabla\{D(r)\nabla M(r,t)\} + R_j(r)\Delta M(r,t) \qquad \text{Eqn. 1.25}$$

where D(r) is an isotropic spin-diffusion coefficient. $R_j(r)$ is the spatially dependent relaxation rate (j = 1, 1ρ, etc.) and $\Delta M = M^{eq} - M(r, t)$, the instantaneous deviation of the nuclear magnetisation from its equilibrium value M^{eq} (= M_0 for j = 1 and = 0 for j = 1ρ). The solution of this differential equation involving six physically independent quantities gives two roots which define average criteria for 'fast' and 'slow' exchange (diffusion) conditions relative to the relaxation rate difference between the two domains (Δk) and a parameter that scales the efficiency of diffusion.

1.4 Thermodynamic Characteristics of Phase-Separated Block Copolymers[12-22]

The mechanical characteristics of these copolymers are that they consist of a glassy phase - namely polystyrene - and an elastomeric phase - namely polyisoprene/polybutadiene. The integration of both these polymers within the copolymer helps utilize the rigidity and hardness of the styrene and the toughness (elasticity) of the rubbery polydiene phase. These polymers have only been recently accessible to study due to the relatively recent advances in polymerization techniques - especially anionic and cationic living polymerization.

The phase behaviour of these A/B type diblock copolymers is simply controlled by the degree of polymerization (DP or N), the architectural constraints (n - number of blocks in the n-block copolymer), the composition of the copolymer (f - volume fraction) and the A-B segment-segment interaction parameter - χ. N - the degree of polymerization, and n both influence the translational and configurational entropy of the copolymer, but χ is determined by the type of monomer - A and B.

Lowering the temperature of the system (from elevated temperatures above the melt point) causes the interaction parameter to increase, thus resulting in the decrease in the number of AB monomer contacts. This leads to block ordering and microphase-separation, and vice versa for higher temperatures. The enthalpy and entropy are governed by N^{-1} and χ, respectively, so χN dictates the phase state. For copolymers of equal volume fraction ($f = 0.5$), then the transition to an ordered state occurs if $\chi N/n \sim 10$.

As $\chi N/n \rightarrow 0$, then there is an order - disorder transition. Near this transition, copolymers are in their unperturbed state, and the microdomain period therein scales as $\sqrt{N}$, so the ordered composition cross-section profile is approximately sinusoidal - called the Weak Segregation Limit (WSL). However, when $\chi N >> 10$ then this leads to the Strong Segregation Limit (SSL) where there are narrow interfaces of widths of $\chi^{-1/2}$ and quite separate microdomains of pure A and B polymers. This is advantageous to

this study in that it will assist in differentiating between the two polymer components using NMR.

The interaction energy of A and B is evident only at the interface because of the constraint of incompressibility of the polymer chains and the drop in entropy from the ensuing extended chain conformation. These thermodynamic forces lead to perturbed chain conformations and thus microdomain dimensions (periods). These classifications of segregation limits do break down in the order-disorder transition regions but it is still viable to treat the system with the Weak Segregation Limit.

As the volume fraction of the styrene or diene component is changed then seven individually distinct equilibrium morphologies formed by order-disorder transitions have been found. These include - spheres, cylinders, lamellae, OBDD (Ordered Bicontinuous Double Diamond) and Gyroid structures. It is the last two morphologies that will be the centre of attention of this research. Evidence of these distinct morphologies comes from transmission electron microscopy and small angle X-ray/Neutron scattering. To date, it is the SSL theory that has been applied to the OBDD structure (model showing dramatic drops in the copolymer's entropy from the extended chain conformation in the 'pure monomer' phases) and the WSL for the gyroid, hexagonal and BCC (body-centred-cubic) conformations.

1.5 Comparison Between The OBDD and Gyroid Morphologies[21-27]

Studies into the effect of annealing temperature and duration were completed on varying weight-fractions of polystyrene-polydiene and investigated using TEM - transmission electron microscopy - and SAXS - small angle X-ray scattering. Summarizing the results showed that a new microdomain morphology had been discovered and given the title - The Gyroid Morphology (from the mathematical G-minimal constant thickness surface model used to pictorially interpret the scattering data whilst agreeing with mean curvature continuous models and thermodynamics). It is

believed to consist of a network of interpenetrating bicontinuous 'rods' as with the OBDD structure but from scattering data it was shown to have the same point group but different space group - it did not have cubic symmetry but had a twist/gyre between repeat units.

One anomalous result was that at the weight fraction for the appearance of the OBDD structure from recent findings showed that this morphology was not obtainable - was this down to mis-assignment of the morphology as OBDD instead of gyroid?

Overall, the repeat spacing of the lamellar unit cell was believed to be 212 Å with the diene having a 140 Å and styrene having a 72 Å thickness. These are believed to be compressed compared to their calculated radii of gyration, so elongation perpendicular to the interface occurs, hence the gyroid structure. The change from lamellar to gyroid involves 'relaxation' of the entropic polystyrene chains (springs) to form a slightly curved interface - the gyroid. The calculated dimensions for the styrene moiety were 50 Å to 80 Å.

1.6 References

1 Harris R. K., 'Nuclear Magnetic Resonance Spectroscopy', 2nd edition, Pub. Longmann, 1987.

2 Abragam A., 'Principles of Nuclear Magnetism', Oxford University Press, Oxford, 1961.

3 Komoroski R. A., 'High Resolution NMR Spectroscopy of Synthetic Polymers in Bulk', Pub. VCH, 1986.

4 Kenwright A. M., Say B. J., 'NMR Spectroscopy in Polymers', Chap.7 - 'Solid-state Proton NMR Studies of Polymers', Pub. Blackie Academic & Professional, 1994.

5 Assink R. A., Wilkes G. L., 'Pulsed Nuclear Magnetic Resonance For Studying Phase Separation in Block and Segmented Copolymers', *Polym. Eng. Sci.*, 1977, Vol. **17**, P606.

6 Tanaka H., Nishi T., 'Study of Block Copolymer Interface by Pulsed NMR', *J. Chem. Phys.* Vol. **82**, (9), 1985.

7 Packer K. J., Pope J. M., Yeung R. R., 'The Effects of Morphology on ^{1}H NMR Spectra & Relaxation in Semicrystalline Polyolefins', *J. Poly. Sc. Polym. Phys.*, 1984, Vol. **22**, P589.

8 Booth A. D., Packer K. J., 'Magnetic Spin Lattice Relaxation in the Presence of Spin-diffusion. The one-dimensional, two-region system', *Mol. Phys.*, 1987, Vol. **62**, 4, P811.

9 Kenwright A. M., Packer K. J., Say B. J., 'Numerical Simulations of the Effects of Spin-Diffusion on NMR Spin-Lattice Relaxation in Semicrystalline Polymers', *J. Mag. Res.*, 1986, Vol. **69**, P426.

10 Tanka H., Nishi T., 'Spin Diffusion in Block Copolymers as Studied by Pulsed NMR', *Phys. Rev.*, 1986, Vol. **33**, P32.

11 Goldman M., Shen L., 'Spin-spin Relaxation in LaF_2', *Phys. Rev.*, 1966, Vol. **144**, P321.

12 Helfand E., 'Block Copolymers, Polymer-Polymer Interfaces, and the Theory of Inhomogeneous Polymers', *Acc. Chem. Res.*, 1975, Vol. 8, P295.

13 Bates F. S., Fredrickson G. H., 'Block Copolymer Thermodynamics: Theory and Experiment', *Annu. Rev. Phys. Chem.*, 1990, Vol. **414**, P525.

14 Denault J., Morese-Seguela B., Seguela R., Prud'homme J., 'Motional Perturbation at the Microphase Boundary in Thermoplastic Elastomers', *Macromolecules*, 1990, Vol. **23**, P4658.

15 Helfand E., 'Diffusion in Strongly Segregated Block Copolymers', *Macromolecules*, 1992, Vol. **25**, P492.

16 Hashimoto T., Fujimura M., Kawai H., 'Domain-Boundary Structure of Styrene-Isoprene Block Copolymer Films Cast From Solutions. 5 Molecular-Weight Dependence of Spherical Microdomains', *Macromolecules*, 1980, Vol. **13**, P1660.

17 Hashimoto T., Shibayama M., Kawai H., 'Domain-Boundary Structure of Styrene-Isoprene Block Copolymer Films Cast From Solution. 4 Molecular-Weight Dependence of Lamellar Microdomains', *Macromolecules*, 1980, Vol. **13**, P1237.

18 Hasegawa H., Tanaka H., Yamasaki K., Hashimoto T., 'Bicontinuous Microdomain Morphology of Block Copolymers. 1. Tetrapod-Network Structure of Polystyrene-Polyisoprene Diblock Polymers', *Macromolecules*, 1987, Vol. **20**, P1651.

19 Thomas E. L., Alward D. B., Kinning D. J. Martin D. C., Ordered Bicontinuous Double-Diamond Structure of Star Block Copolymers: A New Equilibrium Microdomain Morphology', *Macromolecules*, 1986, Vol. **19**, P2197.

20 Helfand E. Wasserman Z. R., 'Microdomain Structure and The Interface in Block Copolymers' In 'Developments in Block Copolymers - 1', Ed. Goodman I., Pub. New York: Applied Science, 1984.

21 Thomas E. L., Lescanec R. L., 'Phase Morphology in Block Copolymer Systems', Prepaper - *Phil. Trans. R. Soc. Lond. A* (1994)

22 Hajduk D. A., Harper P. E., Gruner S. M., Honeker C. C., Kim G., Thomas E. L., Fetters L. J., 'The Gyroid: A New Equilibrium Morphology in Weakly Segregated Diblock Copolymers', Prepaper (1994).

23 Anderson D. M., Davis H. T., Nitsch J. C. C., Scriven L. E., 'Periodic Surfaces of Prescribed Mean Curvature', *Ad. Chem. Phys.*, 1990, Vol. **37**, P337.

24 Thomas E. L., Alward D. B., Kinning D. J., Martin D. C., Handlin D. L., Fetters L. J., *Macromolecules*, 1986, Vol. **19**, P2197.

25 Thomas E. L., Anderson D. M., Henkee C. S., Hoffman D., *Nature*, 1988, Vol. **334**, P598.

26 Disko M. M., Liang K. S., Behal S. K., Roe R. J., Jeon K. J., *Macromolecules*, 1993, Vol. **26**, P2983.

27 Lescanec R. L., Muthukumar M., *Macromolecules*, 1993, Vol. **26**, P3908.

2.1 Block Copolymers

2.1.1 General Discussion

The advent of living polymerisation[1] allowed the proliferation of many specialised polymer systems to become synthetically available - including block copolymers. Living polymerisation prevents termination of the propagating polymer chain - this means the exclusion of all transfer agents that can cause termination, i.e. water (especially adventitious) and other nucleophiles. The result of living polymerisation, especially anionic polymerisation, is that the polymer produced has a monodisperse narrow molecular weight distribution, since the rate of initiation is much greater than the rate of propagation during the polymerisation. This is a vital characteristic because the result of phase separation would be well-defined domains of 'pure' polymer components. This is a necessary requirement since the modelling procedures of phase separation rely on a narrow interphasic region between the two components.

There are other factors that play a role in the resultant polymer structural characteristics.[2-4] In the system studied in this work, the solvent has to be able to solubilize both the styrene and butadiene monomers and also to disperse the terminating material - methanol. The initiator (sec-butyllithium) and solvent (benzene) also determine which type of addition occurs with the butadiene monomer. Poly-1,4-butadiene is the polymer of interest but transfer of a proton during the living stage of polymerisation can result in a 1,2 adduct - a methylene backbone with a vinyl pendant group. This by-product can adversely affect microdomain formation and the packing of the poly-1,4-butadiene chains. This is why sec-butyllithium was the preferred initiator since it had been found to be selective towards production of the 1,4 polybutadiene product.

The synthetic route used relied on styrene polymerising completely in a short period of time (2 hours) whilst butadiene was allowed to polymerise for a much longer

period (24 hours). This was necessary to prevent formation of random or alternating copolymer sequences. The overall synthesis route is given in Fig. 2.1 and a description of the practical details is given in the next section.

2.1.2 Synthesis of Styrene/Diene Copolymers

The synthesis procedure required high vacuum apparatus with a sequence of PTFE valves and bulbs to allow reactions and vacuum transfers to occur. The particular apparatus used is shown in Fig. 2.2:

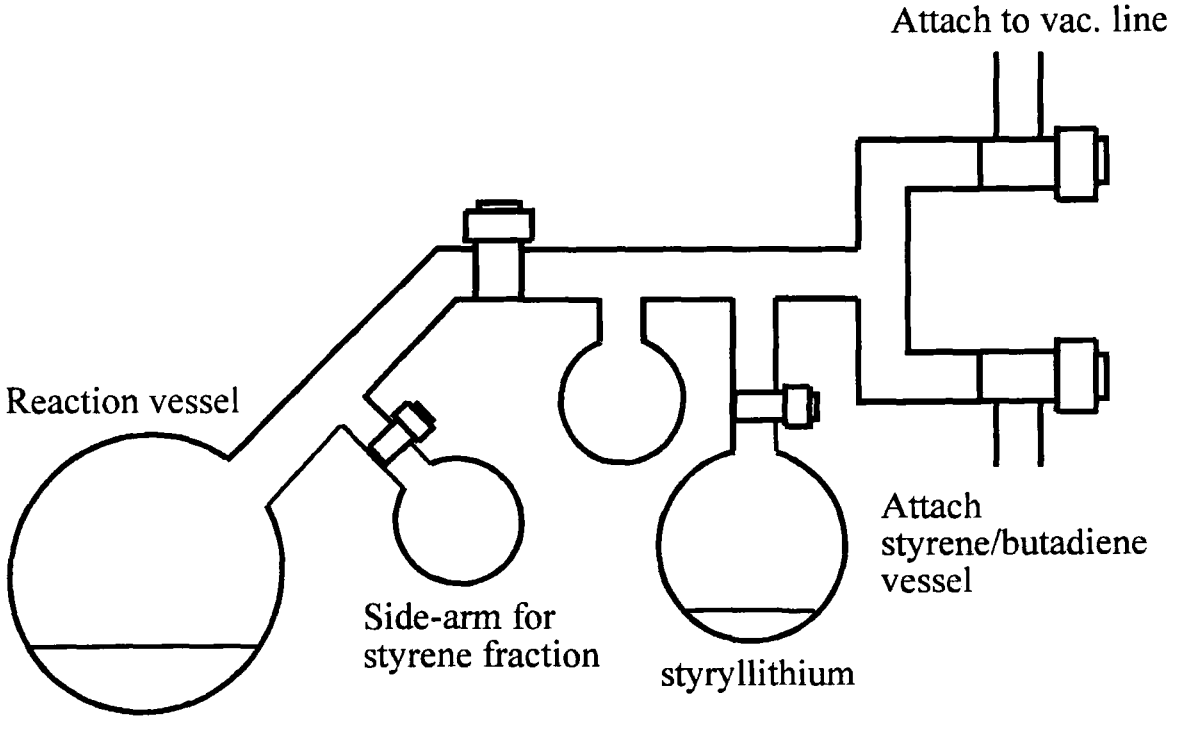

Fig. 2.2 Polymerisation Apparatus.

This system was first washed out using toluene, methanol and finally acetone, and then roughly evacuated using a water pump. This was then placed on a vacuum line and pumped down to below $5x10^{-6}$ atm (to remove any excess water and adventitious

INITIATION

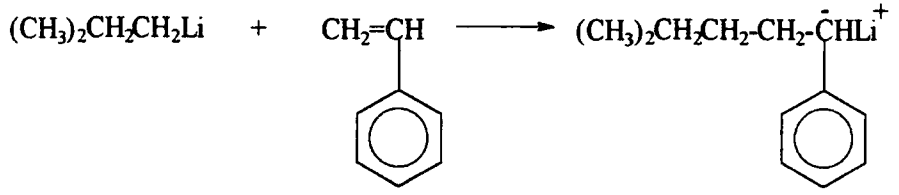

PROPOGATION

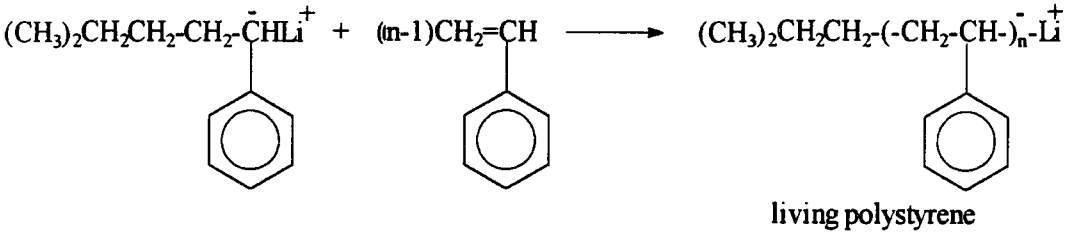

CROSS INITIATION

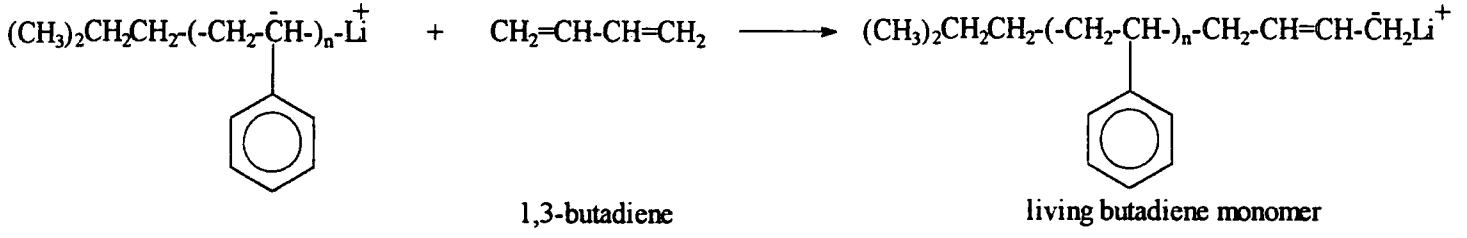

CROSS PROPOGATION

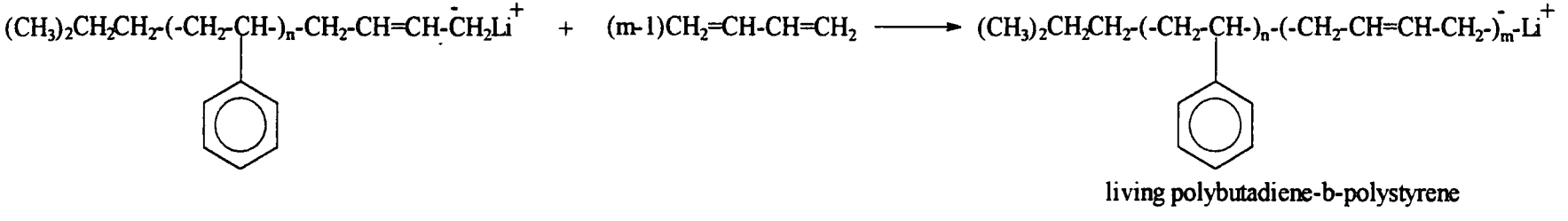

Fig. 2.1 Synthetic Route Used To Produce Diblock Polystyrene-b-butadiene Copolymers.

water). The system was then rinsed using the bulb containing living styryllithium. Benzene from the styryllithium bulb was carefully distilled into the reaction vessel and subsequently used to dissolve any living styryllithium and returned back to the bulb containing the styryllithium, in order to remove the styryllithium and any polymerised styrene present within the apparatus. This step of rinsing with the benzene solvent throughout the flask was repeated until there was no yellow coloration present within the apparatus. This was to try and produce a totally dry reaction environment.

Next, approximately 100 ml of benzene was distilled into the reaction flask. The benzene had been previously washed with sulphuric acid to remove sulphur impurities, (i.e. thiophene). The acidic benzene was washed with a distilled water and sodium bicarbonate mixture, azeotropically distilled using a Dean and Stark and then finally left to dry over $CaCl_2$. After some weeks the solution was filtered and placed on the vacuum line and supported over CaH_2 for one week before use.

The styrene monomer was transferred by distillation into a separate flask and the amount collected was noted. The styrene had previously been washed with conc. HCl (aq) neutralised by NaOH, filtered and dried over CaH_2 for one week.

The styrene fraction was then distilled over into the benzene-containing reaction flask and allowed to thaw to room temperature. A calculated amount of sec-butyllithium was added by syringe, via a side arm covered with a rubber septum, to initiate the styrene polymerisation to obtain a predetermined degree of polymerisation. The initiator was allowed to react for at least two hours (a yellow coloration was observed showing the initiator was still living and had not been terminated by moisture residues). Butadiene was then distilled, after this time, into a graduated flask immersed in a solid carbon dioxide/acetone mixture (-70°C) and subsequently allowed to thaw to 0°C (within an ice-water bath). This was done for safety reasons - at room temperature butadiene exerts a pressure of ~10 atm compared to ~2 atm at 0°C. The butadiene monomer was then transferred by distillation under vacuum into the living styryllithium polymer mixture in the reaction vessel and allowed to polymerise overnight. The reason for the longer reaction time for the butadiene monomer was that butadiene has a more

unreactive living species and the increased viscosity of the reaction medium hinders the diffusion controlled initiation.

The final living block copolymer was terminated ('killed') using nitrogen-purged methanol and an aliquot of antioxidant was added - BHT (butyrated hydrogenated toluene) which also helped kill the lithium living species. Subsequently, the polymer was precipitated using ten times excess of methanol and filtered and placed in a vacuum oven for at least three days.

The final materials were analysed using GPC (gel permeation chromatography) - for determination of molecular weight distribution - TGA (thermogravimetric analysis - using a Perkin Elmer TGA7 instrument) - to determine the temperature of polymer degradation - and DSC (differential scanning calorimetry) - to calculate the glass transition temperature of the diblock copolymers. Proton solution-state integrals were used to determine the accurate composition of the respective copolymer blocks. The results are contained within the next section.

2.1.3 Physical Characteristics

The results obtained for all of the synthesized polymers are summarised within Table 2.1-

Title	Comp. % (PS:PB)	Yield %	M_W	M_n	M_w/M_n	T_g /°C	T_g /°C	T_{DECP}/°C
SB1	50:50	87	161700	120000	1.31	-86.4	102.7	390
SB2	19:81	15	79200	79000	1.15	-85.6	99.1	399
SB3	60:40	89	182000	140000	1.29	-89.7	100.6	379
SB4	40:60	84	193300	160000	1.15	-90.8	98	378
SB5	33:67	89	53000	49400	1.07	-88.5	54.85	375

Table 2.1 Summary of Polymer Physical Characteristics.

The percentage weight-based compositions correlate exactly to the required compositions, except sample SB2 which did not polymerise to the necessary degree that was needed (required 66%:34% of polystyrene:polybutadiene). The yields again reflect the good conversion for the anionic polymerisation and again sample SB2 shows an anomaly. This anomaly has been traced to the solvent containing a large quantity of impurities, i.e. water, resulting in the premature termination of polymer chains during the living styryllithium stage.

All the copolymer samples have two glass transition temperatures which correlate to two differing components present within the copolymers. The glass transition at ca. -90°C corresponds to the polybutadiene moiety, which is below its glass transition temperature at room temperature, so explaining the rubber-like behaviour. The glass transition temperature at ca. 100°C corresponds to the polystyrene component. Since the polystyrene moiety is below its glass transition temperature at

room temperature, then there are no localised segmental motions and hence it is rigid in nature. Steric hindrance of the aromatic rings within the styrene system results in only a small amount of crystallinity within the polystyrene component. The decomposition temperature (from TGA analysis) corresponds to a 98% reduction, in weight, upon heating. This decomposition results from scission and oxidation of the carbon backbone of the copolymer to give a combusted product. These data shows that none of the glass transition temperatures detected result from any thermal degradation.

The molecular weights (M_W) for all of the copolymers should have been near 100000, except SB5 which should have had a molecular weight of 27500. This is clearly not the case which is surprising since the amount of initiator added to the reacting system corresponds to the rate of polymerisation and hence to the degree of polymerisation. The initiator was accurately titrated (with butanol and phenanthralene - to observe a green coloration corresponding to formation of lithium hydroxide) to check the number of moles added to the system so this should not have resulted in the exaggerated molecular weights obtained.

The calculations of the number average and weight average molecular weights are based on an intrinsic viscosity calculation involving the Mark-Houwink equation-

$$|\eta| = k.M^{\alpha} \qquad \text{Eqn. 2.1}$$

where $|\eta|$ is the intrinsic viscosity and M is the molecular weight. k and α are Mark-Houwink coefficients. From the reference: $k=1.119\times10^{-6}$ and $\alpha=0.725$.[5]

These constants are related to the elution volumes of the permeating gel (the spaces between pores and the accessible parts of the pores in the gel). Since most calibrants for GPC machines are polystyrene-based then errors start to occur when using other polymer systems. The main assumption used is that both polystyrene and polybutadiene have the same elution volumes for a particular molecular weight. However, a paper by Tung[5] recalculates the molecular weights of polystyrene- and polybutadiene-based copolymers and arrives at a correction factor of $M_{PS}/M_{PB}=1.7$.

Therefore, each of the molecular weights of polybutadiene, determined by GPC, needs to be corrected by a factor of 1/1.7 so that the overall molecular weights of the diblock copolymers become reduced - Table 2.2-

Sample	M_w	M_n
SB1	119000	94000
SB2	81000	69000
SB3	134000	107000
SB4	148000	129700
SB5	35400	32800

Table 2.2 Corrected Molecular Weights.

These corrected results show that the number and weight average molecular weights are closer to the required molecular weights of 100000. This further proves that there do seem to be heterocontact effects between unlike segments of block copolymers which is especially detectable in GPC data of styrene-butadiene copolymers. This conclusion was the major result from Tung's paper which does seem surprising in view of the inherent incompatibility of the polystyrene and polybutadiene chains.

The molecular weight distributions of the individual copolymers are larger than the optimum dispersions required. The polydispersity describes the ratio of the weight average molecular weight to the number average molecular weight. If this ratio is 1 then the polymer is described as monodisperse with a very narrow molecular weight distribution. If the ratio is above 1.5 then the polymer is too disperse for valid investigations. The values obtained from GPC were between 1.1-1.3 which describes a relatively narrow molecular distribution. However, each one of the GPC polymer distribution profiles had a low molecular weight shoulder of less than 10% of the main distribution intensity which resulted in an increase of the value of the polydispersity. Unfortunately, there seems to be no valid explanation for this low molecular weight

shoulder since during living anionic polymerisation conditions all the living chain ends are initiated and terminated at the same time which should result in a monodisperse distribution for the synthesized polymer.

2.1.4 Chemical Microstructure

The butadiene moiety, when polymerised has a complicated microstructure.[6-15] Butadiene can polymerise through a 1,4 and 1,2 addition route. The result of the 1,4 addition route is an adduct of either a cis or trans configuration (c and t respectively). The 1,2 addition route results in a pendant vinyl group (v). However, there are many possible combinations for all these three different conformations.

The possible structures found within the butadiene chains can be described in terms of triad and diad sequences. These are summarised by letters but examples of the structures are as follows in Fig. 2.3:

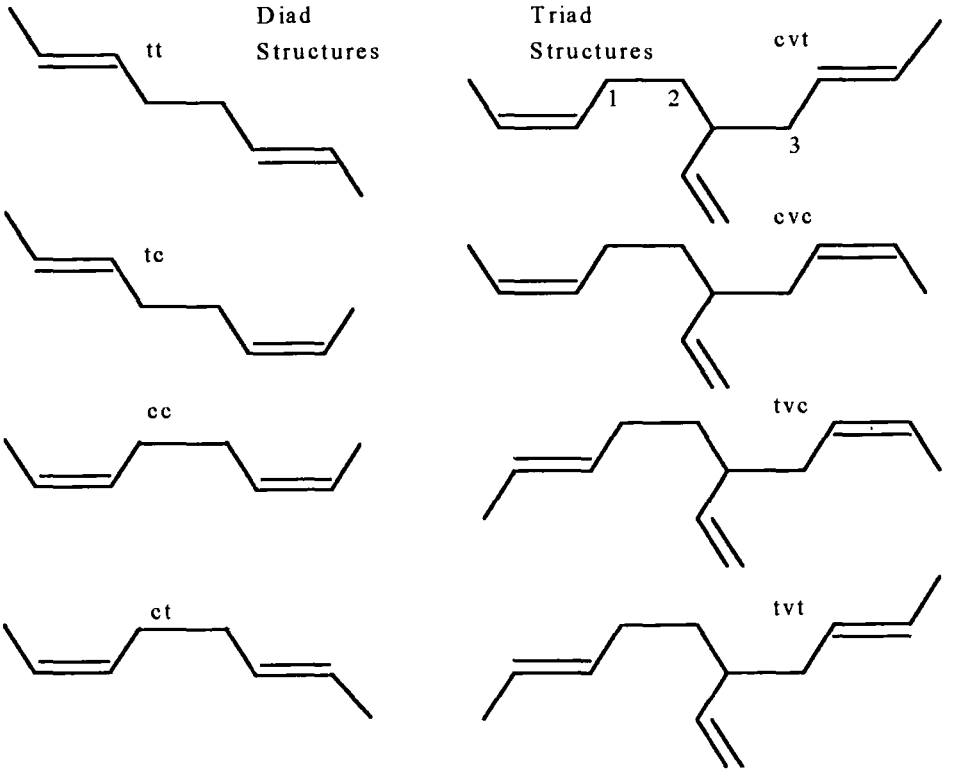

Fig. 2.3 Examples of Possible Diad and Triad Structures. Only triads involving a central v are shown.

For the methylene groups in t or c units, in the absence of 1,2 addition units, only diads need to be considered. Moreover, the **c**t and t**c** diads are equivalent as with **t**c and c**t**. Therefore only four methylene resonances of this type are expected, i.e. **c**c, **c**t, **t**c and **t**t, though Wang et al.[15] did not distinguish **c**c and **c**t yet found evidence for triad influence on trans signals.

The numbered methylene groups 1, 2 and 3 in the cvt structure show the three different resonances that can arise from the one triad.

cvt shows the methylene numbered 1

c**v**t shows the methylene numbered 2

cv**t** shows the methylene numbered 3

For methylene groups described by triads with a central vinyl group, there are four possible arrangements, i.e. **c**vc, **c**vt, **t**vc and **t**vt for type 1 and c**v**c. c**v**t, t**v**c and t**v**t for type 2; all of which give resolved signals according to Wang et al. However, these authors only distinguish three resonances for the cis and trans methylene groups which are adjacent to the methine part of the vinyl group, i.e. v**t** and v**c**, with two signals assigned to the former (presumed to be c**v**t and t**v**t).

The number of possible arrangements available to the saturated methine group in the 1,2 adduct are four. Both of the 1,4 arrangements on either side of the vinyl group affect the saturated methine resonance to give the four triads - t**v**t, t**v**c, c**v**t and c**v**c. The same four triads units influence the unsaturated methine and methylene 1,2 groups, but Wang et al. were not able to distinguish the t**v**c and c**v**t signals in either case, due to overlap of the resonances.

Determination of the possible arrangements for the t and c unsaturated methine groups is more complicated. In the absence of 1,2 units it has been recognised that resonances assigned to diads **c**t, **c**c, **t**t and **t**c can be clearly observed, the CH adjacent to the second unit being referred to in each case. However, more distant units do affect the chemical shifts. Thus, Wang et al observed fine structure in each of these

resonances, but merely commented that these "may some day be interpreted in terms of monomer triad sequences". For t and c units adjacent to v units, the numbering system used in the reference tries to describe bonding to the CH and CH_2 side of the vinyl group. If the conformer is on the CH_2 side of the vinyl group then the methine groups involved are numbered (1) and (2) and if on the CH side of the vinyl group then the methine groups are numbered (3) and (4). This can be seen clearly in fig. 2.4-

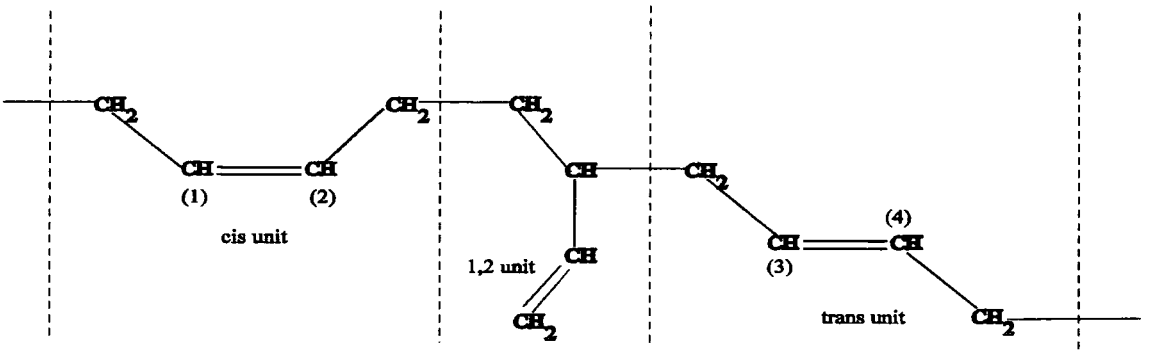

Fig. 2.4 Numbering System for Methine Resonances Adjacent to a Vinyl Group.

For the groups of type (3), Wang et al. saw separate resonances which they ascribed to v<u>c</u>t, v<u>c</u>c, v<u>t</u>t and v<u>t</u>c. However, for type (2) CH signals they only noted (without discussion) a single <u>t</u>v signal and no <u>c</u>v peak. This is surprising since by analogy one would expect separate resonances for t<u>c</u>v, c<u>c</u>v, t<u>t</u>v and c<u>t</u>v. Moreover, they report only diad influences on type (1) CH signals, i.e. they observe only <u>c</u>v and <u>t</u>v resonances, which is decidely odd, since the other neighbouring units should also have an influence, e.g. c<u>c</u>v and t<u>c</u>v should be distinguishable. Finally, they report a peak for the type (4) site v<u>t</u>, with no discussion of the influence of the other neighbouring unit and so suggestion for the chemical shift of the v<u>c</u> type (4) site.

These resultant different configurations have been assigned to the relevant microstructure peaks present in ^{13}C solution-state spectra and have been tabulated within the results described in the next section.

Polystyrene, when polymerised, is known to exist in many different tactic forms. Polystyrene diastereomers (adjacent methylene groups each having a pendant group - whilst ignoring the intervening methylene group with no pendant group) can exist in two conformations - racemic and meso forms. The meso form represents the diastereomer where the pendant group is on the same side of the polymer chain. However the racemic form represents the diastereomer with the pendant group alternating on either side of the polymer chain.[16-21]

The two conformations in diagrammatic form are shown in Fig. 2.5-

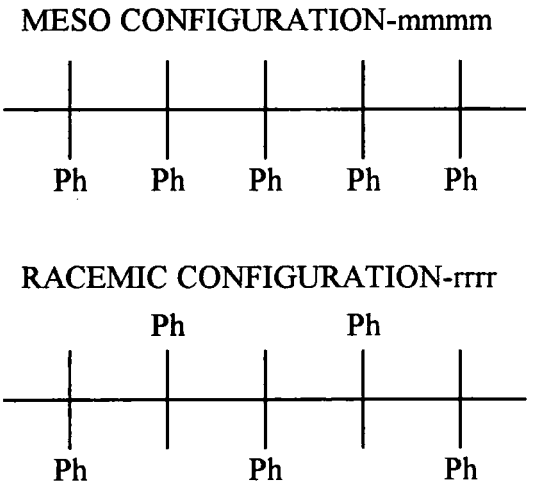

Fig. 2.5 Racemic and Meso Forms of Polystyrene. The intervening methylene carbons are not shown in the above diagrams.

The tacticity of the polymer chains (the longer scale arrangement of diastereomers along the chain) can be described in terms of the occurrence of meso and racemic relations. The syndiotactic form has all racemic diastereomers along the polymer chain and the isotactic form has all meso diastereomers along the polymer chain. The atactic form has an equal proportion of racemic and meso forms at random along the polymer chain.

2.2 Solution-state Investigations - ^{1}H and ^{13}C NMR

2.2.1 Experimental

The spectrometer used to obtain the solution-state results was a Varian VXR400 which observes proton nuclei at 399.964 MHz and carbon nuclei at 100.582 MHz. The spectrometer is set up such that the magnetisation is nutated not by 90° but by the Ernst angle, which is the optimum angle to observe a given carbon atom and 90° for direct proton detection. Due to the markedly different relaxation times for different protonated carbons the angle used is set to observe the best signal for slower relaxing nuclei because of the smaller tip angle while sacrificing only a small degree of signal from the faster relaxing, more proton-rich, species.

The samples prepared had to be a homogeneous mix of polymer and reference solvent. The reference materials used are tetramethylsilane which has a chemical shift of 0 ppm for proton detection and deuterated chloroform which has a chemical shift of 77 ppm for carbon detection. 100 mg of sample were dissolved in 0.7 ml of solvent but required, generally, 4 days to obtain complete solubilisation of the polymer. There seemed to be no viscosity broadening effects within the resultant spectra (broadening of all the resonant peaks), hence the greater concentration of sample in the some of the prepared solutions - SB3-SB5 (the standard dilution stated is 30 mg of sample in 0.7 ml of solvent).

The three copolymers that were the centre of the investigation were-

TK124 - diblock copolymer of 60%w/w polystyrene-b-40%w/w polyisoprene

SB1 - diblock copolymer of 50%w/w polystyrene-b-50%w/w polybutadiene

SB2 - diblock copolymer of 19%w/w polystyrene-b-81%w/w polybutadiene

SB3 - diblock copolymer of 60%w/w polystyrene-b-40%w/w polybutadiene

SB4 - diblock copolymer of 60%w/w polystyrene-b-40%w/w polybutadiene

SB5 - diblock copolymer of 37%w/w polystyrene-b-63%w/w polybutadiene

The reason that they were the focus of the investigations was that TK124 and SB4 are both directly comparable with only an extra methyl group in the isoprene moiety. The copolymer SB5 has the supposed Gyroid structure so may give interesting results due to its novel morphology.

2.2.2 Proton Solution-state Results[22-24]

Observed chemical shifts and their assignments for the butadiene-containing polymers are given in Table 2.3.

Peak (ppm)	Assignment
1.54	styrene methylene
~2	styrene methine proton
2.14	trans 1,4 polybutadiene methylene
2.2	cis 1,4 polybutadiene methylene
5.06	terminal olefin of 1,2 polybutadiene
5.07	terminal olefin of 1,2 polybutadiene
5.48	cis 2,4 polybutadiene vinyl proton
5.52	trans 1,4 polybutadiene vinyl proton
6.6-7.2	aromatic polystyrene meta protons
7.3	aromatic polystyrene ortho and para protons

Table 2.3 Chemical Shift Assignments for Proton Solution-State NMR of Block Copolymers of Polystyrene-b-polybutadiene - Samples SB1-5.

The polybutadiene linewidths are consistently narrower than the polystyrene linewidths. This is due to the greater rotational freedom available to the polybutadiene

chains which allows averaging of the lines unlike the more rigid polystyrene chains which undergo less segmental motion, and hence give broader resonances.

The isoprene-based copolymer contains most of the resonances present in the butadiene analogue. There are extra peaks at 1.587 ppm and at 8.023 ppm which represent methyl and carbonyl resonances. The broad background under the aliphatic region (1.5-4 ppm) represents oxidised material, in the presence of which is confirmed by the carbonyl peak at 8.023 ppm. The isoprene moiety is well known to be more easily oxidised than the butadiene case by free radical oxidation in air, since the free radical formed is a tertiary free radical, which is more stable compared to the secondary radical species formed with polybutadiene. This degree of oxidation is also not surprising because of the age of the TK124 polymer sample (over two years old).

Sample	Expected PS:PB Ratio	Actual PS:PB Ratio	1,4:1,2 Butadiene Ratio
SB1	60:40	55:45	87:13
SB2	66:34	93:7	85:15
SB3	40:60	39:61	94:6
SB4	60:40	59:41	91:9
SB5	37:63	36:63	92:8

Table 2.4 Ratios of Polystyrene to Polybutadiene and 1,4 to 1,2 Adduct Ratios.

The polystyrene:polybutadiene ratios (Table 2.4) were determined using integrals between the regions 6.2-7.2 ppm for polystyrene and 5.1-5.5 ppm for polybutadiene.[25] The 1,4:1,2 adduct polybutadiene ratios were determined from the integrals of the regions 5.5 ppm and 5.06 ppm for the 1,4 and 1,2 adducts, respectively. These four regions clearly contain only the relevant proton species for the ratios. The expected and observed ratios of polystyrene:polybutadiene show there is some degree of accuracy in the synthesis - except for SB2 which was contaminated from impure

benzene. The 1,4:1,2 adduct ratios show clearly that the by-product 1,2 adduct is generally less than 10%, by weight, of the whole polymer. This meets the requirement for only 1,4 addition products so correlating reasonably to the model systems used in microdomain thermodynamic simulations.

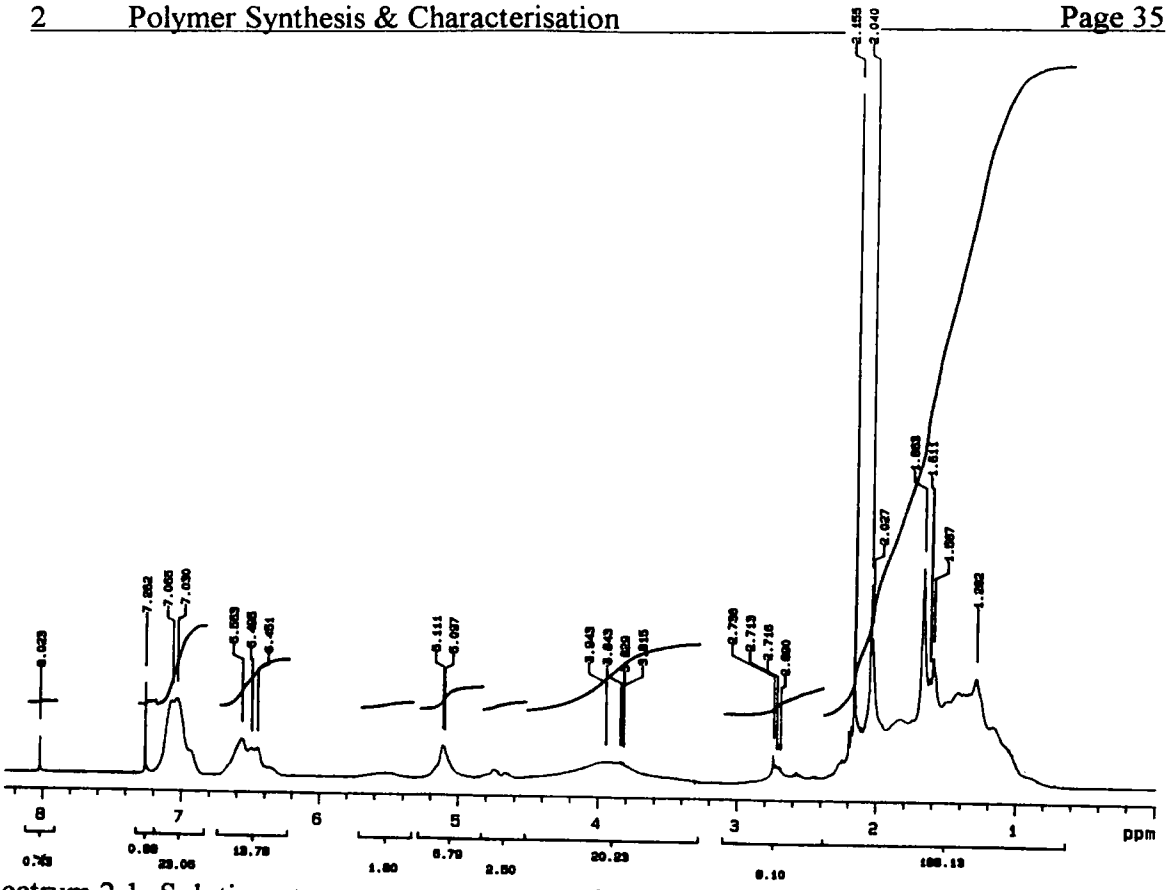

Spectrum 2.1 Solution-state proton spectrum of TK124 - 60% polystyrene-b-40% polyisoprene, referenced with $CDCl_3$

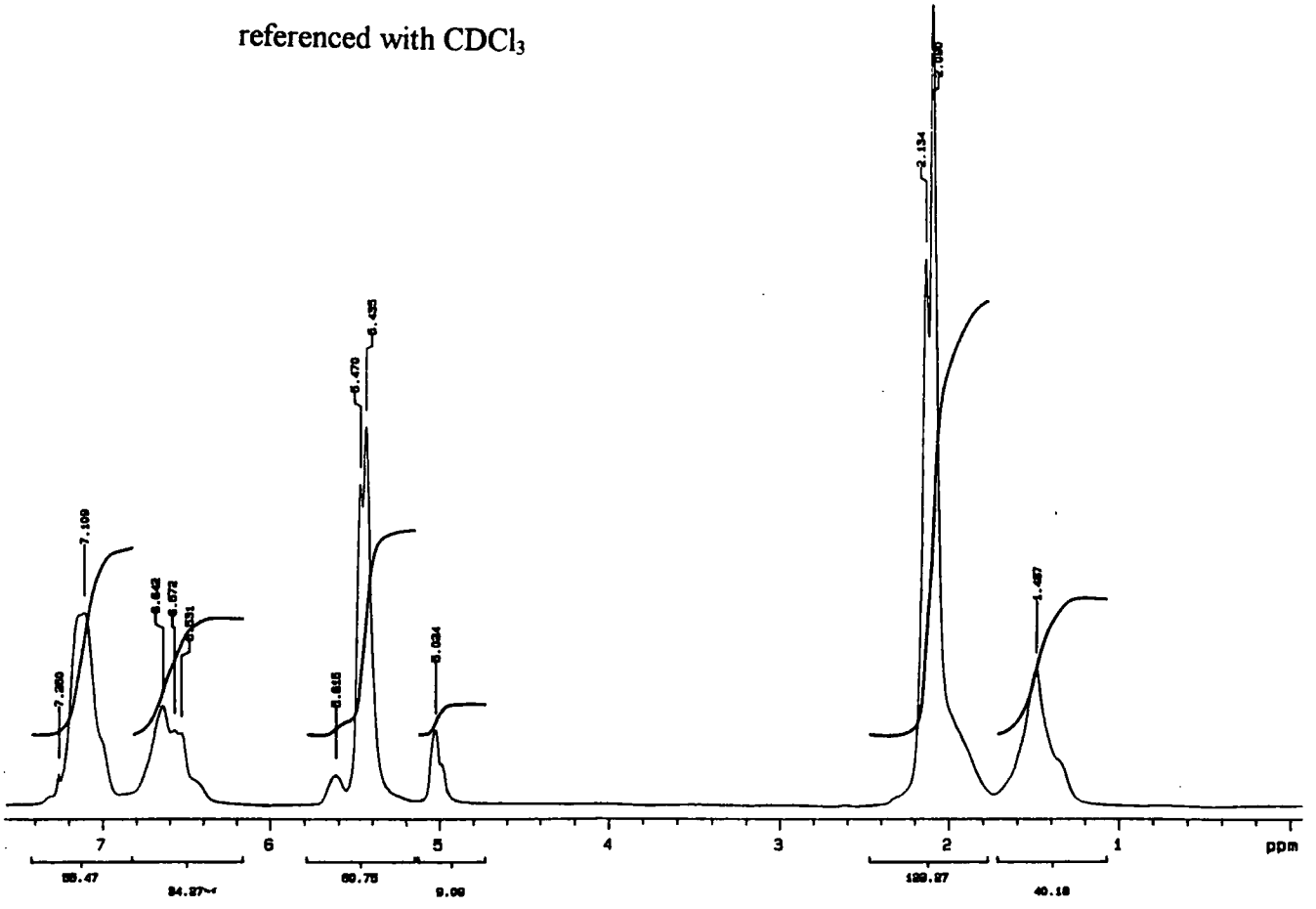

Spectrum 2.2 Solution-state proton spectrum of SB1 - 50% polystyrene-b-50% polybutadiene, referenced with $CDCl_3$

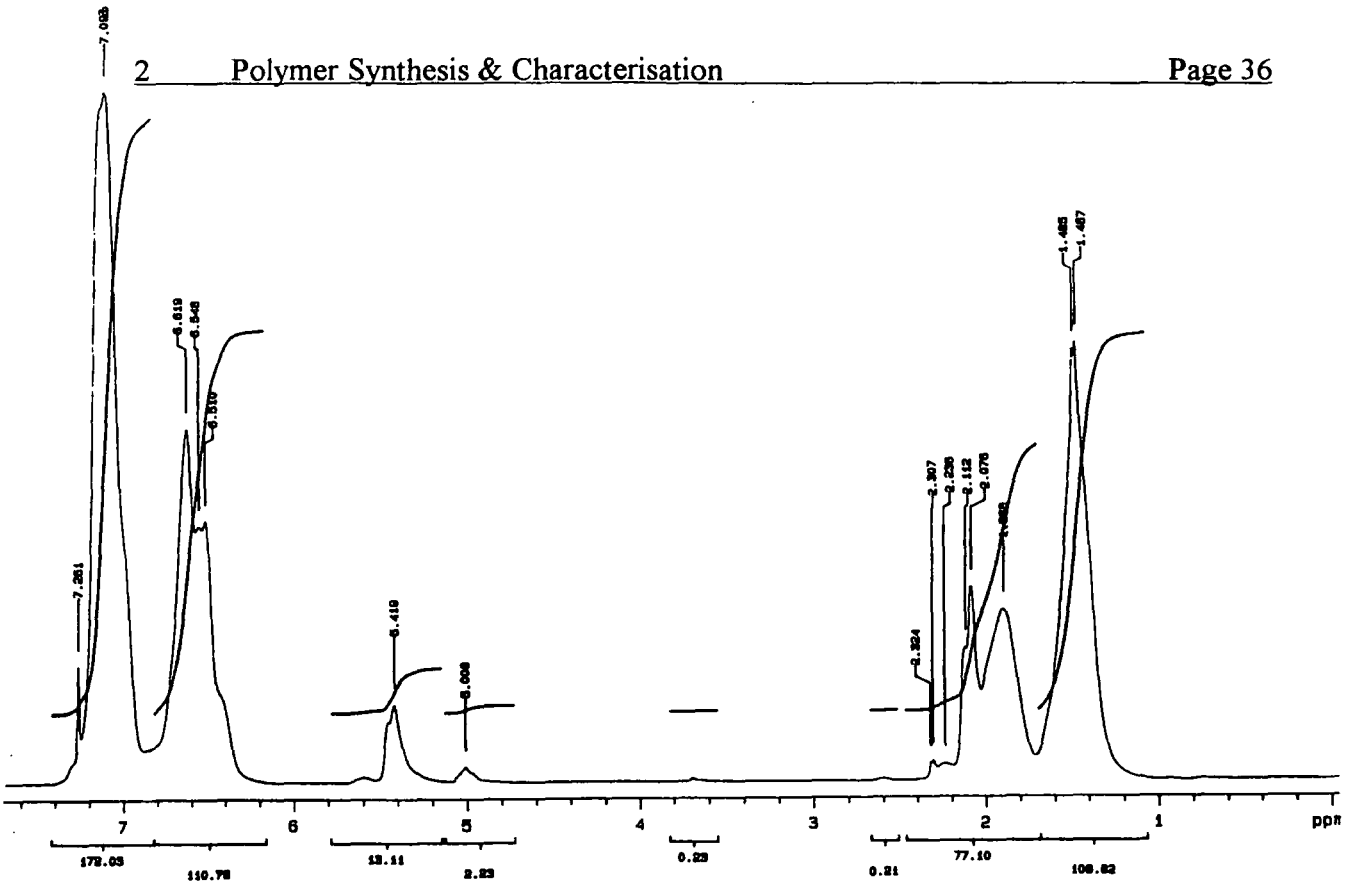

Spectrum 2.3 Solution-state proton spectrum of SB2 - 19% polystyrene-b-81% polybutadiene, referenced with $CDCl_3$

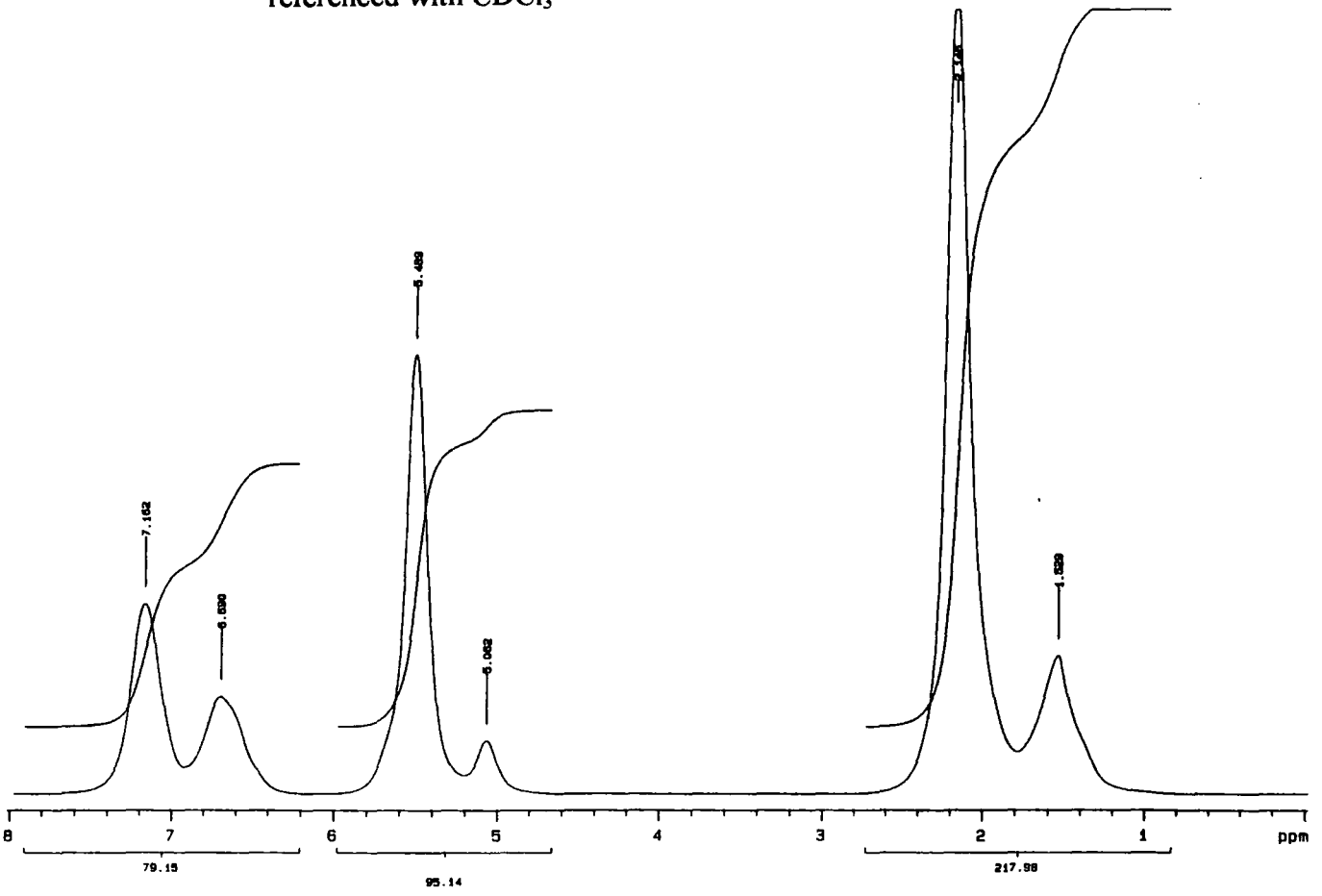

Spectrum 2.4 Solution-state proton spectrum of SB3 - 60% polystyrene-b-40% polybutadiene, referenced with $CDCl_3$

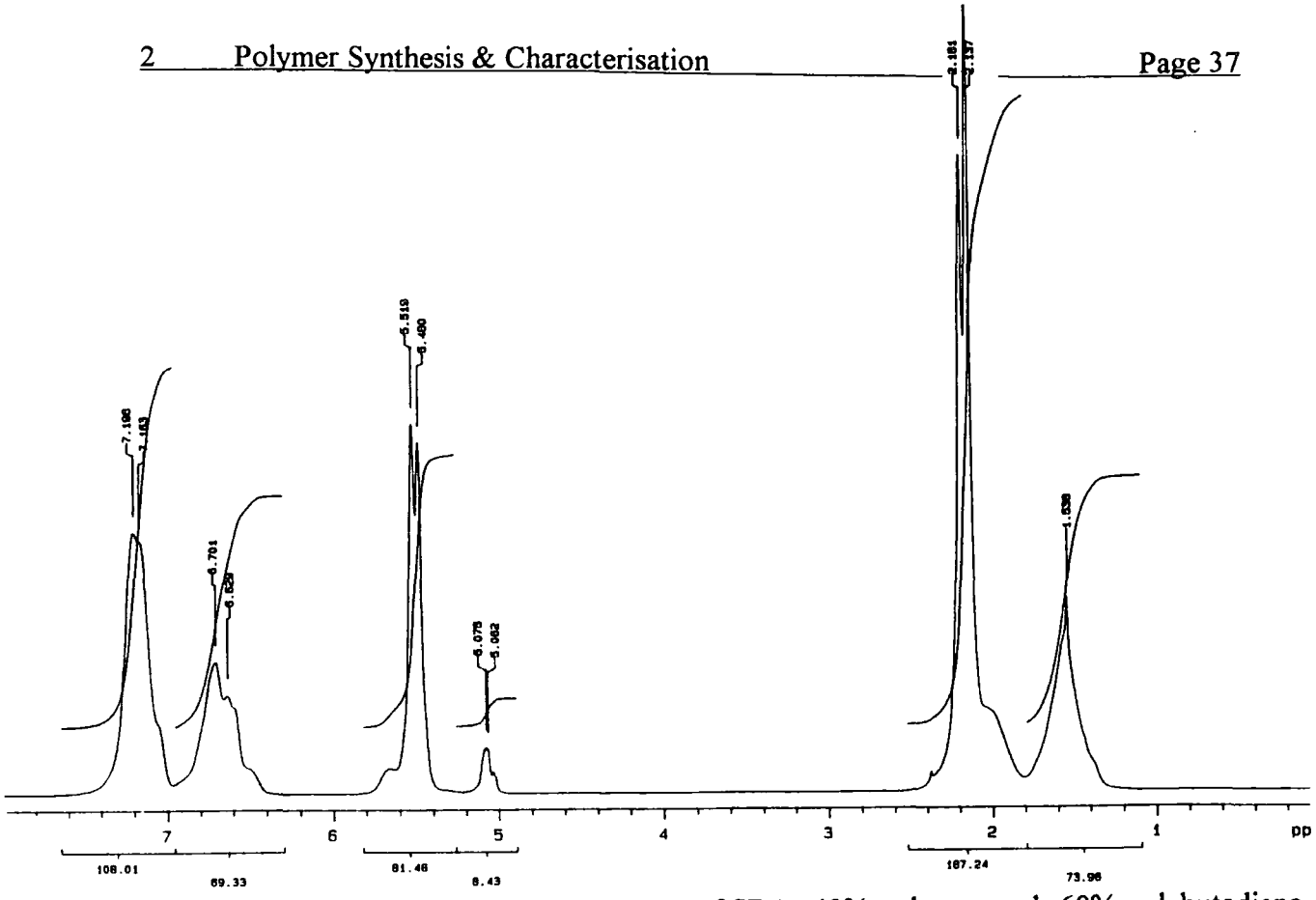

Spectrum 2.5 Solution-state proton spectrum of SB4 - 40% polystyrene-b-60% polybutadiene, referenced with $CDCl_3$

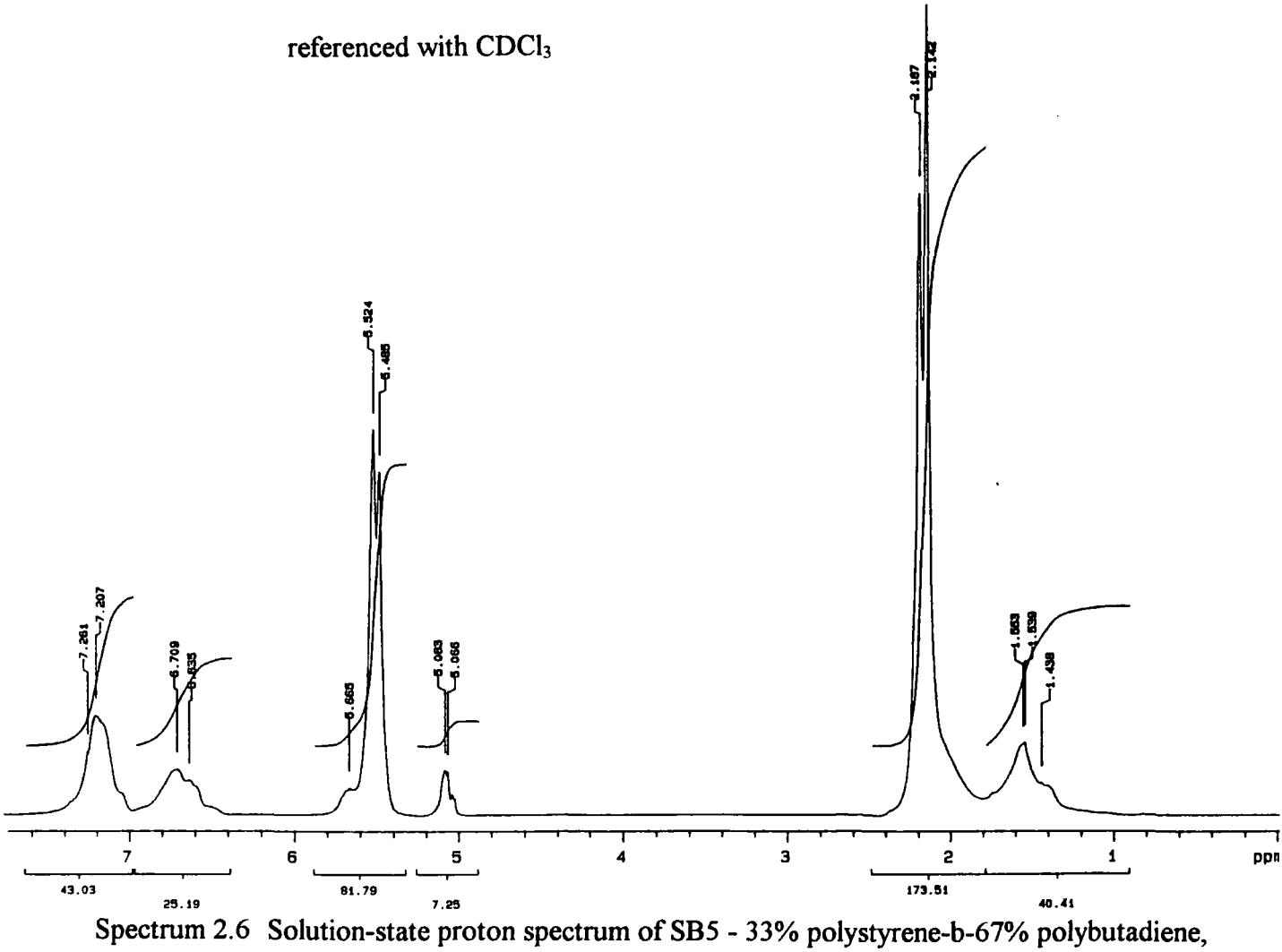

Spectrum 2.6 Solution-state proton spectrum of SB5 - 33% polystyrene-b-67% polybutadiene, referenced with $CDCl_3$

2.2.3 Carbon Solution-state Results[22]

Chemical Shift ppm	Assignment
24.8	cis CH_2 adjacent to a 1,2 adduct of butadiene, with cis/trans/vinyl splitting; split also into head and tail adducts
27.5	cis CH_2 next to a 1,4 adduct of butadiene
30.1	trans CH_2 next to a 1,2 adduct of butadiene, conformer split
32.7	trans CH_2 next to a trans and cis 1,4 adduct of butadiene
34	CH_2 of 1,2 adduct of butadiene next to a 1,4 adduct, conformer split
38.1	CH_2 of 1,2 adduct of butadiene next to a 1,4 adduct
40.3	CH of polystyrene
41-46	CH_2 of polystyrene in different conformational forms
43.6	CH_2 of polystyrene, CH of polybutadiene in a 1,2 adduct
114.2	terminal CH_2 of 1,2 adduct of butadiene
125.6	aromatic CH of polystyrene in the ortho position
127.3-128.3	aromatic CH of polystyrene in the meta and para positions
129.2-129.7	vinyl carbon in polybutadiene, cis set of peaks
129.8-131-7	trans configuration of vinyl carbon in polybutadiene
142.6	vinyl CH in the 1,2 adduct of polybutadiene
145.6	quaternary carbons in polystyrene, tactically split

Table 2.5 Results Of Polymer Solution-state Carbon Spectra For Samples TK124 and SB1-5.

All these assignments have been determined using SB4 as the common standard. This is because the aliphatic region of the polybutadiene moiety is closely similar to the corresponding region referred to in Chapter 4 of reference[24] - Bovey F. A., 'High Resolution NMR of Macromolecules' Pub. Academic Press 1972. However, this reference's description of the vinylic region of polybutadiene is markedly different to the results obtained for SB4. This might be due to the different type of polymerisation route

used in the synthesis, i.e. free-radical instead of the anionic polymerisation used for my polymer systems.

Referring to the two peaks occurring at 27.5 ppm and 32.7 ppm, one can see from the signal intensities that they are of equal intensity in the five butadiene-type copolymers with the exception of SB3, which has a trans:cis peak intensity ratio of approximately 6:5. The reason for this anomaly could be the Nuclear Overhauser Effect (through-space flip-flop-type interaction), but this would have also occurred for all the other solution-state spectra. The equal intensity of the trans and cis peaks means that the trans and cis forms at room temperature are produced with equal probability. Therefore, there is no particular thermodynamic advantage in having the trans or cis conformation, which is not surprising since the anionic intermediate formed during the polymerisation can be attacked from either 'side' to give equal forms of trans and cis conformers.

There is a marked difference in signal intensity with respect to the intensity of the reference material $CDCl_3$, which is due to different concentrations of polymer solution used in the analyses - SB1-2 used 30 mg in 0.7 ml of solvent and SB3-5 used 100 mg in 0.7 ml of solvent.

The differences between the spectra of SB1-5 (polystyrene-b-butadiene) and TK124 (polystyrene-b-isoprene) are that there are extra peaks for the latter due to the vinyl methyl group in the rubber part - namely peaks at 15.9 ppm (methyl - trans), 26.3 ppm and 39.9 ppm (methylene backbone carbons in the trans conformation), 23.3 ppm (methyl - cis) and 26.5 ppm and 32 ppm (methylene backbone carbons in the cis conformation). However, this region of the aliphatic region is more complicated than for the butadiene copolymer analogue because as well as 1,2 and 1,4 addition, 1,3 addition is also known to occur due to the migration of the methyl group whilst in the 'living' anionic stage.

The aromatic region is similar to the butadiene analogue but there are two peaks at 162.9 ppm and 174.4 ppm which correspond to carbonyl functionalised polymers in aldehyde and ketone (quaternary) carbon forms. This is directly due to the age of this

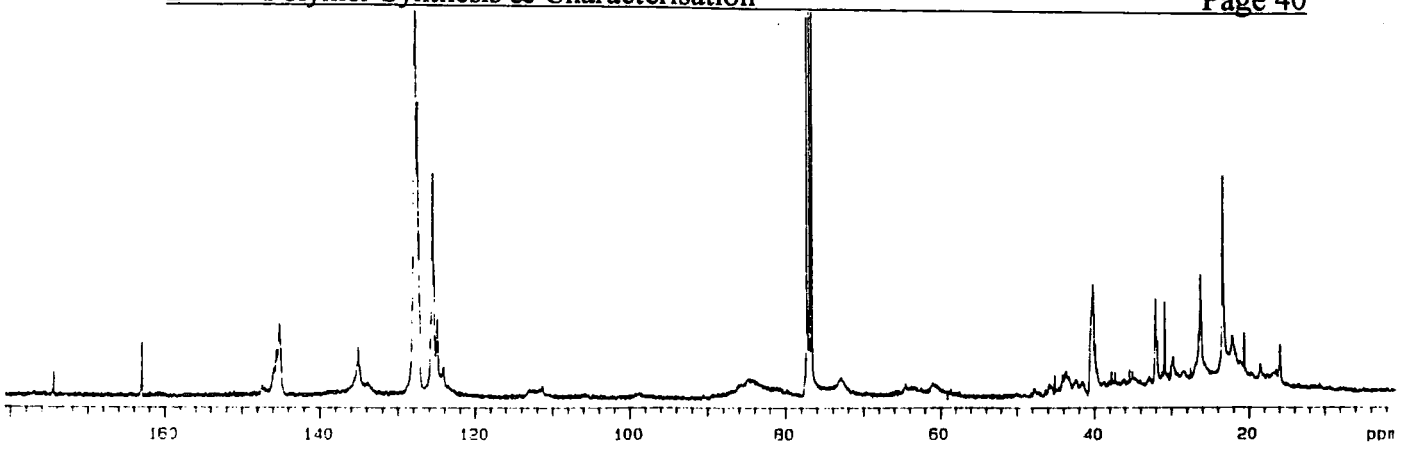

Spectrum 2.7 Solution-state carbon spectrum of TK124 - 60% polystyrene-b-40% polyisoprene, referenced with $CDCl_3$, dilution = 30 mg in 0.7 ml

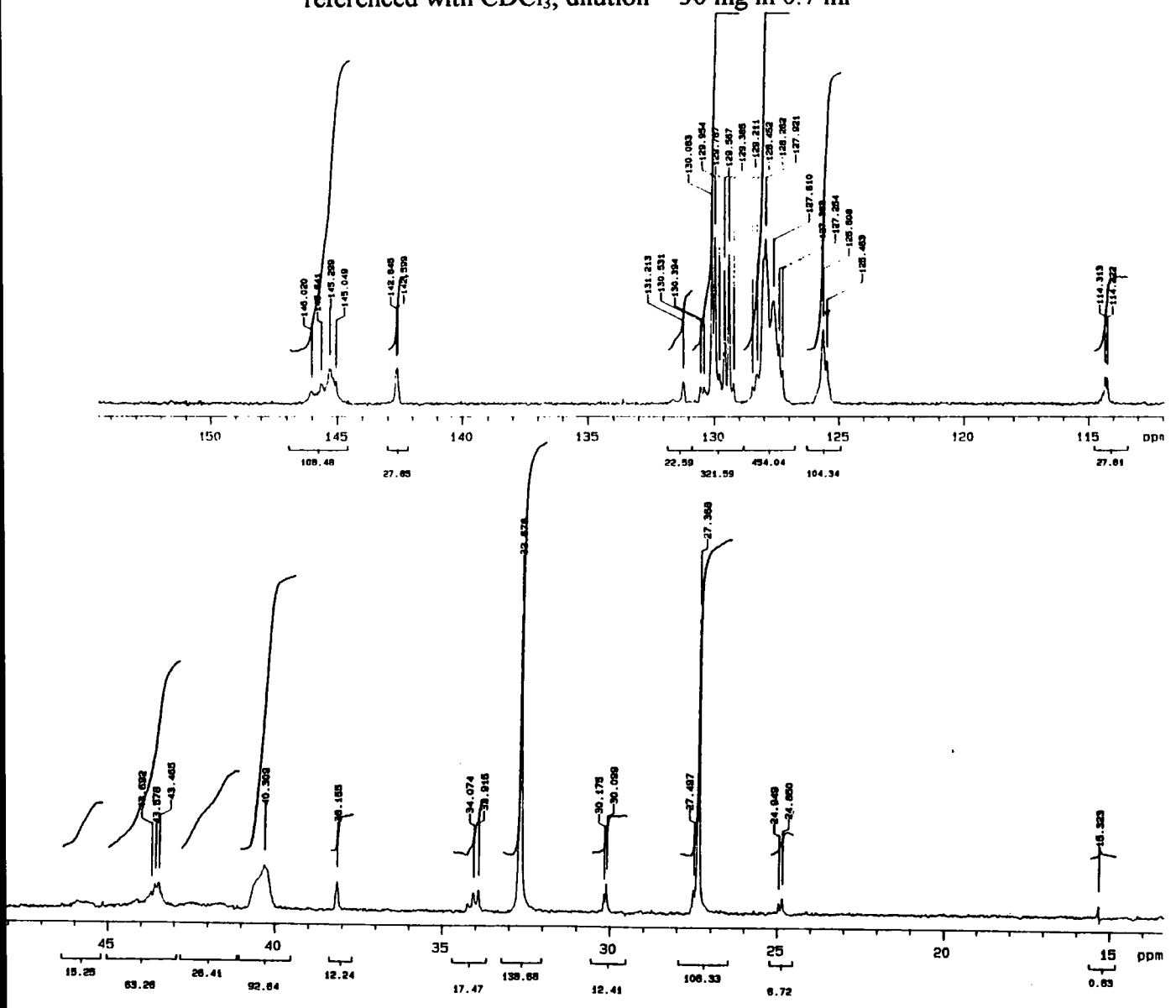

Spectrum 2.8 Solution-state carbon spectrum of SB1 - 50% polystyrene-b-50% polybutadiene, referenced with $CDCl_3$, dilution = 30 mg in 0.7 ml

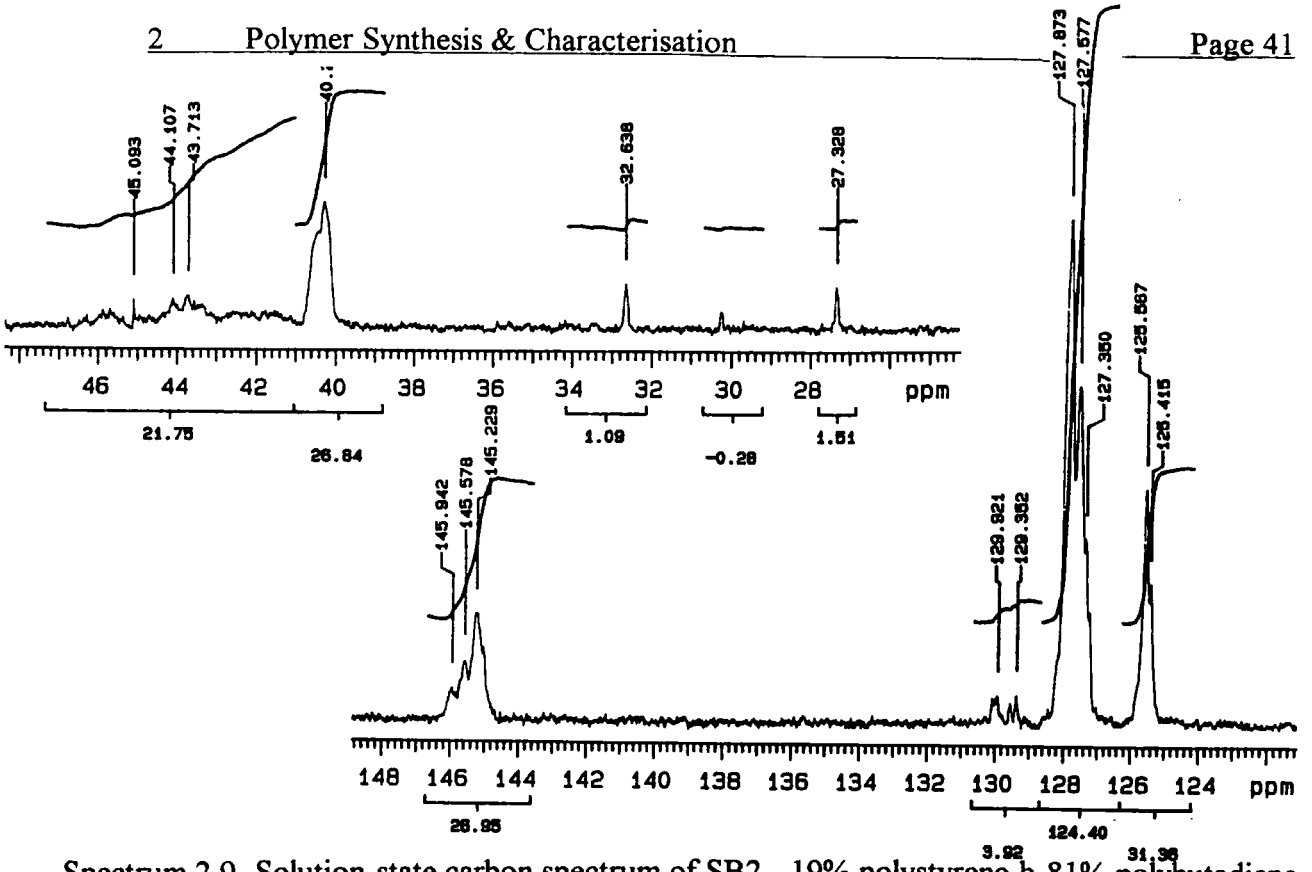

Spectrum 2.9 Solution-state carbon spectrum of SB2 - 19% polystyrene-b-81% polybutadiene, referenced with $CDCl_3$, dilution = 30 mg in 0.7 ml

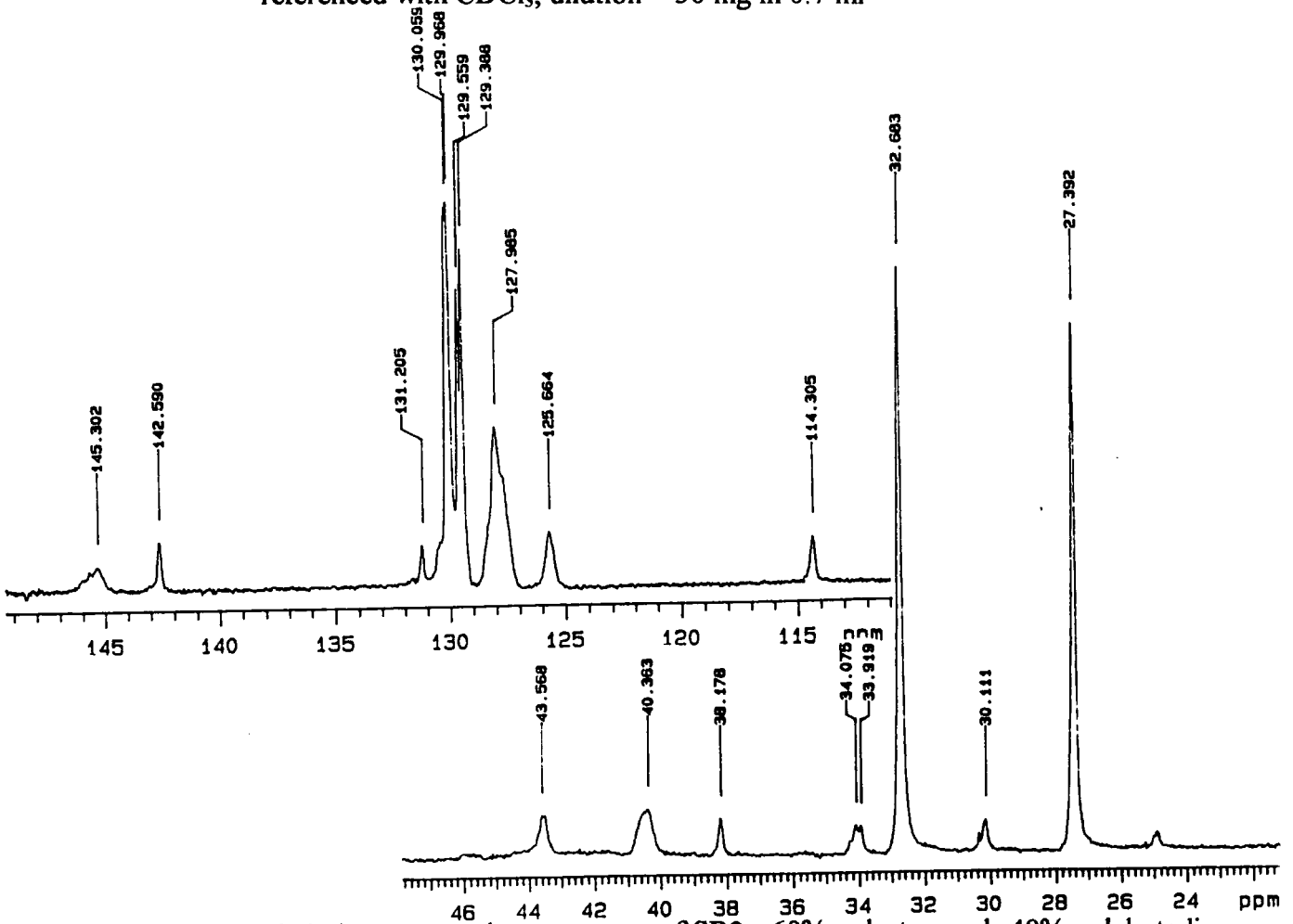

Spectrum 2.10 Solution-state carbon spectrum of SB3 - 60% polystyrene-b-40% polybutadiene, referenced with $CDCl_3$, dilution = 100 mg in 0.7 ml

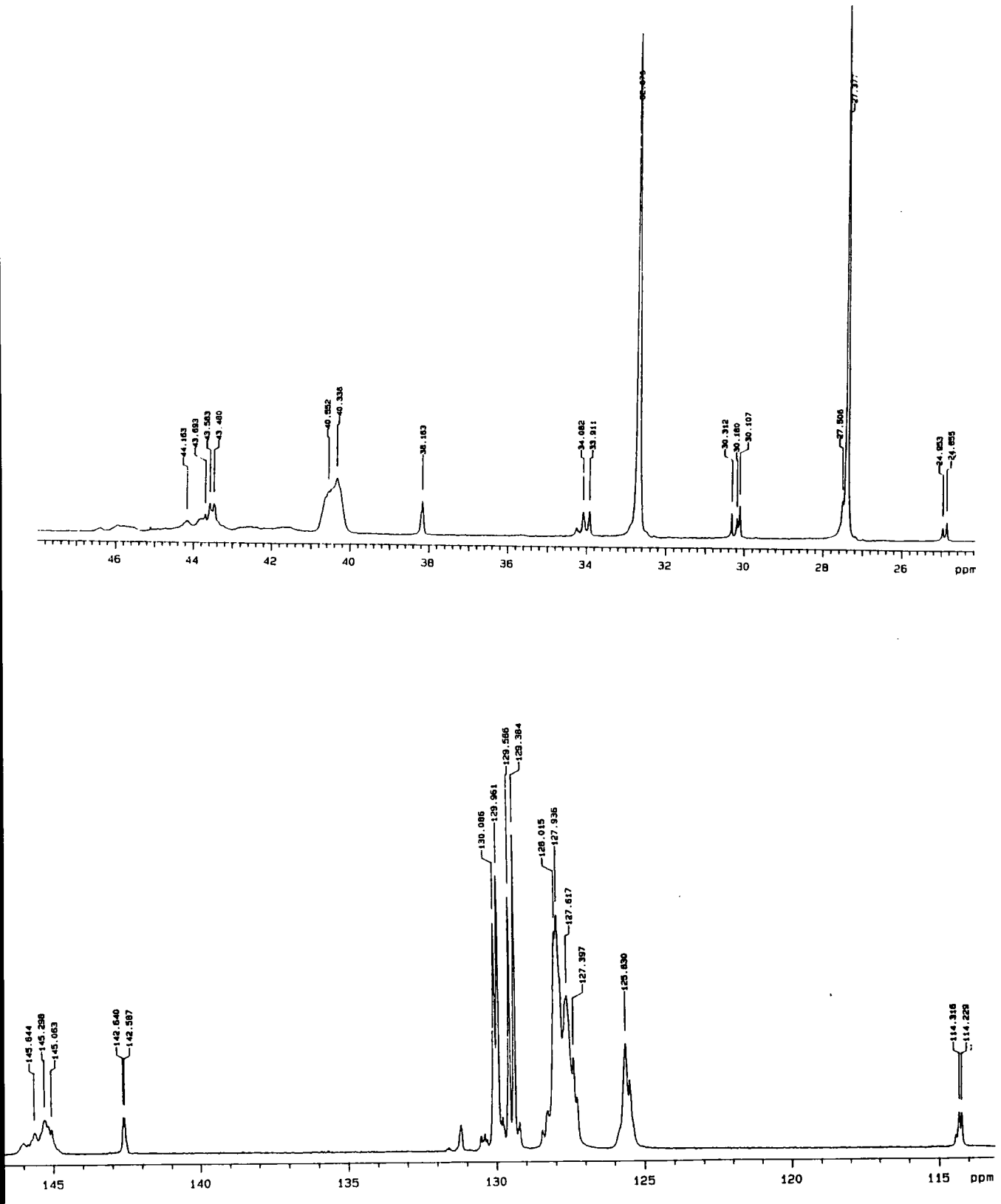

Spectrum 2.11 Solution-state carbon spectrum of SB4 - 40% polystyrene-b-60% polybutadiene, referenced with $CDCl_3$, dilution = 100 mg in 0.7 ml

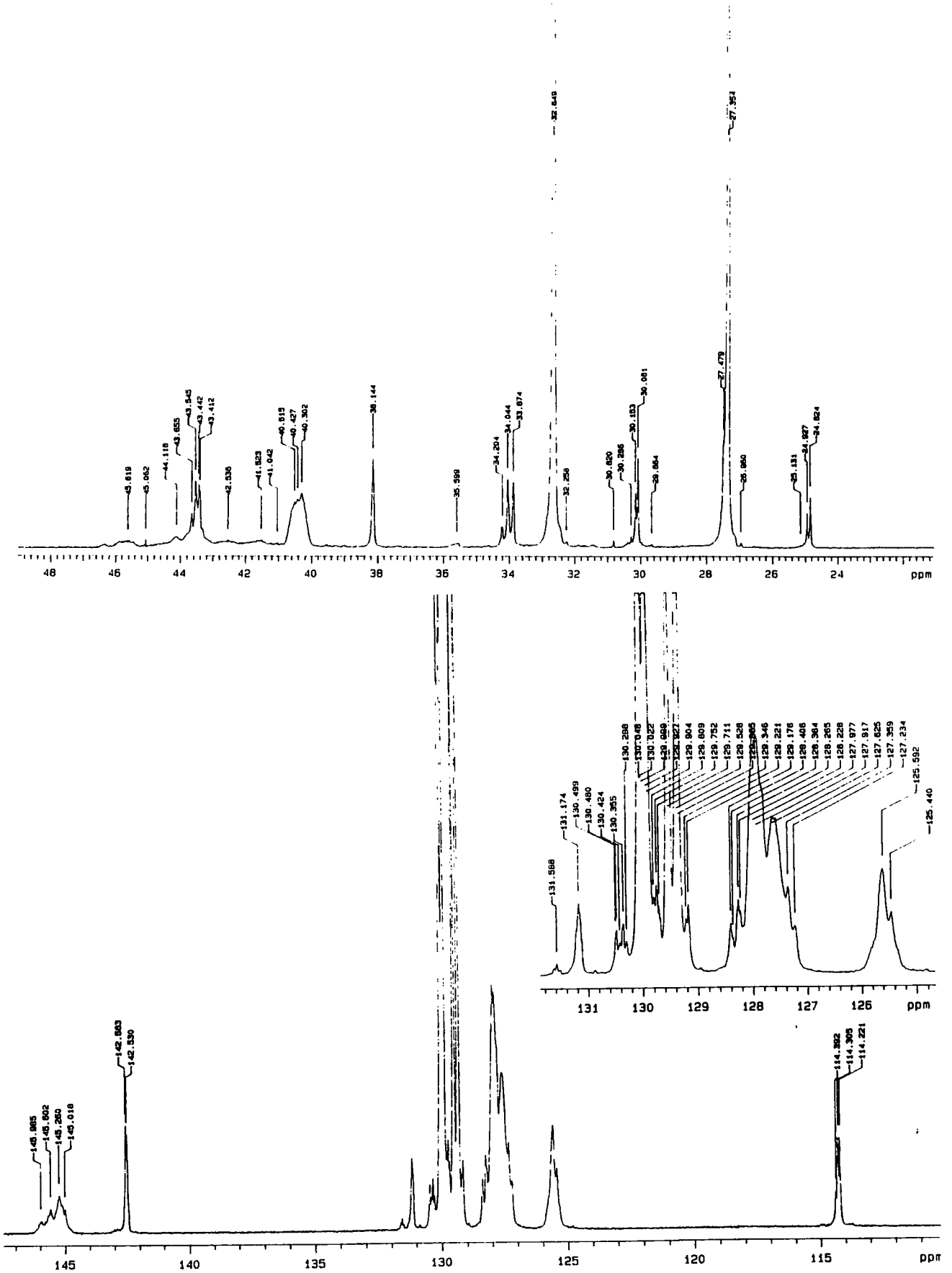

Spectrum 2.12 Solution-state carbon spectrum of SB5 - 33% polystyrene-b-67% polybutadiene, referenced with $CDCl_3$, dilution = 100 mg in 0.7 ml

polymer which over a period of time, being air-sensitive, has cross-linked. This also explains the broad background under each peak in the spectrum - corresponds to cross-linked material such as ether and ester cross-linkages.

Further investigations were made into the determination of the individual polymer's microstructures. The polybutadiene aliphatic region was thoroughly studied and the following assignments were made with reference to Patterson P. J. and Koenig J. L. (Peroxide Cross-linked Natural Rubber and cis-Polybutadiene)[11] and Wang H. T. et al., (^{13}C-NMR Spectra of Isomerized Polybutadienes).[15]

These results have been summarised in table 2.6 on the next page-

Table 2.6 ^{13}C Solution-state Results for Polybutadiene Microstructure.[15]

Peak (ppm)	δ_{REF}-δ_{SB4}	Assignment of butadiene environment[a]
24.839	+0.08	methylene in the triad cvt
~25.0	+0.02	methylene in the triad cvc
27.36	+0.01	methylene in the diad ct
27.49	-0.03	methylene in the diad cc
30.09	+0.01	methylene in the triad tvt
30.16	+0.01	methylene in the triad tvc
30.3	---	not in the reference (acetone impurity)
32.68	+/-0.02	methylene in the diads tt + tc + vc
33.9	+0.18	methylene of 1,2 adduct in triad tvt
34.07	+0.11/+0.16	methylene in triads tvc + cvt
~34.2	+0.17	methylene in the triad cvc
38.14	0,+0.03	methylene in the vt
43.44	+0.02	methine of the triad tvt
43.47	+0.07	methine in the triad tvc
43.56	+0.03	methine of the triad cvt
~43.7	-0.01	methine of triad cvc
114.22	-0.14	vinyl CH_2 in the triad tvt
114.30	-0.14	vinyl CH_2 in the triads tvc + cvt
114.39	-0.13	vinyl CH_2 in the triad cvc
127.92	-0.04	CH(3)= in the triad vct
128.00	+0.06	CH(3)= in the triad vcc
128.25	+0.13	CH(3)= in the triad vtt
128.43	+0.09	CH(3)= in the triad vtc
129.20	+0.08	CH(1)= in the diad cv
129.37	+0.07	* CH= in the diad ct
129.55	-0.07	* CH= in the diad ct
129.73	-0.10	* CH= in the diad cc
129.77	-0.12	* CH= in the diad cc
129.828/.927	0/-0.001	CH(1)= in the diad tv/CH(4)= in the diad vc
129.95	+0.06	* CH= in the diad tt
130.075/.317	-0.005/-0.139	* CH= in the diad tt + tc
130.38	-0.2	* CH= in the diad tc
130.45	+0.04	CH(4)= in the diad vt
130.507	-0.001	CH(2)= in the diad cv (ref. = vt)
131.19	+0.09	CH(2)= in the diad tv
142.57	+0.12	CH= in the triads cvc+cvt+tvc
142.63	+0.12	CH= in the triad tvt

[a] Olefinic carbons of 1,4 units adjacent to 1,2 units are identified by the numbering system:
-CH_2CH(**1**)=CH(**2**)CH_2--CH_2CH(CH=CH_2)--CH_2CH(**3**)=CH(**4**)CH_2-

* more than one resonance quoted at this chemical shift

Bold, underlined letters represent the designated conformer for the appropriate chemical shift. As an example the peak assigned to 24.839 ppm is attributed to the following triad **c**vt

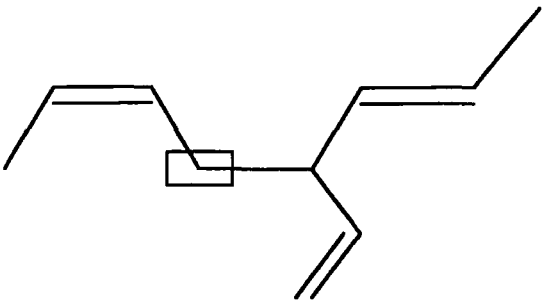

Fig. 2.6 Nomenclature for Designating a Particular Carbon in a Butadiene Triad.

The boxed methylene unit is the carbon responsible for the observed chemical shift at 24.839 ppm.

Relative intensities of the peaks at 24.84 ppm and ~25 ppm show that there are slightly more methylenes in the triad **c**vt compared to the triad **c**vc. Continuing along this line, the intensity of the **c**t resonance is greater than that for the c**c** resonance. This shows that the occurrence of the cis and trans groups along the butadiene chains is of an oscillatory nature instead of a block-type nature. However, the peak for **t**vt is of a much greater intensity compared to **t**vc. The peaks at 30.3 ppm is only seen in the spectrum for SB4. This peak is very narrow compared to the butadiene resonances and is due to the methyl group in acetone which is an impurity that has arisen whilst cleaning the NMR tube.

The diads **t**t, **t**c and v**c** cannot be individually assigned since they are swamped by the **t**t resonance. The vinyl methylene triads are in a ratio of 5:5:1 for t**v**t:t**v**c+c**v**t:c**v**c respectively which shows the unfavourability of the vinyl group surrounded by cis conformers. There is a shoulder for the peak at 34.07 ppm which could be the t**v**c

component but it is not of an equal intensity to the cvt component. At 38.14 ppm there are two overlapping peaks corresponding to cvt and tvt.

Unlike the reference of Wang et al. the triad sequences for the vinyl methine groups are resolved but the intensity for the cvc triad is smaller than the rest which correlates with the reference intensities. This suggests that it is unfavourable for the polymer chain to have two cis groups sandwiching the vinyl group whilst the trans and cis or trans and trans triads are more favourable. The vinyl methylene groups again show the same four triad sequences with the cvt and tvc resonances overlapping and showing the same small intensity of the cvc peak.

Due to the overlap of the polystyrene CH resonance, the methine resonances for trans and cis conformers have been only tentatively assigned. The first four peaks are the methine groups of the trans and cis conformers adjacent to the methine side of the vinyl group. None of the conformations could be identified with triad resonances so only diadic forms were used for assignment. Also, the resonances for vc could not be assigned.

The vinyl methylene resonances in vinyl triads could be assigned but there is again an overlap of the resonances for cvt and tvc. Strangely, all these resonances are shifted by 0.14 ppm compared to the reference of Wang et al.

The unsaturated methine resonances in the 1,4 adducts of polybutadiene overlap with the ortho and meta carbons of the polystyrene ring resonances. However, the peaks of the polybutadiene unsaturated methine resonances are superimposed on the broad styrene resonances. The assignments are the same as the Wang et al. reference except that the diad sequence cv has had all four of its possible resonances assigned. This was achieved by comparing the difference in the resonances of the four trans equivalents and assigning them to surplus peaks found in the spectrum. The agreement with the surplus peaks is surprisingly good. Still more surprising is the triad splitting for the CH(3)= in vct and vcc but none for CH(2)= in the diad cv.

Analysis of the polystyrene's conformation was less straightforward than the polybutadiene analysis. The methylene region of styrene has a relatively wide spectral

distribution and low signal intensity between 38-48 ppm - so could not be readily assigned. However, the quaternary region for styrene was assigned using Tonelli's paper entitled - "Stereosequence-Dependent ^{13}C NMR Chemical Shifts in Polystyrene."[18] The following results were obtained - Table 2.7:

PEAK (ppm)	ASSIGNMENT
146.00	mmmm, mmmr
145.84	rmmr
145.63	mmrm, mmrr
145.28	mrmr, rrmr
145.05	rrrr, rrrm, mrrm

Table 2.7 Polystyrene Tacticity Assignment.

The symbols m and r represent meso and racemic sequences in the polystyrene polymer backbone.

This reported sequence of five different sets of racemic forms for the quaternary carbon in polystyrene, according to Tonelli, represents an atactic conformation for the polystyrene chains within the copolymer. They have an intensity distribution which is Gaussian in nature, i.e. the mmmm and rrrr sequences have the smallest intensity within the distribution whilst the mixtures of diastereomers have a greater probability of occurring and so giving rise to a greater peak intensity.

This suggested set of conformations for polystyrene is also found in a paper by Sato H. et al.[17], which uses a simulation based on Bernoullian statistics with a probability of the meso form being produced during polymerisation of P_m=0.54. This probability corresponds to an atactic chain conformation with a ratio of mm:mr:rr of 1:2:1 (hence the use of Bernoullian statistics, with a value of P_m corresponding to an almost equal probability of meso or racemic forms occurring).

2.2.4 Conclusions

A number of deductions can be made as to the relative microstructure of the polybutadiene moiety within the polystyrene-b-polybutadiene copolymer in the solution-state-

1 There are no detectable signals corresponding to the methylene carbons of either polystyrene or polybutadiene being adjacent to the opposing polymer thus strongly suggesting a block copolymer and not a random or alternating copolymer.

2 There are no triad sequences existing as two adjacent 1,2 adducts suggesting that the 1,2-adduct is a minor component.

3 The existence of equal numbers of cis- and trans-containing triads suggests that there is no conformational advantage in having either the cis or trans configuration at room temperature. Previous work on anionic initiators, especially secBu^{t}Li, suggests that a ratio of cis:trans:1,2 configurations should be approximately 45:45:10 which is confirmed with the ^{13}C assignments (even with spectral peak intensities) whilst the proton spectra give percentage ratios of 38:39:23.

4 Analysis of the diad assignments shows that the ct diad predominates more within the butadiene sequence than the cc diad sequence. This suggests that the polymer consists of an alternation of cis and trans units within the polybutadiene chains and overall having an equal distribution along the chains.

5 The cvc arrangement is unfavourable compared to cvt/tvc and tvt triads. This could be due to conformational steric hinderance.

6 The polystyrene is atactic in nature confirming the bulky nature of the rings preventing the tactic coiling and packing of chains.

2.3 References

1 M. Morton and L. J. Fetters, 'Anionic Polymerization of Vinyl Monomers', *Rubber Chemistry and Technology*, 1974, Vol. **48**, P361-409.

2 R. P. Quirk and B. Lee, 'Experimental Criteria for Living Polymerizations', *Polymer International*, 1992, Vol. **27**, P359-367.

3 R. P. Quirk and J. Ma, 'Dilithium Initiator Based on 1,3-bis(1-Phenylethenyl)benzene. Tetrahydrofuran and Lithium sec-Butoxide Effects', 1991, *Polymer International*, Vol. **24**, P197-206.

4 M. Morton and L. J. Fetters, 'Homogeneous Anionic Polymerization of Unsaturated Monomers', 1971, *Macromolecular Research*, Vol. **2**, P71-108.

5 L. H. Tung, 'Block Copolymer Molecular Weight by GPC', *J. Appl. Polym. Sci.*, 1979, Vol. **24**, P953-963.

6 F. Conti, A L. Segre, D. Pini, L. Porri, '^{13}C N.M.R. Spectra of Polybutadienes:2', *Polymer*, 1974, Vol. **15**, P816-818.

7 G. van der Velden, C. Didden, T. Veermans and J. Beulen, 'New Method for the Microstructure Determination of Polybutadiene with Cis-1,4, Trans-1,4 and Vinyl-1,2 Units by ^{13}C NMR', *Macromolecules*, 1987, Vol. **20**, P1252-1256, No. 6.

8 J. Furukawa, E. Kobayashi, N. Katsuki and T. Kawagoe, '^{13}C-NMR Spectrum of Equibinary (cis-1,4-1,2) Polybutadiene', 1974, *Die. Makromol. Chemie.*, Vol. **175,** P237-245.

9 S. Bywater, 'Microstructure Determination of Polybutadiene by ^{13}C NMR', *Polym. Comm.*, 1983, Vol. **24**, P203-205.

10 A. D. H. Clague, J. A. M. van Broekhoven and L. P. Blaaow, '^{13}C Nuclear Magnetic Resonance Spectroscopy of Polydienes, Microstructure of Polybutadiene', *Macromolecules*, 1974, Vol. 7, P348-354.

11 D. J. Patterson and J. L. Koenig, 'Peroxide Cross-linked Natural Rubber and cis-Polybutadiene - Characterization by High-Resolution Solid-State Carbon-13 NMR', *A.C.S. Symp.*, 1984, Vol. **243**, P205-232.

12 K. F. Elger, G. Quack and B. Stutzel, 'On the Structure of Polybutadiene:4. ^{13}C N.M.R. Spectrum of Polybutadienes with cis-1,4-, trans-1,4- and 1,2-units', 1975, *Polymer*, Vol. **16**, P154-156.

13 H. J. Harwood, 'Characterization of the Structures of Diene Polymers by NMR', *Rubber Chem. & Technol.*, 1982, Vol. **55**, P769-808.

14 F. A. Bovey, 'Chain Structure & Conformation of Macromolecules', Pub. Academic Press, 1982.

15 H. Wang, T. W. Bethea and H. J. Harwood, '^{13}C-NMR Spectra of Isomerized Polybutadienes', 1993, *Macromolecules*, Vol. **26**, P715-720.

16 J. C. Randall, 'The Distribution of Stereochemical Configurations in Polystyrene as Observed with ^{13}C NMR', 1975, *J. Polym. Sci., Polym. Phys. Ed.*, Vol. **13**, P889-899.

17 H. Sato, Y. Tanaka and K. Hatada, '^{13}C NMR Spectra of Diastereomers of Styrene Pentamer', 1982, *Makromol. Chem. Rapid Commun.*, Vol. **3**, P175-179.

18 Tonelli A. E., 'Stereosequence-Dependent ^{13}C NMR Chemical Shifts in Polystyrene', *Macromolecules*, 1983, Vol. **16**, P4-16.

19 B. Jasse, F. Laupretre and L, Monnerie, 'Analysis of Carbon-13 Nuclear Magnetic Resonance Spectrum of Polystyrene by Means of Model Molecules', *Makromol. Chem.*, 1977, Vol. **178**, P1987-1992.

20 H. N. Cheng, 'NMR Characterization of Polymers', Reprint. 'Modern Methods of Polymer Characterization', Chap. No. 11, Pub. Wiley & Sons, Inc., 1991.

21 Tonelli A. E., 'NMR Spectroscopy & Polymer Microstructure - The Conformational Connection', Pub. VCH, 1989.

22 D. H. Williams and I. Fleming, 'Spectroscopic Methods in Organic Chemistry', Fourth Ed., Pub. M^{c}Graw & Hill, 1989.

23 'Guide to the NMR of Polymers', Ed. W. W. Simons and M. Zanger, Pub. Sadtler Research Laboratories Inc., 1973.

24 F. A. Bovey, 'High Resolution NMR of Macromolecules', Pub. Academic Press, 1972.

25 E. R. Santee, R. Chang and M. Morton, '300 MHz Proton NMR of Polybutadiene: Measurement of cis-trans Isomeric Content', *Polym. Lett. Ed.*, 1973, Vol. **11**, P449-452.

3.1 The WRAC[1]

The WRAC - Wideline, Relaxation And Cryogenic spectrometer is a home-built spectrometer. Results obtained from the WRAC allow determination of proton relaxation times - T_1, $T_{1\rho}$ and T_2*. The excellent relative abundance of protons in organic solids makes the spectrometer measurement time short. This allows study of a large number of relaxation rates or relaxation times over a short period of time. As the name suggests, the WRAC can study systems that have very different relaxation times - usually a narrow and wide line component (or regions of slow and fast rates of decay). Systems that fall into this category include heterogeneous polymer systems (crystalline and amorphous regions), absorbates (absorbed and non-absorbed species) and block copolymers (mobile and rigid regions). The WRAC has the ability to discriminate between differently relaxing components within a sample and facilitates calculation of their respective relaxation times.

3.1.1 The WRAC Spectrometer

The basic schematic for the spectrometer is shown in Fig. 3.1-

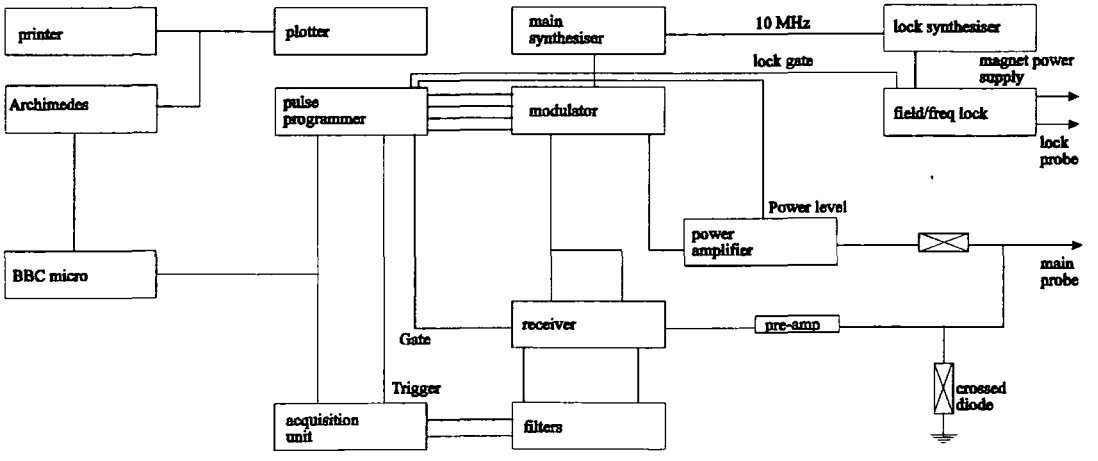

Fig. 3.1 Schematic of the WRAC Spectrometer, Electronics and Control.

The electromagnet is water-cooled and operates at a frequency for protons of 59.99598 MHz. The probe allows ~0.5 cm^3 of sample within a 7.5 mm OD flat-bottomed glass tube. A 1.5 μs pulse duration achieves a $\pi/2$ nutation angle. The lock system consists of a sample of water doped with copper (II) chloride, which is in close proximity to the sample coil. This helps minimise differences in the magnetic field environment around the sample and the lock material. It is necessary to switch off the lock signal during irradiation with an rf pulse and during data acquisition. This avoids cross-talk occurring, since both the lock and spectrometer synthesizers use a similar radiofrequency.

The hardware consists of a pulse-programmer that controls the gating of the spectrometer radiofrequency. The acquisition unit collects the signal and noise data and transfers it to a BBC microcomputer. which co-adds the tansients. At the end of the experiment the data is transferred to the Acorn Archimedes A440 microcomputer. This allows investigation of the data using statistical analysis tools available on the Archimedes computer.

Butan-1,4-diol is the preferred reference material used in the tuning and phasing procedures, at room temperature, and measurement of T_1 and $T_{1\rho}$ values help establish the accuracy of the spectrometer. The probe requires tuning (for each sample) by the use of a directional coupler, in order to minimise the reflected power from the probe. This allows discrimination between the carrier frequency and the signal from the sample. Probe tuning consists of redirecting the signal from the pre-amp into an oscilloscope and minimising the reflected power obtained from the probe by reducing the amplitude of the rf observed on the oscilloscope.

The tuning sequence achieves two things -

1 The power is set for nutating proton nuclei using a 1.5 μs pulse. This is set for all four axes of phase space, i.e., nutating the bulk magnetisation in the +/- x- and +/- y-axes.

2 The spinlock frequency is set so that it is aligned with the x-axis. This prevents any other types of relaxation to occur other than $T_{1\rho}$.

The reference sample - butan-1,4-diol - is a viscous liquid so measurement of T_1, $T_{1\rho}$ and T_2 values should result in equivalent values, since viscous liquids are still at the extreme narrowing limit (as with non-viscous liquids), where $T_1=T_{1\rho}=T_2$. At room temperature all the relaxation times should be equal to 170 ms.

Finally, the sample, under investigation, is placed within the electromagnet and the probe is tuned using the procedure mentioned for butan-1,4-diol. This results in accurate determination of the sample's relaxation behaviour.

3.1.2 The Software

The software utilised by the WRAC is written in Archimedes BASIC Five. The spectrometer is controlled by a central library of commands which are defined in a global program called 'ACQ'. When an experiment is set-up a Basic program is executed which generates the instructions to be down-loaded to the pulse-programmer via the BBC microcomputer and then appends this pulse program to the ACQ program. This makes programming of the WRAC a relatively simple process and minimises correction to the main controlling program - ACQ.

3.1.3 Statistical Fitting

Statistical analysis has played an integral role in my research. The WRAC generates a statistical fit using a nonlinear least-squares maximum likelihood estimator routine.

The principle behind fitting techniques is the analysis of real data values compared to simulated values. Variance is the standard indicator of fitting techniques. It

is derived from the sum of the differences between each simulated data point and the corresponding data point and represents the difference per data point, i.e.

$$\text{Variance} = \frac{1}{n-1}\sum_{i=1}^{n}\left(x_i - \bar{x}\right)^2 \text{ for n data points with a mean value of } \bar{X}. \qquad \text{Eqn. 3.1}$$

A better description is the standard deviation per data point which is the root of the variance. However, this relies on a constant standard deviation per data point so does not account for transient inconsistencies occurring whilst acquiring data. A more dependable description is chi-squared - χ^2 - which uses a different deviation per data point. Thus, if the deviation is large for one data point (described as an outlier), then it does not have an equal weighting so the deviation of this point will not contribute to the total variance. With a series of N data points (x_i,y_i), where i=1 to N, modelling M adjustable parameters a_j, j=1...M, chi-squared is then defined as-

$$\chi^2 = \sum_{i=1}^{n}\left[\frac{y_i - y(x_i; a_1 \ldots a_m)}{\sigma_i}\right]^2 \qquad \text{Eqn. 3.2}$$

Here the standard deviation is considered for each point. $a_1 \ldots a_m$ describes the number of adjustable parameters for the data sets which in this example are x and y. The fitting procedure requires minimisation over the range $a_1 \ldots a_m$ or

$$\sum_{i=1}^{N}\left[y_i - y(x_i; a_1 \ldots a_m)\right]^2 \qquad \text{Eqn. 3.3}$$

This is the maximum likelihood estimator.

The WRAC analyses the data is terms of a given particular set of parameters, and tries to describe what is the probability that this data set could have occurred. Now suppose each y_i data point has a random Gaussian distribution error and the standard

deviation - σ - if deviations of the errors is the same then the probability of a set of data points is their product-

$$P = \prod_{i=1}^{N} \left\{ \exp\left[-\tfrac{1}{2}\left(\frac{y_i - y(x_i)}{\sigma} \right)^2 \right] \right\} \Delta y \qquad \text{Eqn. 3.4}$$

Δy is a fixed error on each data point. Taking logarithms of this probability makes it easier to manipulate and has no effect on the result. If each point has its own standard deviation - σ_i - then-

$$\chi^2 = \sum_{i=1}^{N} \left(\frac{y_i - y(x_i; a_1 \ldots a_m)}{\sigma_i} \right)^2 \qquad \text{Eqn. 3.5}$$

This can be minimised through differentiation to give-

$$\sum_{i=1}^{N} \left(\frac{y_i - y(x_i)}{\sigma_i^2} \right) \left(\frac{\partial y(x_i; \ldots a_k \ldots)}{\partial a_k} \right) = 0 \text{ Where } k=1 \ldots M \qquad \text{Eqn. 3.6}$$

The WRAC has two statistical routines available for analysis of data. These routines are Simplex and Marquardt non-linear least squares fitting routines. Both procedures have their advantages and disadvantages depending upon the nature of the data being processed.

3.1.3a The Simplex Algorithm[2]-

Simplex is a nonlinear least-squares fitting routine which uses the criterion that the sum of the squared residuals (SS_R) is minimised. If the data are dependent on a parameter y and there are n data points then the sum of the squared residuals is defined as- $SS_R = (y_1-y_1')^2 + (y_2-y_2')^2+\ldots(y_n-y_n')^2$. If the error distribution is not random, but

known, then it is given a statistical weighting, i.e. $S_i w_i(y_i-y_i')^2$ (in our case the weighting is constant).

The Marquardt algorithm uses Newton Ralphson and steepest descent algorithms - this avoids the divergence problem but requires substantial programming which, however results in no real loss in speed. The Newton Ralphson alogrithm analyses the partial differentials of SS_R until they are close to zero (BUT this can cause divergence if using inaccurate initial guesses). The algorithm then creates a square matrix that contains all the second derivatives of SS_R, invertes the matrix and multiplies it by the values of the first derivatives to give a variable that is continually checked during each iteration step.

The Simplex algorithm allows convergence even from very inaccurate starting values. A simplex is a geometric figure that has one more vertex than the space in which it is defined has dimensions, e.g. a simplex on a two-dimensional plane is a triangle and in three-dimensional space is a tetrahedron. Building a simplex in the M+1 dimensional space is defined by the parameters that are to be fitted. In a two-dimensional case the vertex is a triangle. The algorithm creates other vertices through reflection, expansion, contraction and shrinkage of the original vertex. The system then finds which vertex has the worst response (highest value) and rejects it to substitute it for another vertex. Examples of vertex operations include:

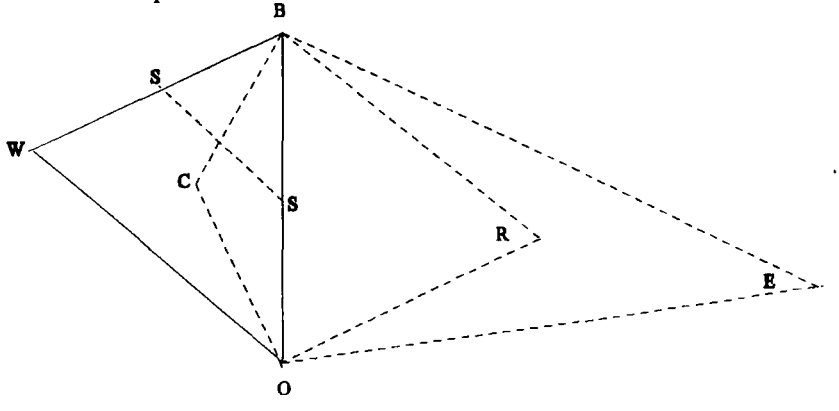

Fig. 3.2 Simplex operations where BWO represents the original simplex with B being the vertex. W is the worst vertex, R is a reflected vertex, E is an expanded vertex, C is a contracted vertex and S are the vertices of a shrunken vertex.

A reflected vertex is created at a distance 'd' from the worst vertex to M (the midpoint of all the other vertices), and then the same distance to create the reflected vertex. An expanded and contracted vertex is created at 2d and d/2 respectively from the value of M but only if the reflected value is rejected.

The overall advantages of the Simplex method are-

1 Divergence is impossible.

2 Calculation of the response value occurs only once or a few times for each iteration.

3 There is no need for derivatives and numerical differentiation.

4 No matrix operations are involved.

3.1.3b The Marquardt-Levenberg Method[3]-

This method requires the minimisation of the first derivative of chi-squared as with other nonlinear least-squares techniques. The first derivative is described as-

$$\frac{\partial \chi^2}{\partial a_k} = -2\sum_{i=1}^{N} \frac{\left[y_i - y(x_i;a)\right]}{\sigma^2} \frac{\partial y(x_i;a)}{\partial a_k} \quad \text{Where } k=1,2,\ldots,M \qquad \text{Eqn. 3.7}$$

Then taking another partial derivative gives-

$$\frac{\partial^2 \chi^2}{\partial a_k \partial a_l} = -2\sum_{i=1}^{N} \frac{1}{\sigma^2}\left[\frac{\partial y(x_i;a)}{\partial a_k}\frac{\partial y(x_i;a)}{\partial a_l} - \left[y_i - y(x_i;a)\right]\frac{\partial^2 y(x_i;a)}{\partial a_k \partial a_l}\right] \qquad \text{Eqn. 3.8}$$

The first and second derivatives are now used to create either an inverse Hessian matrix (if the initial guess is far from the minimum) or are used in a steepest descent method - where if the initial guess (a_{cur}) is near the minimum then χ^2 can be

approximated to a quadratic function so that the next value (a_{min}) of the parameter a can be described as-

$$a_{min} = a_{cur} + D^{-1}\left[-\nabla\chi^2(a_{cur})\right] \qquad \text{Eqn. 3.9}$$

This is called an inverse Hessian matrix method where D is a matrix whose elements are the first derivatives of χ^2 for every parameter a. Now, if $[\alpha]=1/2D$ then this results in a sum of a series of linear equations-

$$\sum_{k=1}^{M}\alpha_{kl}\delta a_l = \beta_k \qquad \text{Eqn. 3.10}$$

where $\beta_{kl} = \frac{\partial^2\chi^2}{2\partial a_k}$ and $\alpha_{kl} = \frac{\partial^2\chi^2}{2\partial a_k \partial a_l}$ (this simplifies the second derivative equation for chi-squared).

However, what happens if the first guess of χ^2 is not near the minimum? The equation of χ^2 is not a quadratic anymore but an iterative routine can be used - called the steepest descent method. The basis of this method is the use of the equation-

$$a_{next} = a_{cur} - \text{constant}.\nabla\chi^2(a_{cur}) \qquad \text{Eqn. 3.11}$$

Here ∇ is a gradient function. This can be also described in terms of linear equations- $\delta a_l = \text{constant}.\beta_l$.

The Marquardt-Levenberg method tries to cross the gap between these two techniques so that the initial fit can be improved by the iterative routine of the steepest descent method and when nearer the minimum the inverse Hessian method comes into the fitting procedures. The Marquardt method accounts for the two potential problems in the steepest descent method-

1 The constant used in the equations is a completely unknown quantity

2 χ^2 is multidimensional (i.e. β_k has dimensions of $1/a_k$ so $\delta a_l \beta_l$ has units of $1/a_k^2$). The only components that are consistent with these units are the diagonal elements (with dimensions $1/\alpha_{kk}$) of the matrix [α]. However, these units may be on such a scale that the numerical values of a may be dwarfed in comparison. This nonlinear method uses a factor λ which can help prevent this problem. Wherefore, this results in-

$$\delta a_l = \frac{\beta_l}{\lambda a_{ll}} \qquad \text{Eqn. 3.12}$$

This method links the steepest descent and inverse Hessian matrix methods by defining a new matrix a` which has the properties-

$$\alpha'_{jj} = \alpha'_{jj}(1+\lambda) \text{ and } \alpha'_{jk} = \alpha_{jk} \ (j^1k) \qquad \text{Eqn. 3.13}$$

Thus, the sum of linear equations becomes-

$$\sum_{l}^{M} \alpha'_{kl} \delta a_l = \beta_k \qquad \text{Eqn. 3.14}$$

When λ is very large, then α` becomes diagonally dominant and so becomes the steepest descent method, but when λ approaches zero then the equation goes to the inverse Hessian matrix method.

Overall, the recipe for the Marquardt method is-

- Compute $\chi^2(a)$
- Pick a value of λ such as λ=0.001
- Solve the linear equations $\sum_{l}^{M} \alpha'_{kl} \delta a_l = \beta_k$ for δa and evaluate $\chi^2(a+\delta a)$
- If $\chi^2(a+\delta a) \geq \chi^2(a)$ then increase λ by a factor of 10 and solve for δa

• If $\chi^2(a+\delta a) < \chi^2(a)$ then decrease λ by a factor of 10 and go back from $a+\delta a \rightarrow a$ and solve again for δa.

The criterion used by the WRAC to stop this iteration is the χ^2 parameter or the SS_R (sum of standard deviations). It reaches the inverse Hessian matrix method and achieves a very large value of λ so the SS_R does not change.

3.1.4 Pulse Programs

The WRAC has a number of pulse programs that can analyse the proton relaxation behaviour of many solid-state samples. The initial sequence of events when studying a sample is to acquire an FID using the pulse program SPECEC and determine the T_2* relaxation behaviour. Next the T_1 relaxation time(s) are measured using the sequence called INVREC and subsequently determine the $T_{1\rho}$ behaviour using the programs T1RCATSE, T1RFIDSE and T1RHOSE.

a) Solid Echo Sequences[4]

SPECEC - This pulse sequence consists of a $90°_y$ (t_w) nutation pulse followed, after an echo delay, by a $90°_x$ echo pulse. This extra $90°_x$ echo pulse refocuses the magnetisation so that detection is effectively made at zero time. This can be more easily seen in Fig. 3.3 (next page)-

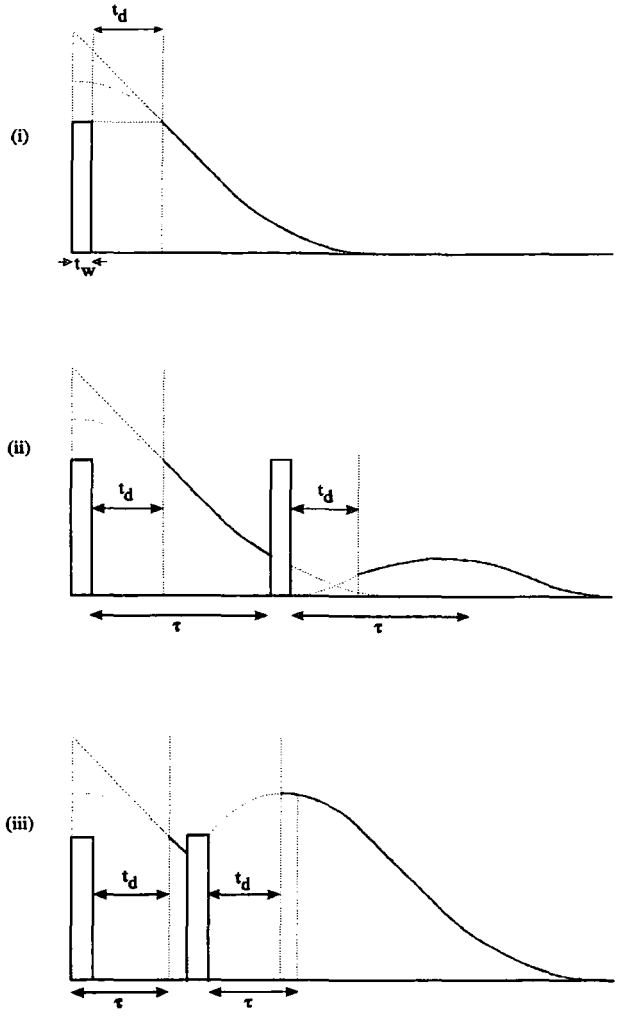

Fig. 3.3 (i) The Bloch decay is obscured by the dead time t_d of the receiver.

(ii) The echo delay t is longer than the dead time but comparable to T_2 so the echoed Bloch decay is attenuated.

(iii) An efficient echo with a maximum simulating the true Bloch decay.

The aim of this experiment is to obtain a signal which can be transformed into the frequency-domain spectrum without distortion from the rf transmitter/receiver. This is achieved with the use of a solid echo. Generally, because of the difficulty in analysis of the transformed spectrum, it is convenient to study the time-domain signal (Free

Induction Decay). The magnitude of the echo delay is generally of the order of 10 μs but in subsequent studies this has been extended up to 2 ms.

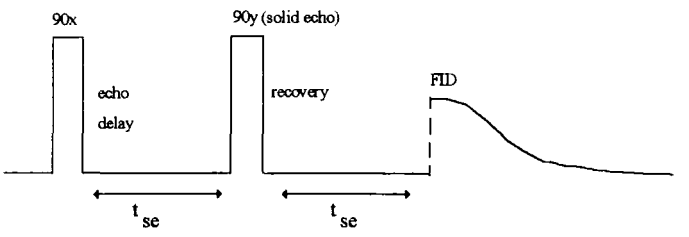

Fig. 3.4 Pulse sequence for detection of an FID with a solid echo.

This echo sequence can only be successfully described by density matrix functions. The density matrix is a tool that is used to describe more fully the vector description of bulk magnetisation. It describes the state of a spin ensemble whilst being acted upon by an operator as well as its evolution time. It achieves this by relating the state of a few spins to the statistical treatment of a large ensemble of spins. The density matrix is an array of numerical coefficients that describe the wavefunctions/states of all the spins within the ensemble of spins.

The equilibrium spin density matrix when in a magnetic field is denoted by - $\sigma(0)=I_Z$. After a 90° pulse, which is applied along the rotating y-axis, the spin density matrix is altered to $\sigma(0+)=I_X$. The spin Hamiltonian, in the rotating system, is $\hbar\mathcal{H}$ so the density matrix at a time t later is-

$\sigma(t) = e^{-i\mathcal{H}t} I_x e^{i\mathcal{H}t}$ and the expectation value in the rotating y-axis $\bar{I}_y=0$.

Thus, the observed signal is proportional to $\bar{I}_x$ or $Tr(I_x\sigma)$. This results in the Bloch decay after a $90°_y$ pulse as-

$$\bar{I}_x = TrI_x e^{-i\mathcal{H}t} I_x e^{i\mathcal{H}t} \qquad 3.15$$

Normalising this to a unit signal at time t=0 follows as-

$$V(t) = Tr(I_x e^{-i\mathcal{H}t} I_x e^{i\mathcal{H}t}) / TrI_x^2 \qquad 3.16$$

The exponential terms can be expanded to give-

$$e^{-iQt}Pe^{iQt} = P + it[P,Q] - t^2/_{2!}[Q,[Q,P]] + \ldots \quad 3.17$$

so this results in-

$$V(t) = 1 + \frac{t^2}{2!}\frac{Tr[\mathcal{H},I_x]^2}{TrI_x^2} + \frac{t^4}{4!}\frac{Tr[\mathcal{H},[\mathcal{H},I_x]]^2}{TrI_x^2} + \ldots \quad 3.18$$

Thus, Bloch decay can be described by second moments M_{2n} of the steady state absorption line-

$$V(t) = 1 - \frac{t^2}{2!}M_2 + \frac{t^4}{4!}M_4 - \ldots \quad 3.19$$

If after the $90°_y$ pulse the system has evolved for a time τ then after a $90°_x$ pulse it evolves for a time τ' so the final Bloch decay can be written as-

$$V(\tau+\tau') = Tr\{I_x e^{-i\mathcal{H}\tau'} S^{-1} e^{-i\mathcal{H}\tau} i_x e^{i\mathcal{H}\tau} S e^{i\mathcal{H}\tau'}\}/Tr\{I_x^2\} \quad 3.20$$

Where $S=\exp(-1/2i\pi I_x)$ - the Bloch decay for the period τ'. This can be rewritten as-

$$V(\tau+\tau') = Tr\{(e^{i\mathcal{H}\tau'} I_x e^{-i\mathcal{H}\tau}) S^{-1} (e^{-i\mathcal{H}\tau'} I_x e^{i\mathcal{H}\tau}\}/Tr\{I_x^2\} \quad 3.21$$

Which can be expanded to give the following truncated Hamiltonians-

$$V(\tau+\tau') = \left\{1 + \frac{(\tau-\tau')}{2!}\frac{Tr[\mathcal{H},I_x]^2}{TrI_x^2} + \frac{(\tau-\tau')}{4!}\frac{Tr[\mathcal{H},[\mathcal{H},I_x]]^2}{TrI_x^2} + \ldots\right\} \quad 3.22$$

Notice the two truncated Hamiltonians' first three terms are the same as the standard Bloch decay i.e., it is centered around the time 2τ (i.e. $\tau=\tau'$). This indeed shows that the $90°_x$ pulse does recover the magnetisation to create a zero-time signal response.

The resultant FID is then modelled by the statistical functions present in the WRAC software.

(b) Inversion Recovery

INVREC is the pulse program that measures T_1 by inversion recovery. This consists of irradiating a sample with a 180° pulse, waiting a time τ_r and then applying a second 90° pulse to move the magnetisation into the detection axis. The WRAC then samples the first point of the FID and repeats the sequence with twice the value of τ_r, then three times the value of τ_r in the sequence and so on. The resultant rate of signal recovery from the negative to positive detection axes is analysed in order to investigate its dependence on $n\tau_r$ and then fitted to a number of exponential functions. Since polymer systems are heterogeneous, and, in diblock copolymers, have more than one polymer species present, then more than one exponential function can be expected for the signal rate of recovery, and thus more than one value of T_1 can be determined.

The irony of this sequence is that after each detected point the system needs to wait for a time of $5T_1$ to allow the magnetisation to align with the z-axis (the static magnetic field). Other restrictions include the need for a sampling rate that is sufficient to detect a number of points before crossing the null point and that the last sampled points should level off sufficiently to determine the magnetisation's equilibrium value.

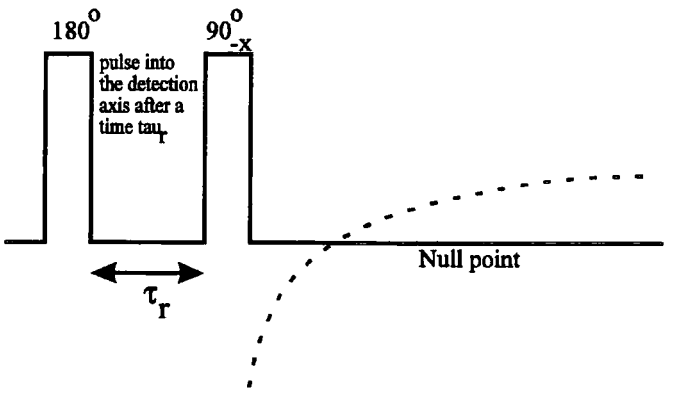

Fig. 3.5 Pulse sequence for the inversion recovery measurement of T_1

(c) Spin-locking

The general pulse sequence for T1RHOSE, T1RHOFIDSE and T1RCATSE, with the spin-lock time in an order of magnitude between 0.5 ms to 30 ms is-

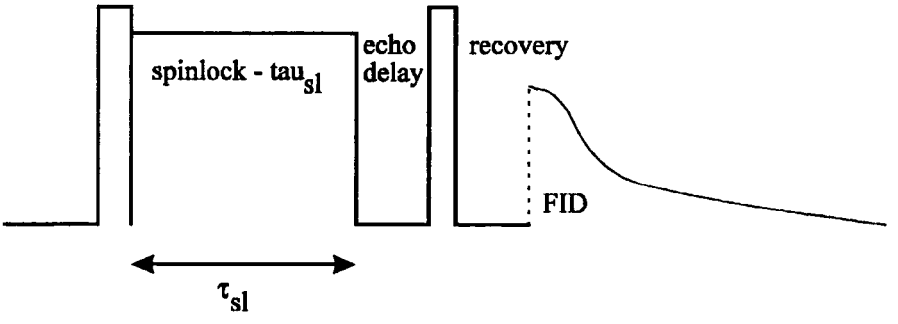

Fig. 3.6 Pulse sequence using a spin-locking field.

T1RHOSE is a pulse program consisting of incrementally increasing the spin-lock time τ_{sl} and analysing the decay of the first sampled point of the FID as a function of τ_{sl} after irradiating the sample with a 90° solid echo pulse. This sequence is used to study the number of $T_{1\rho}$ values present. A limitation of this sequence is that the increment of the spin-lock time has to be sufficient to sample enough of the decay but be long enough for the decay to reach the null point (zero population). However, long spin-lock times are not available due to heating effects on the sample being analysed and deleterious effects on the spectrometer hardware!

T1RHOFIDSE is a measurement of the FID after spin-locking the sample followed by a solid echo. This is an identical sequence to T1RHOSE but acquiring the full FID. This is used to correlate modelled FID components to $T_{1\rho}$ components. At long values of τ_{sl} the FID will correspond mainly to that of the long $T_{1\rho}$ component.

T1RCATSE consists of irradiating the sample with a $90°_x$-$90°_y$ solid echo pulse sequence, as with T1RHOSE and T1RHOFIDSE, then sampling the first point of the FID. This sequence is continued using incrementally longer spin-lock times and sampling again the first point of the FID. However, the incremental increase of the spin-lock time is not constant but concatenated by using short, medium and long increment times in spin-locking duration (τ_{sl}). This is used to try and accurately fit exponential functions to the FID. Because of the uneven incremented spin-lock times the fast and slow decays present in the FID can be analysed in more detail.

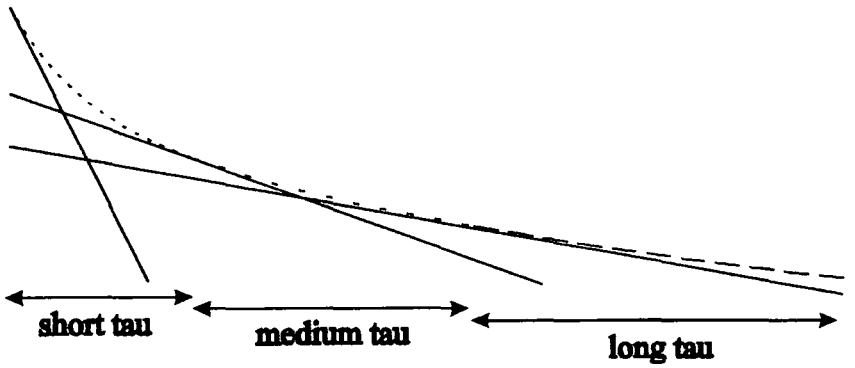

Fig. 3.7 Concatenated FID with three time ranges and three fitted exponential lines. Unpeeled data is not shown.

This diagram shows the fitted exponential relaxation times on a logarithmic scale. The WRAC first finds the best fit to one component. It then subtracts the simulated component points from the data points - this is known as unpeeling the data - and the resultant points undergo the same fitting procedure until all that can be fiitted is noise. The concatenated spin-lock times mean that all the components are characterised equally.

3.1.5 Determination of Accuracy and Precision of WRAC Data

Prior to this investigation continual experiments on the WRAC showed randomly periodic background signals which were either internal - from electronic components - or external - from an rf source. If internally produced then the noise is stochastic - a series of random fluctuations in the noise level and frequency. If externally produced then the noise is non-stochastic - consisting of a periodic fluctuation in the noise level and frequency (such as a sinusoidal oscillation). These experiments were achieved by writing a BASIC computer program to analyse the signal from the probe containing only an empty glass sample tube and then to see if the distribution of rf signals was of standard Gaussian type - hence showing stochastic noise. The program created a bar chart showing the distribution of frequencies/amplitudes of the background noise sampled, and indeed it was found to be the case that the noise was of a Gaussian distribution. Unfortunately, this meant that the WRAC's components needed to be analysed to remove this random noise generation (or minimise it) but it was much easier compared to trying to find an external rf generating source. After some other setbacks such as fluctuations in the rf amplitude generated and signal amplification, the WRAC was then able to give consistent results.

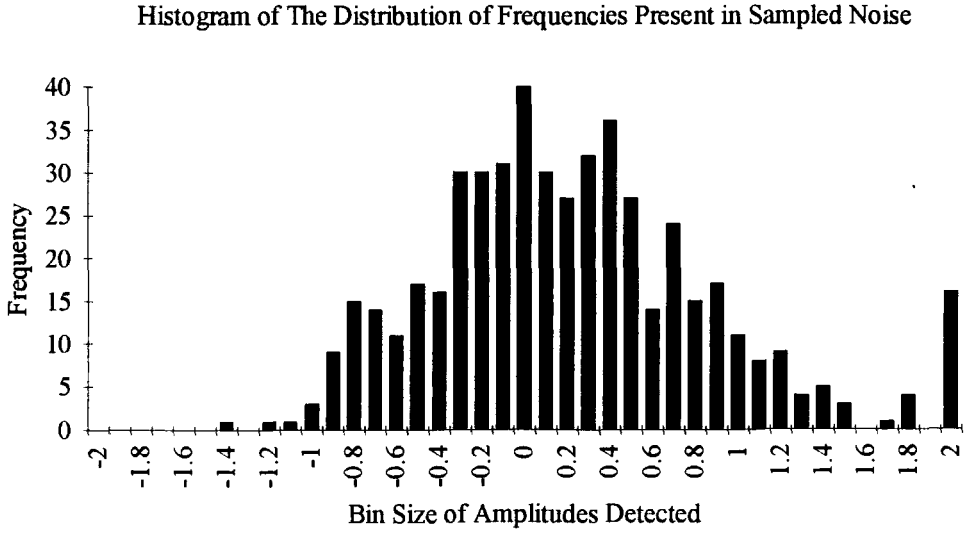

Graph 3.1 Distrubution of Actual Noise From The WRAC Around a Null

The output from the WRAC consists of four areas (Spectrum 3.1)-

1 The FID (top left hand corner), usually shown pictorially to be fitted to a number of statistical components. If for a relaxation measurement, then this area is usually depicted as a series of exponential lines. The signal axis is logarithmic so any exponentials appear linear.

2 The deviation from the applied model (bottom left). This shows the deviation of the FID data points from the model and graphically gives an idea of errors occurring - such as offset effects and mechanical faults. The m-residue/rms-residuals value gives a numerical indication of the goodness of fit, which needs to be minimised. If the integrated residues deviate sinusoidally from the null-line or drifts significantly from the null-line then another component needs to be fitted or a baseline is necessary.

3 The top right hand side depicts the model parameters as absolute populations, relative populations and time constants (relaxation times) for the particular statistic (inverse of the rates of decay) and the standard deviation. With a Weibullian function, one also has the index of the power shown (between 1-Lorentzian and 2-Gaussian).

4 The bottom right hand side shows the parameters used in the experiment. Standard deviation-squared and the Q-value both describe the goodness of fit by the data to the model (0.5 perfect fit, 0 wrong model, 1 too good a fit). The Q-value determines how the residual noise left after fitting procedures compares to the noise sampled before the acquisition of the decay data. If Q=0 then the residual noise still contains a statistical component or a baseline but if Q=1 then the residual noise is less noisy than the pre-acquisition sampled noise.

Spectrum 3.1 Example of WRAC Spectral Output. An Unpeeled FID.

3.1.6 Weibullian, Gaussian and Exponential Statistical Modelling Functions

The exponential function is defined as $\exp(-t/T_2)$ and the Gaussian is defined as $\exp-(t/T_2)^2$. The Weibull function is defined as- $\exp[-(t/T_2)^N]$, where N is the Weibullian coefficient, which can be between 1 and 2. Each one of these functions has a different lineshape in the transformed frequency domain spectrum and can occur both singly and in conjunction with each other. This implies that when a quantity T_2 is mentioned in this thesis it may not have the mathematical meaning associated with the Lorentzian-based solution-state T_2 from lineshape analysis.

3.2 Results

Experimental Investigations

The initial program of work on the WRAC was to try and study the FID of TK124 and determine the relaxation parameters of the sample. Then, the next goal was to try and model the FID using well-known statistical functions to try and correlate the functions to the diblock copolymer components.

The relaxation parameters analysed were T_1^H and $T_{1\rho}^H$. Using the inversion recovery pulse program the T_1^H for the isoprene-based polymer was found to be 720 ms (± 40 ms), from the WRAC

$T_{1\rho}^H$ from the WRAC was 6 ms (± 0.1 ms). The WRAC appeared to fit a single exponential to the decay of the proton FID signal as a function of incrementally increasing the spin-lock.

After a number of experimental discrepancies - such as variation in signal output from the amplifier, rf frequency 'ringing' resulting in sinusoidal oscillations in the FID detected (caused by breakthrough of the lock signal into the probe signal) and problems with the feedback loop used to maintain a constant lock signal - a sequence of investigations was undertaken to try and analyse more closely the relaxation of two components within polymer systems and eventually observe and analyse spin diffusion. The work concentrated on the newly synthesised polymer - SB5 (polystyrene-b-butadiene gyroid). The experiments that were completed were as follows-

1 Effect of pre-acquisition delay (denoted recovery time) on the FID (pulse program SPEC) to identify the minimum value without pulse breakthrough and maybe see the effect of spin-spin relaxation.

2 Effect of solid-echo delay on the ^1H FID (pulse program SPECEC) - to try and extrapolate to zero echo delay and compare actual statistical populations to components within the polymer.

3 Effect of variable spin-lock time to selectively analyse the fast and slow decaying components within the FID and to set up an analogous two-dimensional experiment (pulse program T1RHOFIDSE relates values of T_2 to those of $T_{1\rho}^H$).

4 Determination of $T_{1\rho}^H$ (analysed in terms of components) using the pulse program T1RHOSE.

5 Pulse program T1RCATSE - to analyse the first point of the FID using different dwell times-

short dwell - to analyse the fast decaying component
medium dwell - to analyse the fast and slow decaying components
long dwell - to analyse the slow decaying component

This can then be used in the analogous two-dimensional experiment.

First the relaxation characteristics of the polymer were analysed and the following results were obtained-

T_1 = 186 ms (baseline of 0.2% - to account for errors in M_0 and Q = 1). The Q-value of 1 signifies, as discussed above, that the fit is too good to be true (see Section 3.2.2 for explanation). The WRAC also uses another baseline to reflect the data vertically into a more recognisable exponential decay. This baseline is not shown in the spectral output but is determined by the WRAC as the signal from the last acquired point in the T_1 experiment.

$T_{1\rho}^{H}$ (mobile) = 24.0 ms (Q = 0.754 - 66% of the signal population). This correlates well to the 67% composition of polybutadiene within the copolymer SB5.

$T_{1\rho}^{H}$ (rigid) = 4.8 ms (Q = 0.754 and 34% of the signal population).

The $T_{1\rho}^{H}$ results further confirm that the rigid - fast decaying - component is the polystyrene moiety and the mobile - slowly decaying - component is the polybutadiene moiety.

3.2.1 Effect of Recovery Time on a Standard Spectrum

These experiments showed that receiver breakthrough occurred at times less than 7 μs. Thus, 8 μs were used as a standard throughout the rest of the experiments.

3.2.2 Effect of Echo Delay on FID Components Measured

The resultant FID was found to be successfully modelled by the three functions - a Weibullian, a Gaussian and an exponential function. The criterion of goodness of fit was based on minimising the standard deviation squared and optimising the Q-value.

The Q-value describes the validity of the fit to the data. If the value is close to zero then the model could have just as easily been modelled to random noise as to the FID data set. If approximately 0.5 then the model directly correlates to the FID data, but values approaching 1 show that the model is too good to be true! Q is a function of χ^2 (equivalent to the summed standard deviations squared SDSQ) - the probability that the observed χ^2 will exceed the value of χ^2 obtained when sampling the residual noise before the experiment even for a correct model. Q also equals 1-P, where P is the probability of obtaining the experimental data by random chance, so if Q=0 then the modelled data could have just as easily have been generated by noise and if Q=1 then there is no possible way of generating the residual noise data by random noise but if equal to 0.5 then the residual noise actually is noise and not an unmodelled statistical component.

The values obtained during this experiment were all of a value of 1 but the WRAC seems to be incorrect in sampling noise in comparison to the FID data. The noise is sampled without the effect of rf pulses, before the experimental run. Therefore, if the residual noise is modified by the use of rf pulses then the noise sampling method results in a different type of Gaussian distribution compared to the pulse sequence residual noise. This gives a value of Q=1 since the residual noise in the FID has a different magnitude and distribution of noise compared to the initial sampling of noise before the experiment, and not due to modelling that is too good to be true!

The Weibullian models particularly consistently to the long-time decaying component (with a Weibullian index of 1.46 (±0.03), whilst the Gaussian and exponential functions combined, represent the faster decaying component. Comparison of the relative populations of the various functions during the initial stages of the experiment show that the Weibullian (long-time decaying component) is the polybutadiene component (67% in composition) and the combined Gaussian and exponential components correlate to the polystyrene function within the copolymer.

Table 3.1 Results from experiment 1 - SPECEC - spectrum with a solid echo and the effect of solid echo delay.

Echo delay (us)	Weibullian Population	Weibullian time (ms)	Gaussian + Expo Pop.	Gaussian time (ms)	Exponential time (ms)
0	452	0.97	250	0.018	0.021
5	455	0.96	209	0.01.7	0.021
10	455	0.97	168	0.01.7	0.023
20	451	0.97	100	0.01.5	0.019
30	448	0.96	50.	0.01.5	0.024
40	441	0.94	28	0.01.4	0.029
50	440	0.95	14.8	0.01.7	0.028
60	437	0.93	11.4	7.7E	0.029
80	427	0.92	7.5	-----	0.042
100	423	0.92	4.1	-----	0.023
200	373	0.86	1.4	-----	0.088*

* - deviation due to the statistic modelling to the noise.

Each one of these experiments had a receiver delay of 8μs which is applied after the end of the last pulse. Therefore, for the first two experiments the effective delay after the echo pulse is 8μs for the 0μs echo delay experiment and 3μs for the 5μs echo delay experiment. The rest of the experiments have the echo delay greater then the receiver delay so the effective delay is the echo delay-

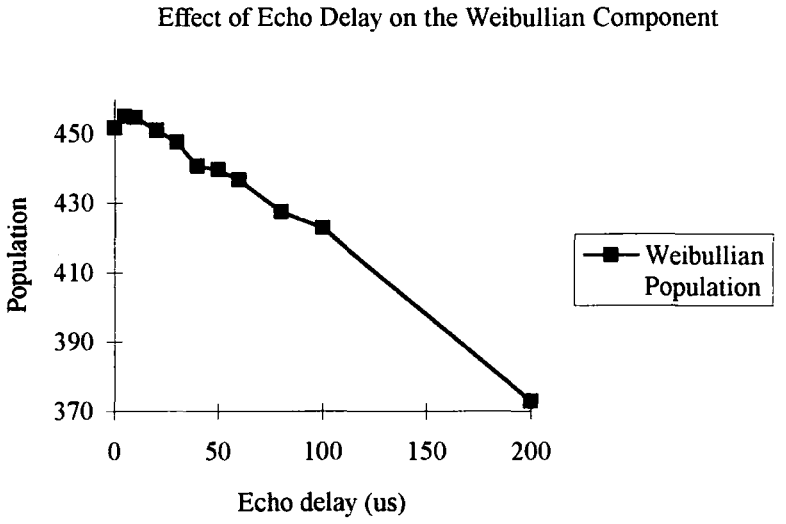

Graph 3.2 Modelled Weibullian Component as a Function of the Echo Delay

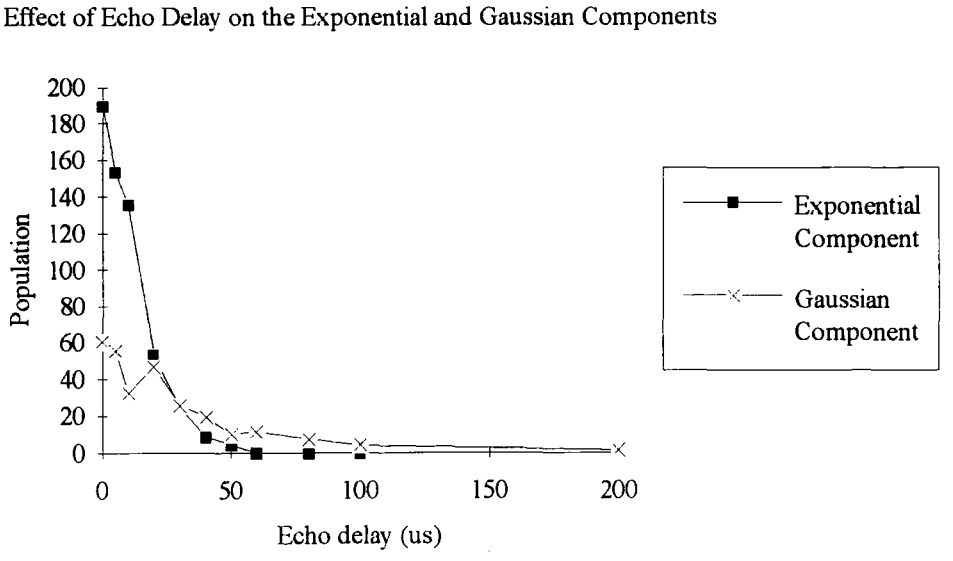

Graph 3.3 Modelled Exponential and Gaussian Components as a Function of the Echo Delay.

One can see that the echo delays which are less than the receiver delay lose the first few of the digitised points of the FID. Therefore, the magnetisation detected is not a true reflection of original magnetisation at the start of the dead time. The minimum time that can recover the full magnetisation is at 10ms. From the table of data (Table 3.1) one can see that little of the Weibullian modelled component is lost but the Gaussian+exponential components combined have decreased by ca. 32% but this procedure is sufficient to recover the true intensity. The decay for all the components can be seen as Gaussian in nature. This shows that the echo delay is recovering the second moment of the magnetisation which, since it is in the solid-state, should be described by a Gaussian distribution.

Plotting the data as a function of $1/(\text{echo delay})^2$ gives a straight line for each of the three functions' paratmeters. The intercepts of the graphs give the true value of the population at zero-time. These values are, according to modelling using the Levenberg-Marquardt non-linear least squares fitting-

Weibullian =448 ± 2

Exponential =260 ± 15

Gaussian =25.5 ± 15

These results show that the zero-time ratios of Weibullian:Gaussian+exponential agree with the actual components of the block copolymer. The actual values are 62:38 of Weibullian:Gaussian+exponential from the zero-time extrapolation compared to 67:33 of the polybutadiene:polystyrene components.

3.2.3 Effect of Spin-lock Time on The Components of T1RHOFIDSE

Spin-lock (ms)	Weibullian	Gaussian + Exponential	Weibullian time (μs)	Gaussian time (μs)	Exponential time (μs)
0.1	427	161	950	16	23
0.5	415	139	960	16	22
1	401	118	960	16	20
2	377	91	970	16	20
5	321	48	980	15	17*
7	292	31	990	15	41*
10	261	20	990	15	99*
20	164	3.2	1000	18	-----

* The effect of low population of a statistic modelling to the noise.

Table 3.2 Effect of spin-lock time on the statistical components modelled during T1RHOFIDSE

This experiment is analogous to two-dimensional experiments - two time-domain axes with the second time-domain being governed by the spin-lock time or relaxation under $T_{1\rho}$ conditions.

This experiment analyses the effect of spin-spin relaxation on the resultant statistical components measured from the decaying FID. The decay of the particular functions shows that the Weibullian FID component models to the slowly decaying $T_{1\rho}$ component whilst the combined exponential and Gaussian functions model to the faster decaying $T_{1\rho}$ (polystyrene) component.

Notice, the consistency of the relaxation rates of the three component under increasing spin-lock delay times. This confirms that the modelled functions are invariant

with increasing spin-lock times and that the WRAC was consistent whilst acquiring the signal during all of the experiments.

The overall relaxation behaviour of this system can thus be modelled as

$$\frac{dM}{dt} = M_w \exp(-t/9.4E-4)^{1.5} + M_g \exp(-t/1.6E-5)^2 + M_e \exp(-t/2.3E-5)$$

M_w= 448 = magnetization from the Weibullian component at time t = 0

M_g= 260 = magnetization from the Gaussian component at time t = 0

M_e= 25.5 = magnetization from the exponential component at time t = 0

The numbers given correspond to the populations obtained from the previous experiment seeing the effect of echo delay on FID components.

These statistics do not necessarily directly correlate to components within the block copolymer, since an infinite number of exponentials could easily model the infinite number of polymer proton nuclei present within the copolymer. However, the criterion of modelling of minimisation of SDSQ and a value of Q=0.5 leads to a perfect fit.

The rate of decay of the three modelled statistics gives information on the spin-locked relaxation rate of the particular statistics. Again modelling the data using the Marquardt non-linear method the following results were obtained-

Weibullian = 21 ms (± 1.2 ms)

Exponential = 5.5 ms (± 0.2 ms)

Gaussian = 1.3 ms (± 0.5 ms)

More information was needed on the spin-locked relaxation times for each component in the copolymer so the pulse program T1RHOSE was the next step. These above values of $T_{1\rho}$ should correlate with the $T_{1\rho}$ components in the next experiment.

3.2.4 The Effect of Spin-lock Time Increment on Exponential $T_{1\rho}$ Components

Spin-lock increment (ms)	Exp. Population Slow decay	Exponential time (s)	Exp. Population Fast decay	Exponential time (ms)
0.1	506	0.015	85	1.5
0.5	400	0.023	179	3.5
1	379	0.024	187	4.3
2	358	0.026	197	5.3
5	365	0.027	171	5.5
7	368	0.028	182	5.2
10	352	0.031	119	8.1

Table 3.3 Results from the effect of spin-lock time on exponential $T_{1\rho}$ components.

This experiment is used to try and optimise the incremental spin-lock time to try and get information about the faster decaying component as well as the slower decaying component. If the sampling rate - which is determined by the spin-lock increment - is below 1 ms then the rate of decay for the fast decaying statistic is 1.5 ms but when the spin-lock time is above 1 ms then the fast decaying statistic has a decay rate of 5 ms. Whether these are two different $T_{1\rho}$ rates of 1.5 ms and ca. 5 ms is not known but it is directly seen for the modelled exponential and gaussian functions in the previous experiment. This experiment does show the importance of the sampling rate for the determination of accurate $T_{1\rho}$ relaxation times. If the spin-lock time increment is too short then the slowly decaying component is inaccurately determined but if too long then not enough of the fast decaying component is sampled. Therefore, an experiment is needed for the determination of $T_{1\rho}$ using and uneven sampling rate (spin-lock time). This is why studies were continued using the pulse program T1RCATSE.

The slower decaying component has an exponential time constant ($T_{1\rho}$) of 25 ms (±10 ms) which compares favourably to 21 ms from the previous experiment. Unfortunately, there is a drift to increasing times as the spin-lock increment is increased.

3.2.5 Results From T1RCATSE

Function	Population	Time (ms)
Exponential	266.3	30
Exponential	157.4	14
Exponential	140.6	3.9
Exponential	35.7	0.77

Table 3.4 Exponential components fitted to a concatenated $T_{1\rho}$.

GCAT1 represents the concatenated FID with three sets of dwell times (spin-lock time increments - 0.1 ms, 0.5 ms and 5 ms) used to examine the fast and slow decaying components more accurately. Notice it has been fitted to four exponential functions. Previous workers in this field of study have been able to correlate directly the number of exponential components of an FID to the number of physical components within a polymer - e.g. if three components then they were assigned to the rigid, mobile and interfacial regions. However, it is my belief that this is erroneous. It is just as feasible to fit an infinite number of exponential components to an FID. The criterion for my model using just four components has been the fact the next additional exponential modelled had a time constant of less than 0.01 ms - equivalent to the first point sampled in the FID.

A printout of the actual intensities of the individual points in the FID was then used to set up a sequence of T1RHOFIDSE experiments with the spin-lock time being determined by the analogous time of the FID concatenated point being sampled. This is

Spectrum 3.2 GCAT1 - Concatenated FID with Three Sets of Dwell Times.

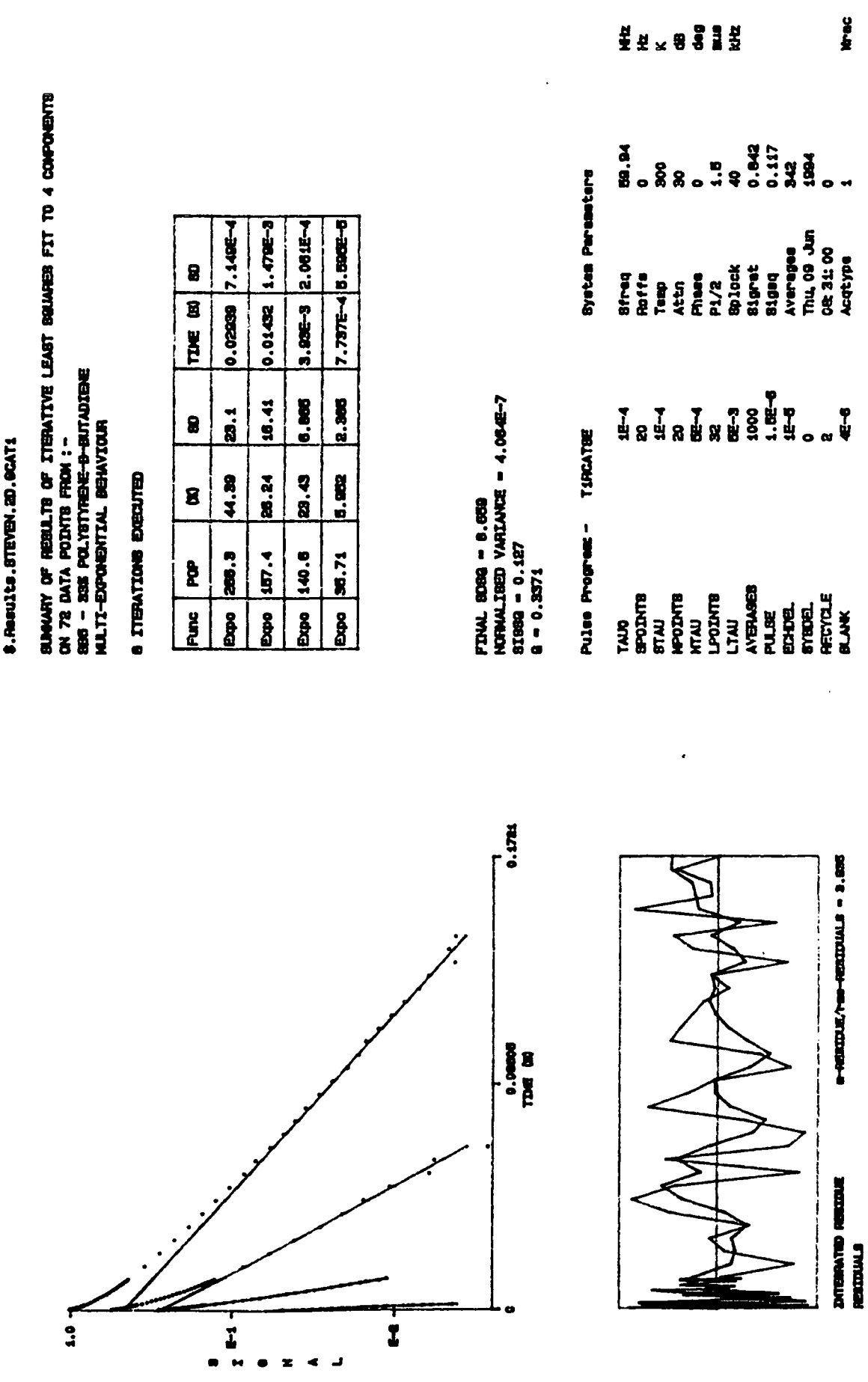

Table 3.5 T1RHOFIDSE Model Intensities Compared to Actual Intensities Obtained from GCAT1 (The Concatenated FID).

Spin lock time (ms)	GCAT1 Population	T1RHOFIDSE Total Population	Weib. Populations	Gaus. + Expo Populations
0.2	573.119	574.37	420.3	154.07
0.3	563.035	564.37	416.9	147.47
0.4	554.701	557.16	414.1	143.04
0.5	546.807	550.62	411.4	138.22
0.6	539.548	540.96	407.8	133.16
0.7	533.572	534.44	405.8	128.64
0.8	526.037	527.66	402.4	125.26
0.9	519.341	520.87	400.8	120.37
1	513.908	515.86	398	117.86
1.1	508.112	509.68	395.9	113.78
1.2	502.539	503.81	392.9	110.91
1.3	498.703	498.27	390.2	108.07
1.4	492.052	495.11	388.7	106.41
1.5	487.627	489.79	385.9	102.89
1.6	482.881	484.54	354.4	100.14
1.7	478.093	479.39	381.3	97.49
14.8	472.855	474.09	379.4	94.99
1.9	470.479	469.87	377	92.87
2	463.872	465.15	374.9	90.2
2.1	460.23	460.5	372.5	88.00
2.6	440.378	440.71	362	78.71
3.1	422.95	422.758	352.4	70.358
3.6	406.374	406.38	343.5	62.88
4.1	391.73	390.247	332.7	57.547
4.6	377.953	377.9	325.8	52.16
5.1	364.944	363.539	317.2	46.339
5.6	352.798	352.422	310	42.422
6.1	341.867	340.951	304.1	36.851
6.6	331.577	330.066	296.4	33.666
7.1	320.541	319.125	282.7	37.245
7.6	310.271	310.375	282.6	27.775
8.1	302.773	301.938	376.2	25.939
8.6	293.74	292.172	267	25.172
9.1	284.737	284.53	263.4	21.13
9.6	278.012	276.07	257.2	18.87
1.01	269.836	268.99	251.6	17.39
1.06	262.166	261.89	245.9	15.99
1.11	255.115	255.01	240.6	14.41
1.16	249.23	248.23	235	13.23
1.21	243.903	242.16	230	12.16
1.71	191.505	196.502	191.5	5.002
2.21	153.83	158.634	156.2	2.434
3.21	100.504	106.128	105.1	1.028
3.71	82.07	87.447	86.06	1.387

directly analogous to a two dimensional experiment but the second time dimension is being analysed by hand. Forty four of the seventy two points were analysed using T1RHOFIDSE and each one modelled accordingly to the previous model of Weibullian, Gaussian and exponential functions. A summary of the individual populations of these functions in comparison to the total populations obtained from the concatenated experiment is provided within Table 3.5. Of particular note is the comparison of the population of the sampled FID concatenated point to the total population of the T1RHOFIDSE experiment at the same time instant. The values are almost identical with no deviations or trends away from either total population. This indicates that the WRAC signal obtained from the probe is extremely consistent over a long period of time - this was one of the primary problems of this work since the lack of consistency prior to these results indicated potential and actual problems within the workings of the WRAC spectrometer.

Following this, the next step was to analyse the decay rates of the Weibullian and Gaussian+exponential components modelled from the T1RHOFIDSE experiments derived directly from the concatenated experiment. These two sets of data were analysed using the WRAC's Marquardt-Levenberg fitting method and compared to the modelling of the original concatenated FID populations. The different experiments modelling the decay rates of the modelled components were designated titles - GRAPH~T1R - for the populations of the original concatenated experiment, GWW1 - for the modelled Weibullian data and GGAUSEXW - for the modelled Gaussian+exponential data. The results of these analyses were as follows-

Spectrum 3.3 GRAPH~T1R - Model of The Concatenated Experimental Data at Different Spin-lock Times.

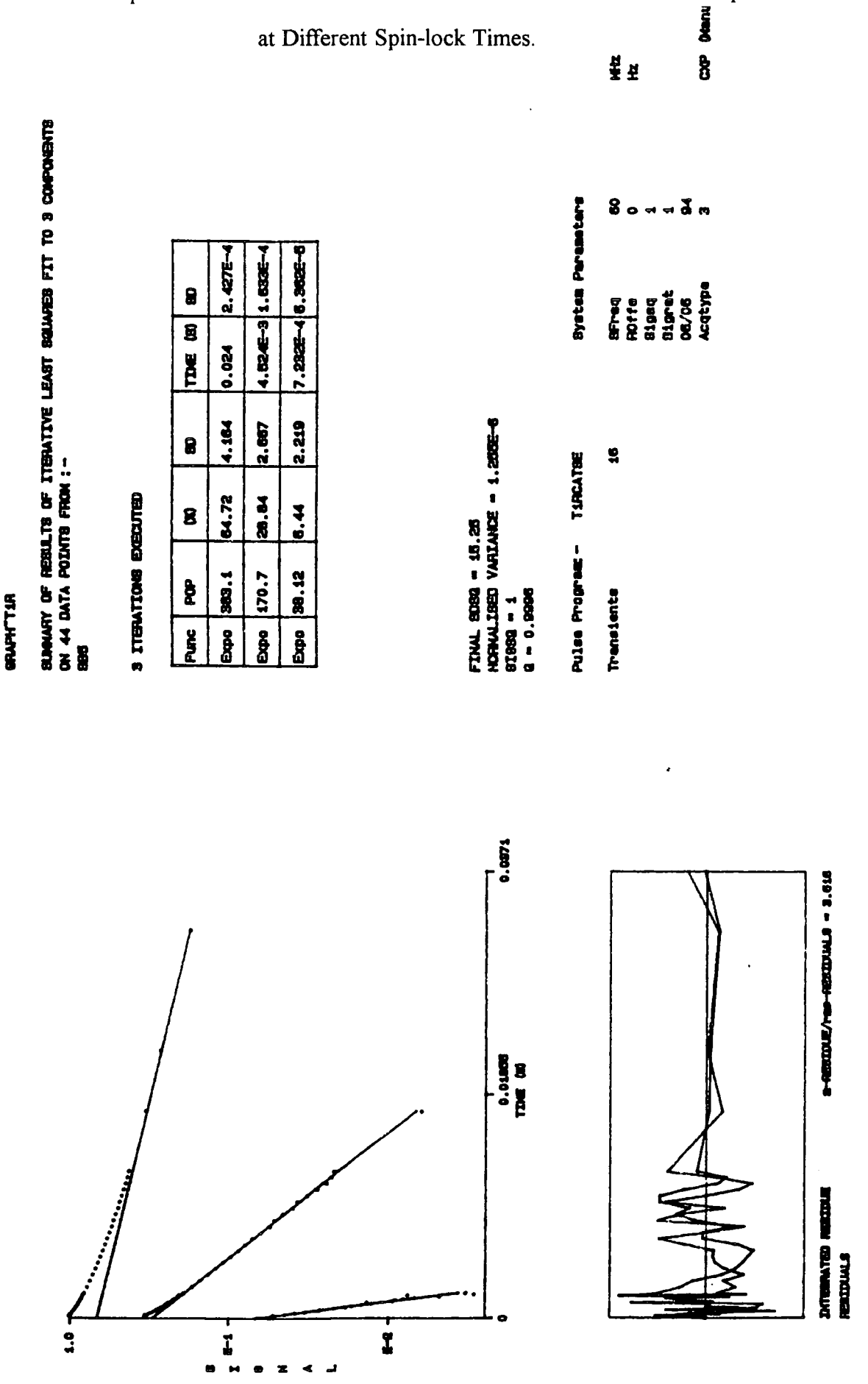

Spectrum 3.4 GWW1 - Model of The Weibullian Populations Determined From Concatenated Experiments at Different Spin-lock Times.

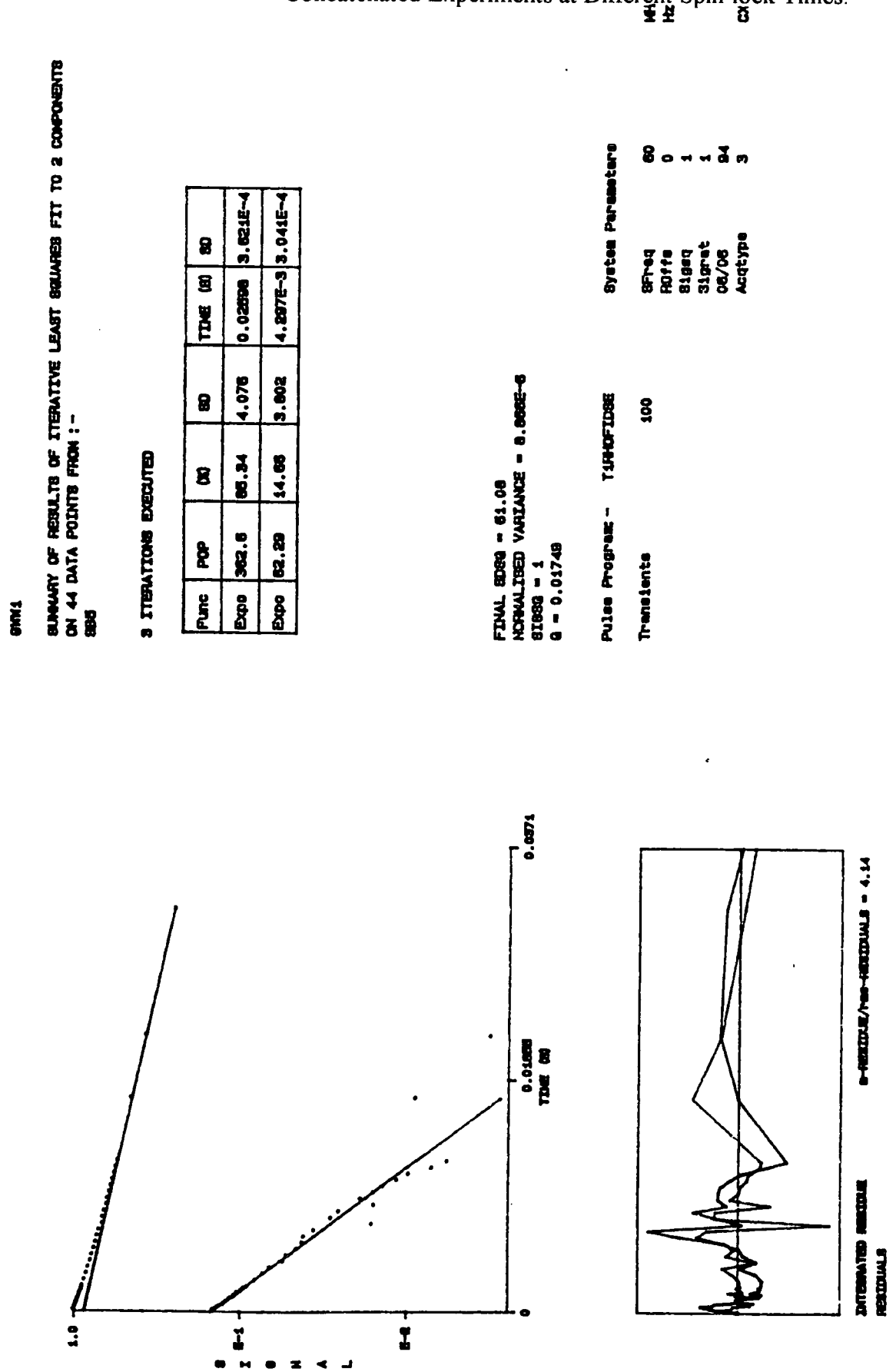

Spectrum 3.5 GGAUSEXW - Model of The Combined Gaussian + Exponential Populations Determined From Concatenated Experiments Using Different Spin-lock Times.

GGAUSEXW

SUMMARY OF RESULTS OF ITERATIVE LEAST SQUARES FIT TO 2 COMPONENTS
ON 44 DATA POINTS FROM :-
BBS

4 ITERATIONS EXECUTED

Func	POP	DX	SD	TIME (S)	SD
Expo	125.2	75.53	3.164	5.181E-3	1.088E-4
Expo	40.85	24.47	2.704	9.778E-4	1.027E-4

FINAL SUMS = 46.36
NORMALISED VARIANCE = 5.007E-6
SIGMA = 1
R = 0.2269

Pulse Program - TIMHOFIDBE

Transients 100

System Parameters

SFreq	60
RDffs	0
Sigsq	1
Sigrat	1
OS/OS	94
Acqtype	3

MHz
Hz
COP

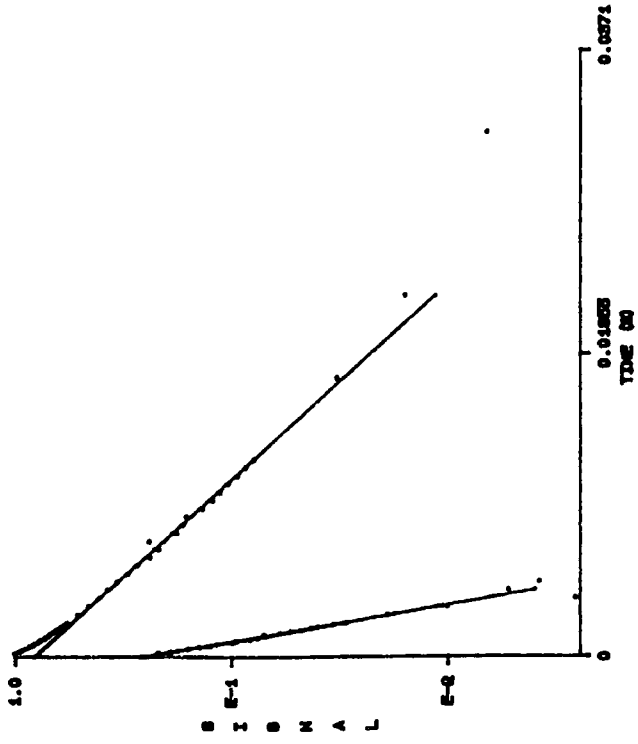

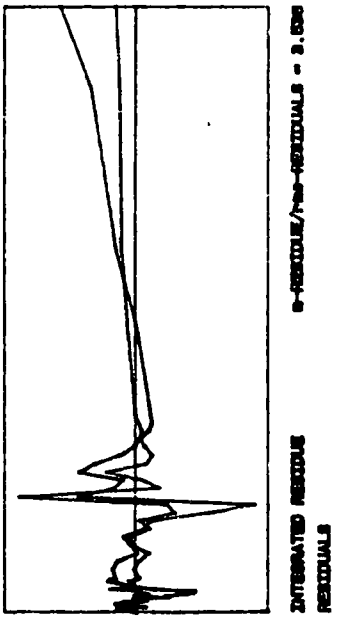

Function	Population	Time (ms)
Exponential	383	24
Exponential	171	4.5
Exponential	38	0.72

Table 3.6 The exponential components of the slow and fast decaying components in the experiment denoted GRAPH~T1R - a concatenated FID fit.

GGAUSEXW			GWW1		
Function	Population	Time (ms)	Function	Population	Time (ms)
Exponential	125	5.1	Exponential	363	26
Exponential	41	1.0	Exponential	62	4.3

Table 3.7 Separated exponential components fitted to the Weibullian and Gaussian+exponential statistics.

On comparison of the rate constants, the Weibullian exponentials fit to the 24 ms and 4.5 ms exponents of the total concatenated experiment. The rate constants of the Gaussian+exponential statistics fit to the 4.5 ms and 0.72 ms (slight difference in the very short time component but that is most likely down to the small number of points sampled or the accuracy of the WRAC trying to model fast decaying statistics).

These results reinforce the view that the mobile component is modelled to the Weibullian and the rigid component to the Gaussian+exponential statistics. They also highlight the overlap of the exponentials correlating to either not a clearly defined

interface (in terms of bulk magnetisations of the two block components) or the actual physical interface between the two components-

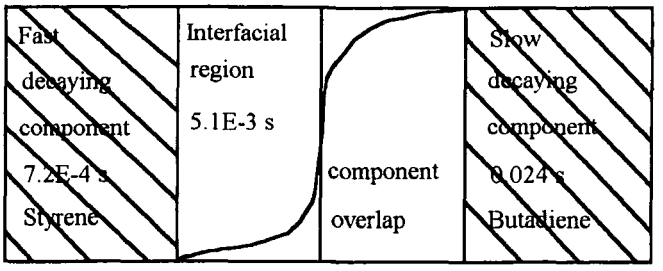

Fig. 3.8 Relaxation Profile Across The Diblock Copolymer Boundary.

The GGAUSEXW experiment shows a distinct deviation of m-residue/rms-residuals integrated residual - this could be an offset problem (chemical shift of the copolymer detected slightly different from the chemical shift of the reference material - butan-1,4-diol). Realistically, this is more due to an artefact of the use of modelling modelled data and just represents not a sufficient number of sampled points or noise. However, this does reflect in the more than marginal difference in the rate of decay from the exponential representing the so-called 'pure' styrene component - 0.98 ms compared to the concatenated result of 0.72 ms.

Next, the same concatenated experiment was completed with a delay between the 90° pulse and the acquisition of each data point. The delay - denoted sysdel - was 0.2 ms, and the experiment is called GCAT4. The results of the modelling were as follows-

Function	Population	Time (ms)
Exponential	289	28
Exponential	90	13
Exponential	12	2.4

Table 3.8 $T_{1\rho}$ Rates for a Concatenated Experiment with a System Delay.

Spectrum 3.6 GCAT4 - Concatenated $T_{1\rho}$ Experiment With a Delay Before Data Acquisition of 0.24 ms.

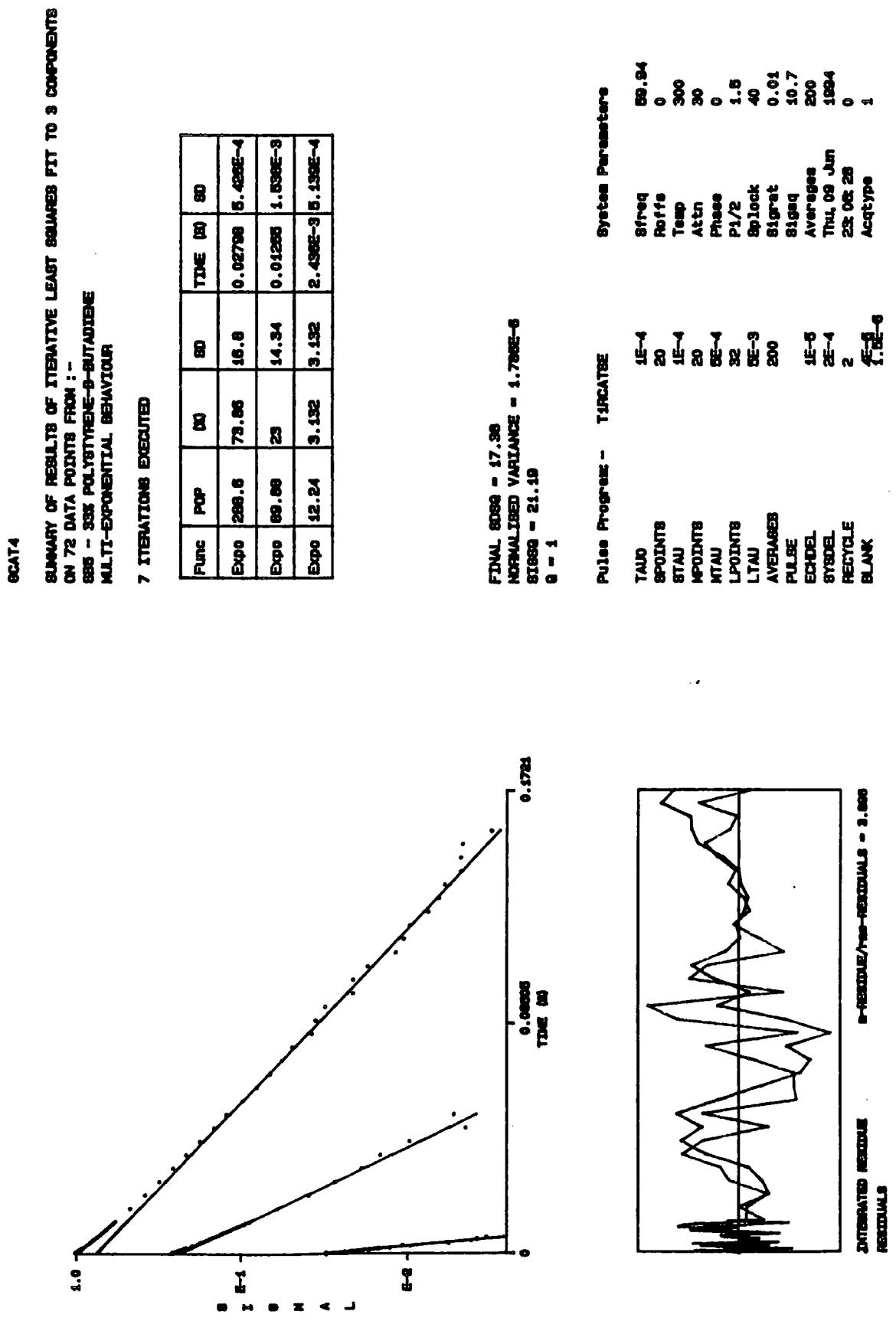

In comparison to the results of the exponential fitting of the original concatenated experiment (without the delay) it is clear that the three exponential components are directly observable within the original concatenated experiment. It shows that the use of only 44 points in GRAPH~T1R results in one of the components not being modelled - it has a time constant of 13 ms - thus proving that the modelling of the exponential components to physical attributes of the copolymer system is erroneous.

Two more concatenated runs were completed trying to examine the fast and slow decaying components more deeply. GCAT5 and GCAT6. They represent the concatenated experiments without and with the delay (0.2 ms) present. Notice that more points are sampled over a longer distance to determine that the FID does decay to zero over that period and that there are more sampling points within the respective different rates of decay regions.

3.2.6 Comparison Of Concatenated Experiments Without And With A System Delay

GCAT5			GCAT6		
Function	Population	Time (ms)	Function	Population	Time (ms)
Exponential	186	27	Exponential	178	26
Exponential	70	17	Exponential	64	13
Exponential	111	4.8	Exponential	11	2.9
Exponential	38	1	Exponential	-----	-----

Table 3.9 Concatenated experimental populations with three and four exponentials fitted.

These results reconfirm the previous results with the slowly decaying mobile component modelling to three exponentials and the total modelling to four exponentials. Again the time constants are very consistent. Overall, the model shows that the mobile

Spectrum 3.7 GCAT5 - Concatenated $T_{1\rho}$ Experiment Without a Delay Before Data Acquisition of 0.24 ms. A Four Exponential Fit.

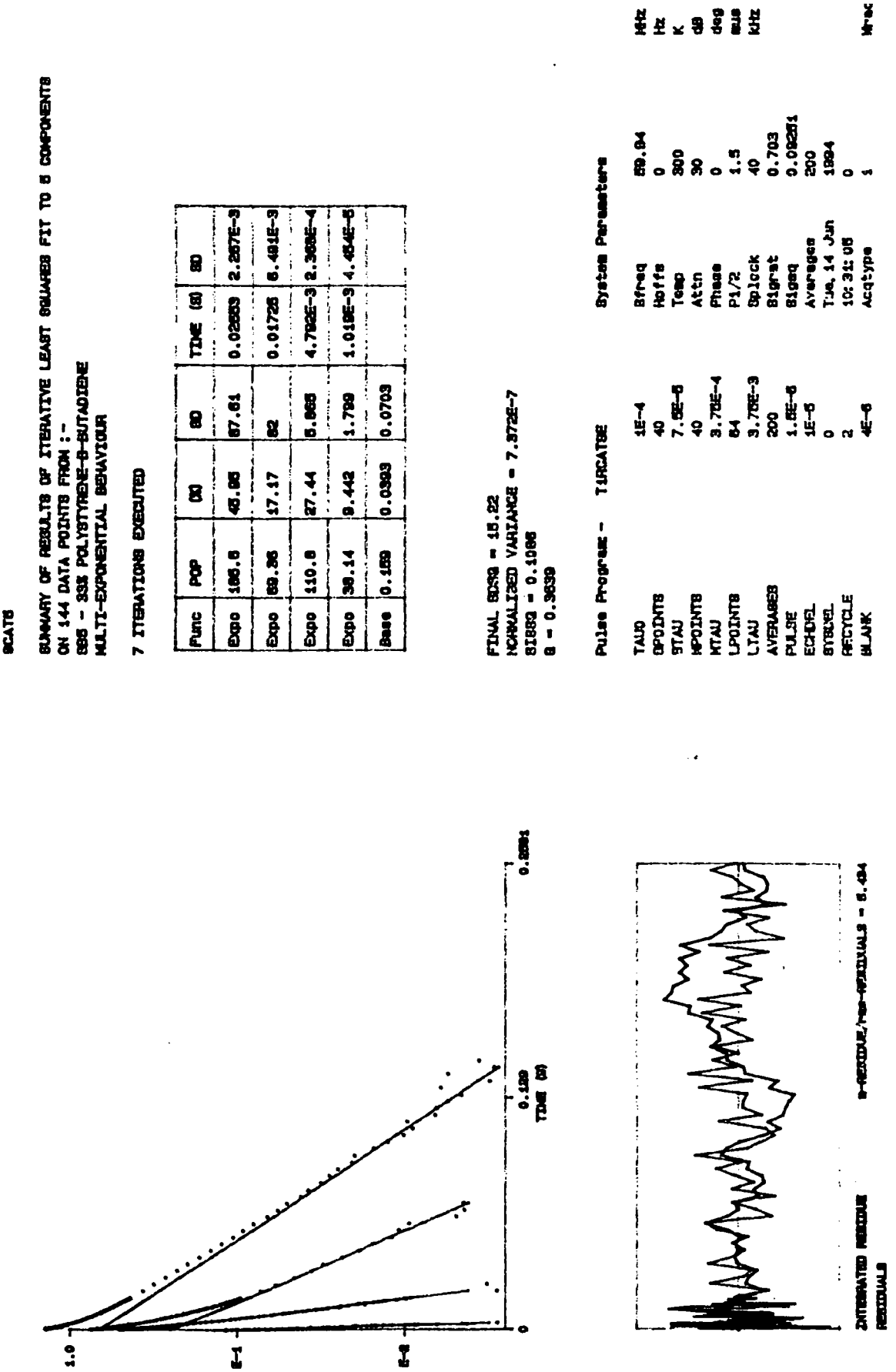

Spectrum 3.8 GCAT6 - Concatenated $T_{1\rho}$ Experiment With a Delay Before Data Acquisition of 0.24 ms. A Three Exponential Fit.

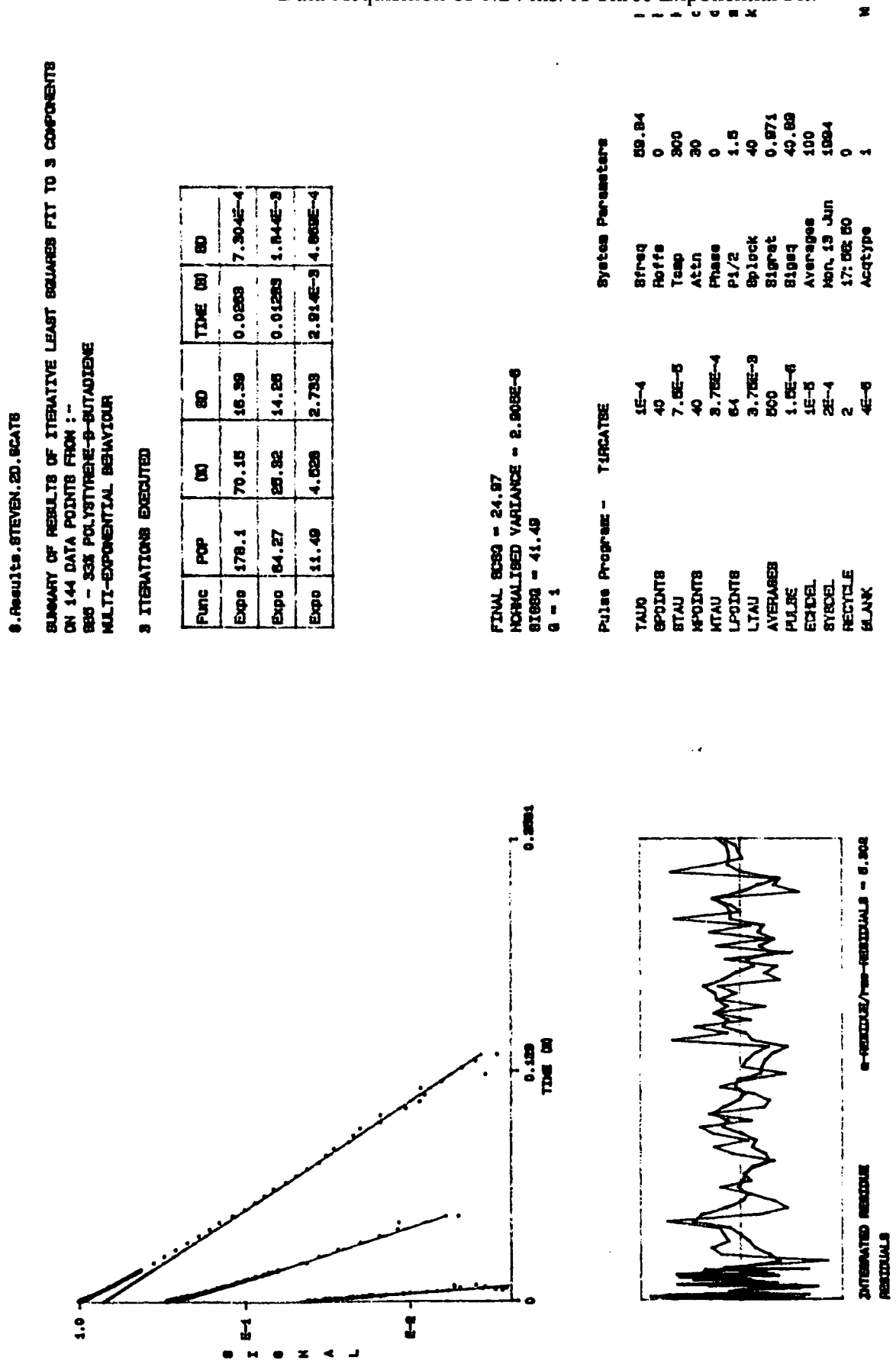

Weibullian is modelled sufficiently by three exponentials and the rigid - fast decaying component - models to two, with one of the exponentials modelling, to some degree, to both the Weibullian and the Gaussian+exponential component models.

One interpretation of these results can be gained from work of A. Kenwright et. al[7]. They studied annealed polypropylene to investigate relaxation of crystalline and amorphous boundaries. They investigated $T_{1\rho}$ behaviour and found four exponential fits, as in this investigation. They assumed the fastest relaxation rate could be attributed to the intrinsic relaxation time of the amorphous material (analogous to the polystyrene 'pure' region). They investigated the intermediate relaxation rates and determined that one was a result of establishment of a 'Fick' diffusion profile (the second fastest relaxation rate) and the other was associated with the rate at which the diffusion profile moves back into the slower relaxing region (the crystalline region). They suggested that the slowest relaxing region follows the establishment of a diffusion profile across the entire sample.

However, they do postulate that since the fastest relaxing region undergoes rapid spin-diffusion (i.e., its relaxation is helped by the presence of the slower relaxing component) then upon comparison of the relaxation rates for the purely crystalline and partially crystalline materials, results in the purely crystalline material having a slower relaxation rate. This may be observed later in the results of the homopolymers' relaxation behaviour (Section 3.2.8).

Finally, these two sets of data were used to try and achieve absolute values of styrene and butadiene FID components. Since the GCAT6 models the Weibullian only, then if this was extrapolated back to a zero sysdel (0.2 ms was the system delay used in GCAT6) then the difference in populations of the GCAT6 FID points to the GCAT5 FID points would result in the determination of the rigid component FID population.

Referring back to the T1RHOFIDSE which had an spin-lock time of 0.2 ms, the Weibullian function for that delay is given by -

$$\exp-\left(\frac{2E-4}{8.88E-4}\right)^{1.43} = 0.888$$

This factor represents the fraction of the signal that is present at time 0.2 ms compared to time t = 0. Using this as a multiplier the absolute values of the Weibullian were obtained and thus the Gaussian+exponential component values. A plot of these absolute values of decay of the FID components shows that the initial intensity of the signals is in a ratio of 2:1 (Weibullian:Gaussian+exponential) which correlates exactly to the percentage composition of the copolymer components - 67:33 w/w % polybutadiene:polystyrene. This again reinforces the modelling procedure and the reproducibility of the results from the WRAC.

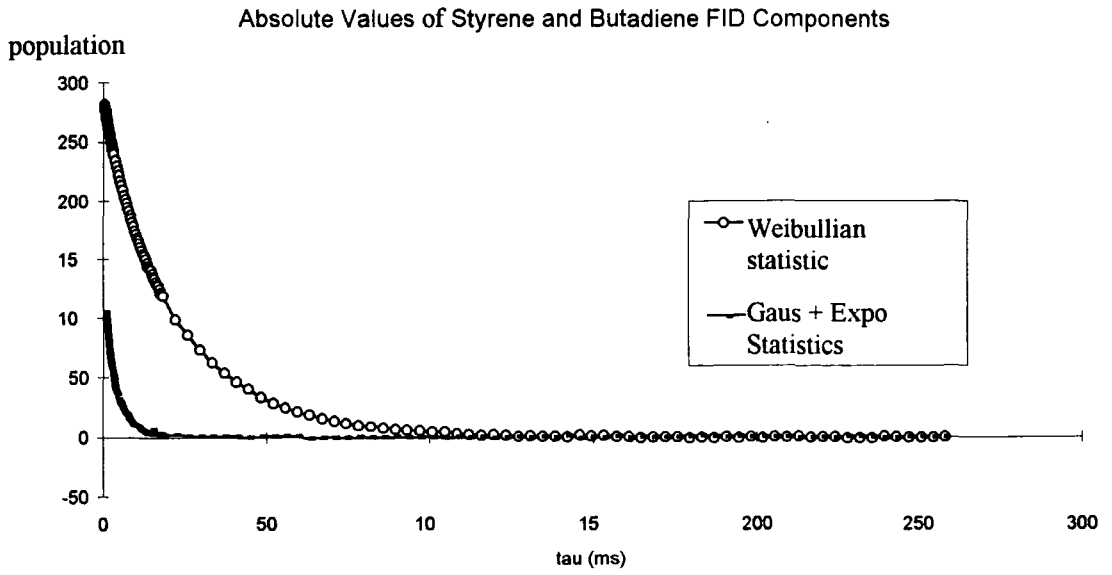

Graph 3.4 Extrapolated Data Indicating The Absolute Decay of Styrene and Butadiene FID Components.

3.2.7 Summary of Relaxation Results For SB5 - Polybutadiene-b-polystyrene Copolymer

Initial measurement of T_1 and $T_{1\rho}$ gave values of 186 ms and 24 ms/4.8 ms, respectively. The ratio of the $T_{1\rho}$ values was 66%:34% with the larger percentage referring to the longer (24 ms) relaxation time, hence indicating some success in differentiating between the two moieties within the copolymer.

Results from the effect of echo delay on the FID components (Section 3.2.2) revealed that the three individual statistical functions best fitted the FID-

A Weibullian - the long time decaying component - with a percentage population of 67%.

A Gaussian and exponential component which together combined to give a percentage population of 33% - clearly modelling the faster decaying component.

The effect of spin-lock time on the statistical functions (Section 3.2.3) indicated that the Weibullian function modelled to the slow decaying component with a T_2 relaxation rate of 940 μs (±30 μs) and the combined Gaussian + exponential functions had T_2 relaxation rates of 23 μs (±2 μs) and 16μs (±1 μs), respectively. This gave an overall description of the FID in terms of the equation-

$$\frac{dM}{dt} = M_w \exp(-t/9.4E-4)^{1.5} + M_g \exp(-t/1.6E-5)^2 + M_e \exp(-t/2.3E-5)$$

The rate of decay of the three modelled components was also analysed and gave values of $T_{1\rho}$ of-

Weibullian $T_{1\rho}$ = 21 ms Exponential $T_{1\rho}$ = 5.5 ms Gaussian $T_{1\rho}$ = 1.3 ms

Due to the large range in relaxation rates an investigation was made into the duration of the spin-lock time increment and its effect on $T_{1\rho}$ components (Section 3.2.4). It was found that three individual values of $T_{1\rho}$ were detected depending on the spin-lock time increment. Subsequently, a concatenated FID was detected and modelled using four exponentials (the best fit) to investigate the T_2 behaviour (Section 3.2.5).

The problem of evaluating $T_{1\rho}$ in-depth was investigated with the rate of decay of the modelled functions at each dwell time of the concatentated experiment. This, in a sense, was a two-dimensional experiment. The three statistics each modelled to three $T_{1\rho}$ values overall, but the fourth value of 13 ms was missing which may have been due to the loss of modelled data towards long dwell times.

It was noted that during longer dwell times only the Weibullian model fitted with any degree of sucess suggesting that the faster decaying components were not present. This gave an excellent way of modelling the intrinsic behaviour of the Weibullian with the use of a concatenated experiment with a system delay before acquisition (GCAT4 - Spectum 3.6). Using a system delay of 0.2 ms allowed three $T_{1\rho}$ values to be modelled which may relate to the polybutadiene component and some fraction of the interface.

GCAT5 and GCAT6 were the finale of this work. They were identical concatenated experiments without and with a system delay. These two experiments were used to try and investigate the intrinsic relaxation behaviour of the fast and slow decay components present within the copolymer FID. The fast decaying component (present in GCAT5) was found to be described by 3 exponential functions and the slower decaying function modelled to two exponentials. Two of the exponential functions overlapped suggesting some degree of modelling of the interface.

The next logical step was to try and analyse the homopolymers and compare their relaxation characteristics to the two extreme relaxation rates modelled in the copolymer and investigate any degree of correlation.

3.2.8 Relaxation of the Homopolymers

From the preceding results of spin-locked relaxation times for diblock copolymers it was decided to analyse the homopolymers and also to examine the effect of evacuating the samples to see if there was any change in T_1 and $T_{1\rho}$ relaxation times. This was essential for the later study of polymer annealing since the samples have to be evacuated due to the air sensitivity of the diene moiety when under elevated temperature conditions. The homopolymers' physical characteristics are as follows-

POLYBUTADIENE - a homopolymer of polybutadiene with a molecular weight of 37000 which was anionically polymerised. Due to the viscous nature of the homopolymer it had to be solvent cast into the glass WRAC tube using THF (tetrahydrofuran) as the casting solvent. This was removed by evacuation.

POLYSTYRENE - a homopolymer of polystyrene with a molecular weight of 54000 which was the precursor in the anionic polymerisation of the diblock copolymer SB4. This was analysed in its crumb form (prior to annealing) both in standard atmosphere and under evacuated conditions.

The results are as follows-

Sample Description	T_1/s	$T_{1\rho}$/ms
Polystyrene (crumb form)	1.3	3.2
Polystyrene evacuated (crumb form)	7.6	3.0
Polybutadiene - THF solvated ?	1.95/54%;0.45/40%	0.098/18%;0.64/82%

Table 3.10 Relaxation times of homopolymers under evacuated and atmospheric conditions

Two points of interest are particularly important-

1 The effect of evacuating the homopolymer of polystyrene results in a dramatic increase in the value of T_1, due to the removal of paramagnetic oxygen which helps relax the aromatic protons within the polystyrene ring[8]. This increase by a factor of five has been observed by other workers. Notice that $T_{1\rho}$ is barely affected by evacuation, which is advantageous since $T_{1\rho}$ will be the relaxation time indicative of any changes upon annealing. If the assignment was correct in the investigation of the copolymer SB5 then the relaxation time for the polystyrene moiety has increased from 0.74 ms, in the copolymer, to 3.2 ms, in the homopolymer. This does suggest that the slower relaxing polybutadiene component does cause the polystyrene to relax more rapidly in the copolymer.

2 The transferral of polybutadiene into an NMR tube using THF and after evacuation still results in THF being trapped within the polymer matrix. This is evident from the two components for both T_1 and $T_{1\rho}$. However, the populations are not consistent between the two relaxation times T_1 and $T_{1\rho}$, so the WRAC, during this experiment, was giving relaxation parameters that were very inaccurate. It was hoped that the $T_{1\rho}$ for the polybutadiene homopolymer would show a greater value compared to its analog in the copolymer suggesting that the more rapidly relaxing polystyrene was acting as a relaxation sink.

3.2.9 Effect of Annealing on $T_{1\rho}$ Values

The last investigation was to try and observe any effects in the spin-locked relaxation time upon annealing. The annealed copolymer sample was evacuated but the unannealed sample was run under atmospheric conditions. The annealed sample was SB5 - annealed at 150°C for 168 hours. The results (analysed as the sum of four exponentials) were as follows-

Sample	Expo	Time/s	Expo	Time/s	Expo	Time/s	Expo	Time/s
GCAT5	46%	0.026	17%	0.017	27.4%	4.8E-3	9.4%	1E-3
GCAT1E	45.6%	0.024	20.6%	0.014	24%	4.1E-3	9.7%	8.3E-3

Table 3.11 Effect of annealing on $T_{1\rho}$ values for the gyroid polymer - SB5 - 33% polystyrene-b-67% polybutadiene.

One can see that there is no observable difference between the annealed (GCAT1E) and unannealed (GCAT5) experiments. This is not surprising since it has already been mentioned previously that the only difference is in the interface which is not directly modelled to any particular $T_{1\rho}$ relaxation time. The sample would have undergone phase separation but $T_{1\rho}$ is not an indicator of the degree of phase separation. The only way to investigate phase separation is by spin diffusion, which is described more fully using the Goldman-Shen experiment in the next chapter.

3.3 References

1 Harris R. K., Kenwright A. M., Royston A., Say B. J., 'A Versatile NMR Spectrometer for Observing Abundant Spins in Condensed Phases', *Meas. Sci. Technol.*, 1980, Vol. **1**, P1304.

2 Caceci M. S., Cacheris W. P., 'Fitting Curves to Data- The Simplex Alogrithm is the Answer', *BYTE*, 1984, P340.

3 Press W. H., Flannery B. P., Teukolsky S. A., Vetterling W. T., 'Numerical Recipes - The Art of Scientific Computing', 1986, Pub. Cambridge: Cambridge University Press, P523.

4 Kaufman S., Bunger D. J., 'Use of the Weibull Function for Describing the Shape of the Free Induction Decay', *J. of Mag. Res.*, 1970, Vol. **3**, P218.

5 Powles J. G., Strange J. G., 'Zero Time Resolution Nuclear Magnetic Resonance Transients in Solids', *Proc. Phys. Soc.*, 1963, Vol. **82**, P6.

7 Kenwright A. M., Packer K. J. and Say B. J., 'Numerical Simulations of the Effects of Spin-Diffusion on NMR Spin-Lattice Relaxation in Semicrystalline Polymers', *J. Mag. Res.*, 1986, Vol. **69**, P426.

8 Froix M. F., Williams D. J. and Goedde A. O., 'NMR Relaxation Time Studies of Polystyrene', *Macromolecules*, 1975, Vol. **98**, P354.

4.1 Goldman-Shen Experiments

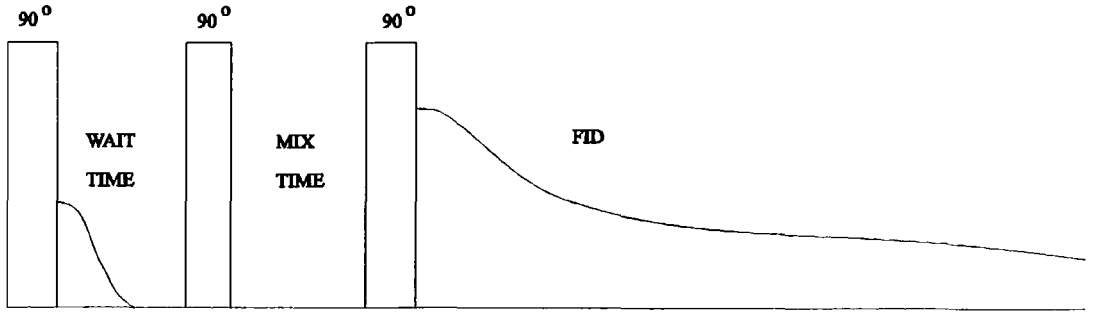

Figure 4.1 Standard Goldman-Shen pulse sequence.

The Goldman-Shen experiment[1] is the classic experiment used to study spin-diffusion. Referring to the above diagram it mainly consists of three pulses each separated by a delay. The first 90° pulse nutates the magnetisation into the transverse xy-plane. The subsequent delay, denoted 'WAIT' - causes relaxation under T_2 conditions. Thus, when the sample under investigation consists of a heterogeneous system with mobile and rigid regions then these regions decay under fast and slow relaxing rates. This first delay can be tailored to cause relaxation of the faster decaying component down to a zero signal. This results in an attenuated slowly decaying signal. When the next 90° nutating pulse is applied it causes the resulting magnetisation to be nutated into the positive or negative z-axis - depending on the phase of the applied 90° pulse. The subsequent delay is denoted 'MIX' which allows spin-diffusion to occur between the two differently decaying regions. However, since the magnetisation is in the ±z-direction then longitudinal relaxation occurs (T_1 relaxation) which competes with the process of spin-diffusion. The subsequent third and final 90° nutating pulse brings the magnetisation back into the transverse plane where the signal can be detected and a measure of spin-diffusion can be obtained. Unfortunately, there are certain problems inherent within the sequence-

1 The use of three successive pulses without the allowance of relaxation to equilibrium between each pulse results in the creation and detection of multiple quantum coherences. The use of a single 90° nutating pulse on a spin-system results in the creation of single quantum coherences (in terms of the density matrix description of the bulk magnetisation this results in first-order populations occurring in the diagonalised density matrix). Now the delay after the first pulse, if long enough to allow recovery back to the system's equilibrium populations, results in the transfer of single quantum coherences which are easily detected. However, when the magnetisation is nutated under non-equilibrium conditions, i.e. the magnetisation has not relaxed back to its equilibrium state between each pulse, then this causes the creation of multiple quantum coherences, i.e. in spin density matrix terms the matrix consequently contains first, second and higher order terms. These transitions, unfortunately, become coherent upon placing the magnetisation back into the xy-detection plane after the third 90° nutating pulse.

Evidence for these multiple quantum coherences came from studies of hexamethylbenzene with phase selection for zero-quantum coherences. These results will be described in detail in the results section of this chapter.

2 Off-resonance effects, resulting from different chemical shifts of proton species present within the sample, create errors in the nutation angle for particular proton species within the bulk magnetisation.

A series of experiments was completed to try and investigate some of the factors involved in the Goldman-Shen sequence.

4.2 Experiments and Their Results

4.2.1 Nutation Angle Effects

The original idea was first used to try and investigate if any T_1 effects were evident. The two initial sequences investigated implemented the storage of the bulk magnetisation in the positive and negative z-directions. The first point of the FID was detected and the results were analysed to see if T_1 effects were on a similar time-scale to the effects of spin-diffusion.

Unfortunately, there were too many experimental variables to consider when using the original experiment, so initially the two experiments implemented were the 3-pulse Goldman-Shen experiments, with positive and negative storage, but without the two delays between the pulses. This resulted in a ±270° and ±90° nutation angles when using the three-pulse sequences with differing phases. The pulse program required defining the phase of each pulse as 0 and 2. This represents the nutation of the magnetisation from the positive z-direction into the 90_x and 90_{-x} respectively. This sequence of +/- x-direction pulses resulted in 8 different experiments.

Pulse sequence	Nutation angle	SB5	Butan-1,4-diol	Reduced size[#]
G000	+270	-475	-1084	-515
G002	+90	+553	+1225	+595
G020	+90	+544	+1218	+596
G022	-90	-573	-1200	-612
G200	+90	+550	+1241	+616
G202	-90	-583	+1205	-592
G220	-90	-575	+1205	-595
G222	-270	+486	+1097	+522

Table 4.1 Effect of nutation angle on the absolute population detected in the Goldman-Shen sequence.

[#] These results are from a sample of reduced sample size placed within the centre of the magnet.

The reference material which was used to compare effects of each nutation angle was butan-1,4-diol and the first point of the resultant FID was detected so the final absolute signal amplitudes were as seen in Table 4.1.

These results show that there is a marked difference in the population detected as the magnetisation is nutated through different angles through phase-space. The results from the reduced sample size runs were used to investigate B_1 field inhomogeneities. It can be seen that the dramatic reduction in detected population for the pulse sequences G000 and G222 still occur in these runs hence showing that this population reduction is not an effect resulting from B_1 field inhomogeneities.

The next step was to check the accuracy of the nutation angle since the biggest errors in the previous experiment came from the G000 and G222 sequences where the magnetisation is nutated by +/-270° angle, respectively. Using butan-1,4-diol the first point in the FID was detected as a function of the pulse duration (a 90° nutation angle is equal to 1.5 μs) and the results were-

Pulse duration-(μs) - G000	Population	Pulse duration (μs)- G222	Population
1.4	-883	1.4	+917
1.5	-896	1.5	+958
1.6	-820	1.6	+889

Table 4.2 Effect of pulse duration on the population detected with butan-1,4-diol.

The pulse duration has a marked effect on the population detected. With both pulse sequences the maximum population (90° nutation angle) is at 1.5 μs which shows that there are few errors from the nutation angle. The populations observed for the two pulse sequences at 1.5 μs should have been equal but clearly they are not. This discrepancy may be due to spectrometer instability but is more probably due to the

inability to set the nutation angle in units less than 0.1 μs. These conclusions lead to the use of the solid-echo within the sequence.

4.2.2 The Solid-echo Pulse[2]

The solid-echo pulse, which has already been described in Chapter 3, is used to refocus the magnetisation to zero-time resolution without the occurrence of receiver breakthrough. However, this also helps in reducing the effects of off-resonance contributions to the bulk magnetisation. When the bulk magnetisation is nutated by 90° into the xy-plane there are certain components within the magnetisation which nutate by greater and lesser angles compared to the 90° nutation angle. When using three nutating pulses of the same phase this causes these nutation angle errors to be increased three-fold.

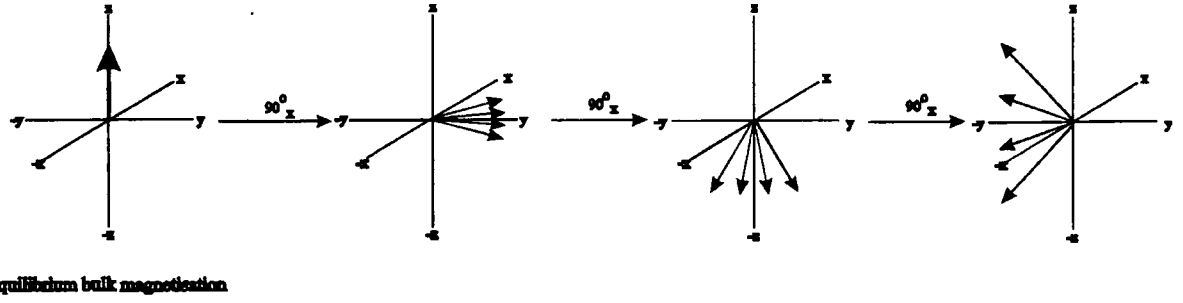

Equilibrium bulk magnetisation

Figure 4.2 The effect of three nutating angles of the same phase on the off-resonance components of the bulk magnetisation.

This is why there are discrepancies in the detected populations for G000 and G222. The solid-echo pulse causes the incorrectly nutated parts of the magnetisation to rotate by 90° from the longitudinal axis into the transverse xy-plane. This can be understood more easily in the following diagram where the nutation angle effects have been exaggerated-

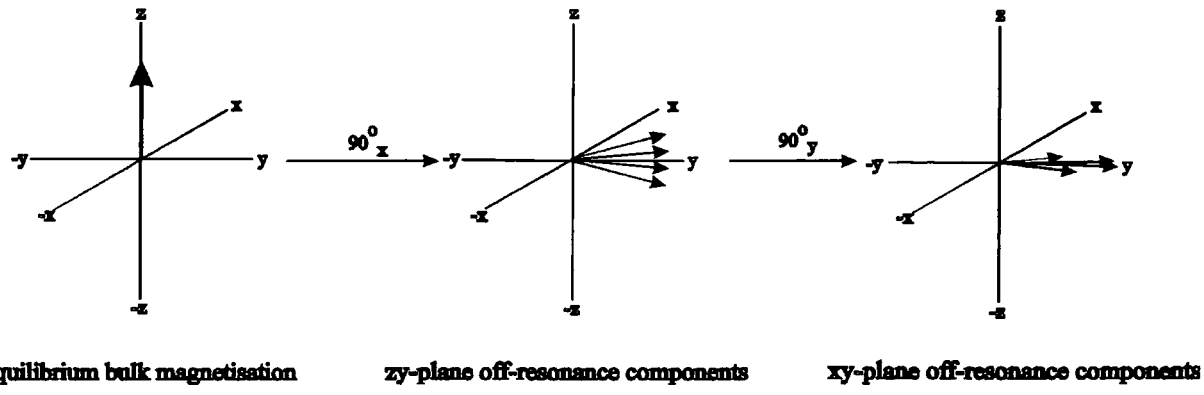

Figure 4.3 The effect of the solid-echo pulse on the off-resonance components of the bulk magnetisation.

This resulted in the investigation of the positive and negative storage of the magnetisation in the Goldman-Shen sequence with the implementation of the solid-echo pulse to try and investigate T_1 effects.

4.2.3 Multiple quantum Coherences[3-12]

It has been highlighted previously that the use of three successive pulses on a spin ensemble that is not under equilibrium conditions results in the formation of multiple quantum coherences[13]. In density matrix terms and product operator terminology this can be described most succinctly.

Coherence is a transition between a pair of eigenstates |r> and |s> with a difference in quantum numbers of M_r and M_s. The transverse magnetisation has a coherence related to a change in the quantum number $p = \pm 1$. Coherence is the superposition of two eigenstates[13]-

$$\psi_{rs} = a_r|r\rangle + a_s|s\rangle \qquad \text{Eqn. 4.1}$$

Coherence is expressed by the existence of nonzero density matrix elements $\sigma_{rs} = |r><s|$ and $\sigma_{sr} = |s><r|$. The terms of the density operator are the sum of the density matrices each with a coherence order - p, i.e.-

$$\sigma(t) = \sum_{p} \sigma^{p}(t) \qquad \text{Eqn. 4.2}$$

The properties of the coherence of order p can be demonstrated by transformations under rotation about the z-axis-

$$\exp(-i\phi F_z)\sigma^{p} \exp(i\phi F_z) = \sigma^{p} \exp(-ip\phi) \qquad \text{Eqn. 4.3}$$

Where $F_z = \sum_{k=1}^{N} I_{kz}$ for N spins. This coherence can also be represented by a coherence transfer map-

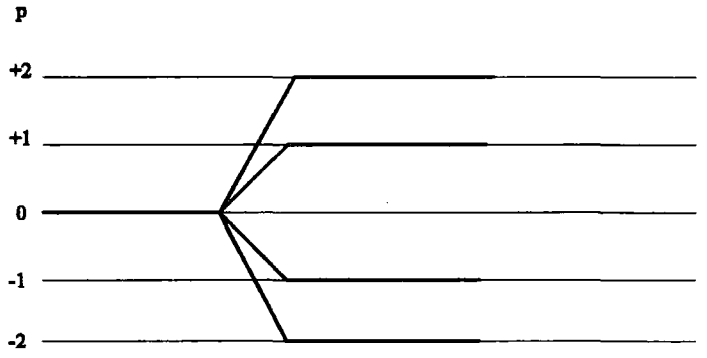

Figure 4.5 Multiple quantum coherence map for a single 90° pulse. Only ±1 transitions are formally observed.

The route that is highlighted is called the coherence-transfer pathway. Thermal equilibrium is characterised by p = 0 and should end as p = ±1 (a single-quantum coherence) to be detectable or in terms of a coupled I = ½ spin pair the resultant coherences that are possible are-

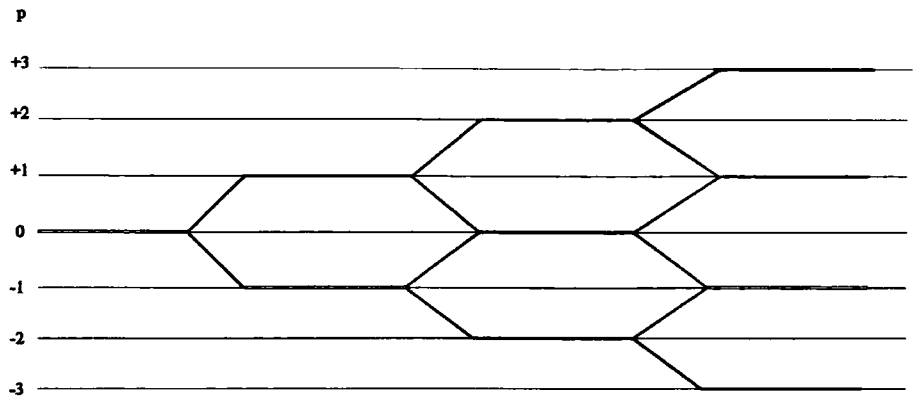

Figure 4.6 Quantum coherence map for a spin I = ½ spin system and three pulses. Single-quantum coherences are shown

4.2.4 Selection of Coherence-transfer Pathways[8]

Consider a complete pulse sequence with n-coherence-transfer processes expressed by the propagators (pulses) U_1, U_2,..., U_n:-

$$\sigma_0 \xrightarrow{U_1} \xrightarrow{U_2} \cdots \xrightarrow{U_n} \sigma(t) \qquad \text{Eqn. 4.4}$$

Each propagator transfers one coherence $\sigma^p(t_i^-)$ into numerous different orders $\sigma^{p'}(t_i^+)$ or:-

$$U_i \sigma^p(t_i^-) U_i^{-1} = \sum_{p'} \sigma^{p'}(t_i^+) \qquad \text{Eqn. 4.5}$$

where σ^p and $\sigma^{p'}$ are density operators before and after the transformation by U_i. Thus the changes resulting from n consecutive coherence-transfer steps are described by a set of n values-

$$\Delta p_i = p'(t_i^+) - p(t_i^-) \qquad \text{Eqn. 4.6}$$

The state of the spin-system initially is at thermal equilibrium so p = 0, and for final detection of a coherence (or coherences) then p = -1. Therefore, the sum of all the coherence pathways is described as-

$$\sum_i \Delta p_i = -1 \qquad \text{Eqn. 4.7}$$

This selection of coherence pathways is achieved by introducing a phase increment into the phase cycle of the sequence employed. In density matrix form this takes on the appearance of a phase-shifted propagator $U_i(\phi_i)$, which converts equation 4.5 into-

$$\sigma^p(t_i^-) \xrightarrow{U_i(\phi_i)} \sum_{p'} \sigma^{p'}(t_i^+) \exp\{-i\Delta p_i \phi_i\} \qquad \text{Eqn. 4.8}$$

Thus, this is achieved by performing N_i experiments where the rf phase ϕ_i of the propagator is incremented systematically to obtain a particular change, Δp_i, in coherence order-

$$\phi_i = k_i 2\pi / N \qquad \text{Where } k_i = 0, 1, \ldots, N_i\text{-}1 \qquad \text{Eqn. 4.9}$$

However, an important aspect of this sequence of N_i experiments is that a series of values of Δp_i are selected, i.e. $\Delta p_i \pm nN_i$ with n = 0, 1, 2, ... With the Goldman-Shen sequence the use of three 90° pulses results in the following coherences formed with just a two-spin system:-

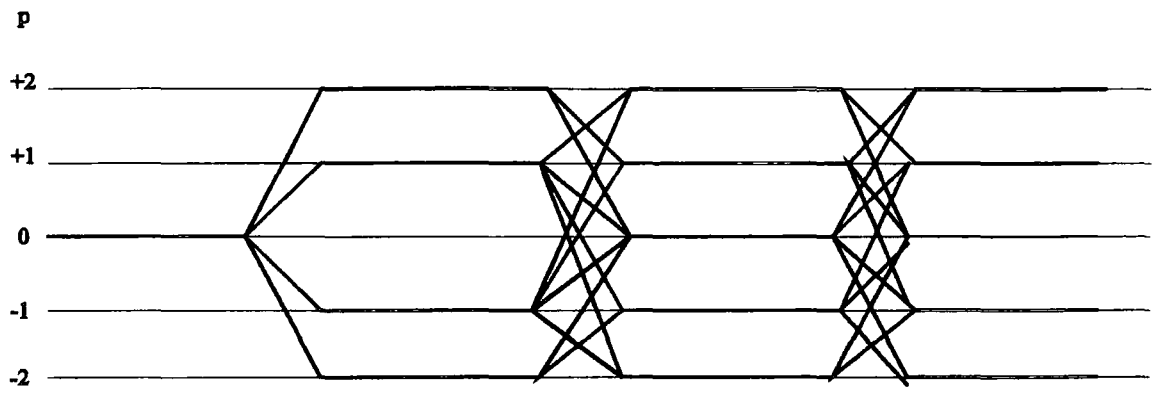

Figure 4.7 Coherence-transfer map of single- and double-quantum coherences

Thus, Δp_i ranges from -3, -2, -1, 0, 1, 2, 3. The coherence -1 needs to be detected and the coherences labelled 0, 1and 2 have to be blocked or in the terminology used by Bodenhausen et. al.: -3, -2, **-1**, (0), (1), (2), 3. This requires a minimum of four N_i experiments with a phase increment of ϕ_i = 0, p/2, p and $3\pi/2$. Thus, the phase-cycling needed for single-quantum selection for a single pulse is-

f_1	f_{rec}
0	0
90	90
180	180
270	270

Table 4.3 Phase-cycling of one pulse to detect a single-quantum transition

Notice that the phase of the receiver (f_{rec}) cycles with the phase of the pulse. This is called CYCLOPS (CYClically Ordered Phase Sequence). However, this becomes more complicated when using more than one nutating pulse. The phase increment of the receiver is determined by the equation-

$$\phi_{rec} = -\Delta p_1\phi_1 - \Delta p_2\phi_2 - \Delta p_3\phi_3 \qquad \text{Eqn. 4.10}$$

This is for the three-pulse Goldman-Shen sequence. Thus, the selection of the single quantum transition in this sequence is shown by the following coherence transfer map (Figure 4.8)-

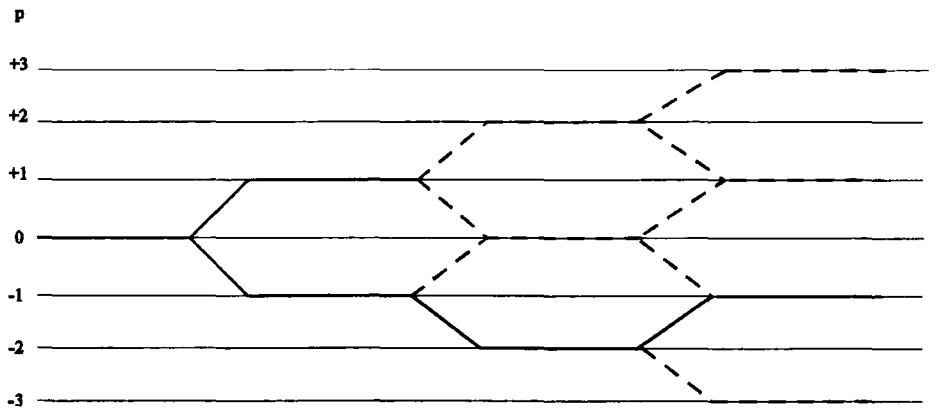

Figure 4.8 Coherence pathway for detection of selection-quantum coherences in the Goldman-Shen experiment

Here the dotted lines represent the coherences that are phase-cycled destructively. The single-quantum transition is selected when $\Delta p = -1$. This sequence of events is achieved by the following pulse sequence (Table 4.4)-

f_1	f_2	f_3	f_{rec}
0	180	0	180
0	180	180	0
90	270	0	0
90	270	180	180
180	0	0	180
180	0	180	0
270	90	0	0
270	90	180	180

Table 4.4 Phase-cycling for single-quantum selection in the Goldman-Shen sequence.

As a comparison a series of ten experiments was devised using hexamethylbenzene, and the resultant transformed spectra were analysed to see the effect of phase-cycling, positive- and negative-storage of the magnetisation in the mixing time and the effect of the solid-echo pulse on the selection of coherences in the Goldman-Shen sequence. Thus, the following list of experiments were completed and the corresponding spectra are given -

1 A single-pulse experiment used as a reference since it only has single-quantum coherences.

2 A single-pulse experiment with a solid-echo pulse incorporated before detection in order to be used in reference with any subsequent spectra utilising the solid-echo pulse sequence.

3 The Goldman-Shen sequence storing the magnetisation in the positive z-direction. The sequence used incorporates the solid-echo pulse but has no phase-cycling, so not detecting solely single-quantum coherences.

4 The Goldman-Shen sequence storing the magnetisation in the positive z-direction. No solid-echo pulse has been used and no phase-cycling. Thus, this is the basic Goldman-Shen sequence.

5 The Goldman-Shen sequence storing the magnetisation in the positive z-direction with phase-cycling that selectively destroys the single-quantum coherences but maintains the zero-quantum coherence transition (the dipolar flip-flop interaction with the Zeeman levels).

6 The Goldman-Shen sequence storing the magnetisation in the positive z-axis whilst using a sold-echo pulse and no alternation of the phase of the receiver. This results in the magnetisation being nutated into the positive x-axis continually throughout the experiment, so removing any effects that may arise from storing the magnetisation in the -z-axis.

7 The Goldman-Shen sequence storing the magnetisation in the positive z-axis, with a solid-echo pulse but with no mixing time. This results in a two-pulse

experiment with the second pulse being a composite of two 90° pulses of opposite phase. This is used to try and investigate if any distortions occur during the mixing time.

8 The Goldman-Shen sequence storing the magnetisation in the positive z-axis, again with no mixing time but without a solid-echo pulse.

9 The Goldman-Shen sequence storing the magnetisation in the positive z-axis and phase-cycled to select the single-quantum coherence without the effects of a solid-echo pulse.

10 The final Goldman-Shen sequence consists of storing the magnetisation in the negative z-axis but with no mixing time. This is essentially used to investigate any effects of storing the magnetisation in the negative z-axis.

Analysis of Spectra 4.1 and Spectra 4.2 results in the following conclusions-

Experiment 1 The single-pulse experiment shows that no distortion of the hexamethylbenzene peak occurs upon the application of a single 90° nutating pulse.

Experiment 2 The use of a solid-echo pulse also has no deleterious effects on the transformed spectrum.

Experiment 3 Of particular note is the spectrum of the Goldman-Shen sequence utilising a solid-echo sequence. It shows that the distortion (as seen in experiment 4) resulting from single-quantum coherences is removed, i.e. the solid-echo pulse selectively refocuses the single-quantum coherence of the overall three-pulse sequence. However, there do seem to be higher orders of quantum coherences that are not refocused, resulting in a baseline distortion on either side of the detected resonance.

Experiment 4 Referring to the Goldman-Shen sequence not incorporating the solid-echo pulse results in the distinct distortion resulting from multiple quantum coherences.

Spectra 4.1 Five Transformed Goldman-Shen Experiments.

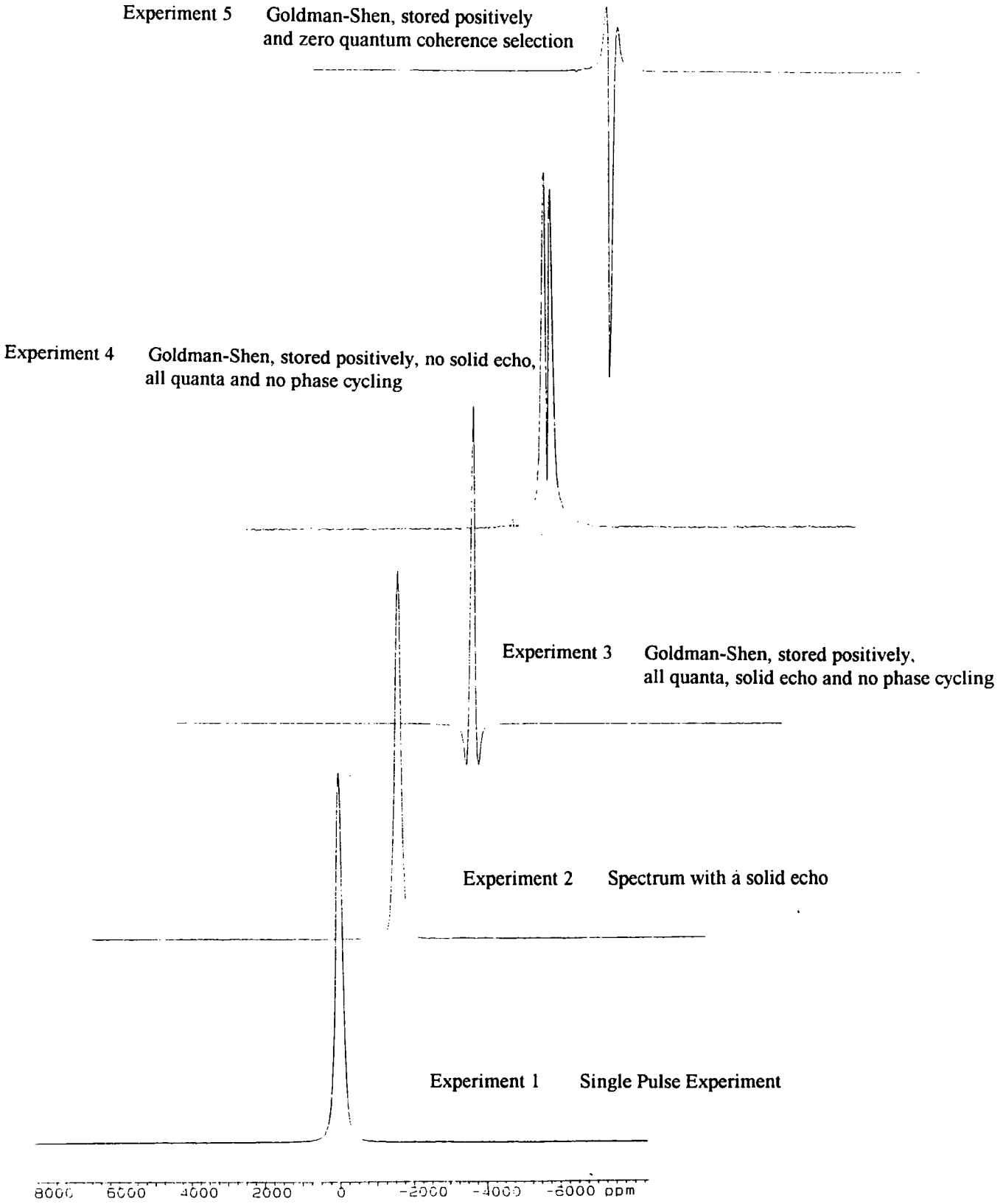

* All peak heights are in absolute intensity mode

Spectra 4.2 Five Transformed Goldman-Shen Experiments.

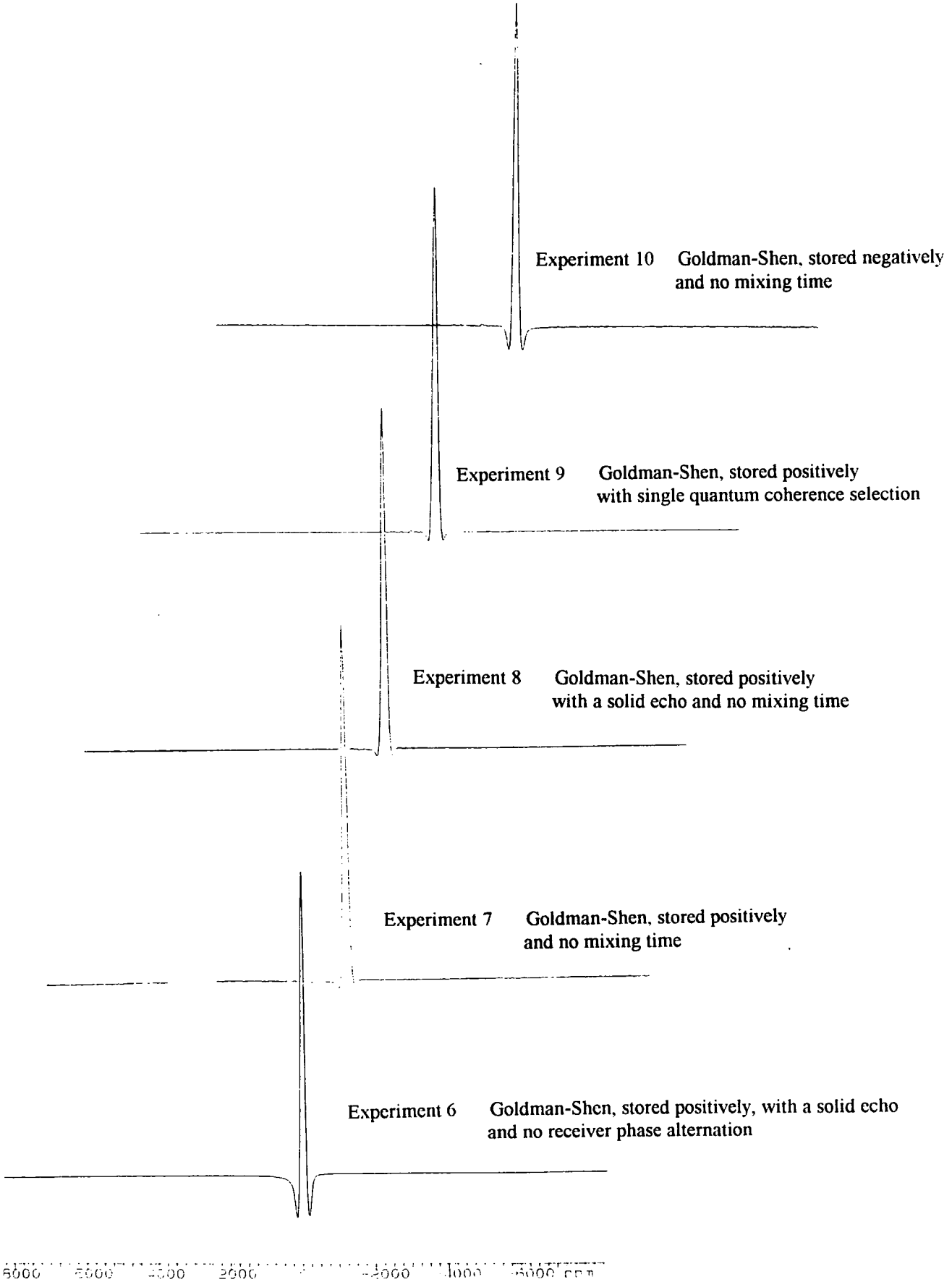

* All peak heights are in absolute intensity mode

Experiment 5 The Goldman-Shen sequence selecting the zero-quantum coherence with no solid-echo pulse does indeed show a greater distortion of the hexamethylbenzene from the Gaussian lineshape. The phase-cycling sequence was the same as that sequence used to select single-quantum coherences only this time the receiver phase was incremented further by 180° each time it was applied in order to subtract alternate signals and so result in the selection of the zero-quantum coherence[13].

Experiment 6 The sequence incorporating the solid-echo pulse but with no phase alternation of the detection receiver phase again shows a baseline distortion arising from refocusing only the single-quantum coherence. This particularly shows that there is no distortion arising directly from detecting the magnetisation in the negative x-axis since the receiver phase was not altered, hence causing the magnetisation to be detected in the positive and negative x-axes..

Experiment 7 The spectrum resulting from storing the magnetisation in the positive z-axis but without a mixing time does indeed show that the distortion from multiple quantum coherences does indeed becomes detectable from the result of using three successive nutating pulses, i.e. the multiple quantum coherence is generated by the use of a second pulse (but not directly detectable at this stage as is seen with no mixing time). However, subsequent evolution results in the distortion being detected by the use of a third pulse.

Experiment 8 Use of a solid-echo pulse but with no mixing time again results in no multiple quantum distortion but there is still some small baseline distortion which seems to be unresolvable even with phase cycling, as is seen in the next spectrum which selects only single-quantum coherences.

Experiment 9 This incorporates the phase-cycling sequence in order to select the single-quantum coherence. It is just as successful as the solid-echo pulse in terms of

destroying the multiple quantum coherences but there is still a small inherent distortion of the baseline.

Experiment 10 This has no mixing time (hence no transference of the distortion into the detectable frame) and stores the magnetisation in the negative z-axis. There is considerably more distortion compared to the analogous experiment storing the magnetisation in the positive z-axis. However, this may be a result from using three pulses of the same phase which only enhances off-resonance nutation angle effects.

The result of these experiments was to recommend the incorporation of both the phase-cycling procedure to select the single-quantum coherences and the use of the solid-echo pulse to reduce B_1 field inhomogeneities and thus to prevent carrier signal distortion as well as the selection of single-quantum coherences.

4.2.5 T_1 Effects[14]

The first sequence devised was denoted - GSHENSE - a Goldman-Shen experiment using a three-pulse sequence with a solid-echo to create phase coherence of the signal which avoids receiver breakthrough-

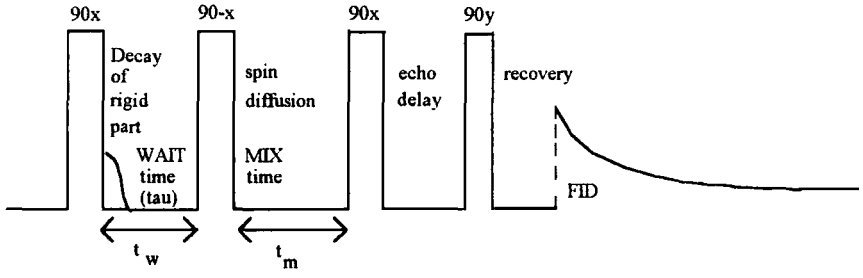

Figure 4.4 Goldman-Shen pulse sequence with a solid-echo pulse - denoted GSHENSE.

The magnetisation is nutated by a 90° pulse into the y-axis, then there is a delay for a time - tau - so that the rapidly decaying component decays to zero intensity (at a time $t_w=T_1\ln 2$) before the application of another 90° pulse of opposite phase to bring the magnetisation back into the +z-axis. A time -denoted MIX or t_m - is used to allow spin-diffusion to occur from the slower decaying component to the faster decaying component before application of a final 90° pulse to translate the resultant magnetisation into the detection axis, whereupon a 90° solid-echo pulse is used before acquiring the data. The results were denoted GGOLD1

GSHENMSE - this is exactly the same as the previous sequence except there is no 'MIX' time for the allowance of spin-diffusion. Effectively, this is an FID of the slowly decaying component. This is used to determine whether the fast decaying component has decayed completely. The resultant FID contains only the long-decaying mobile component which, if the relaxation parameters are known, can be extrapolated to its initial magnitude of magnetisation and thus can be used to calculate the absolute

magnitude and decay of the slowly decaying component independent of the faster rigid component. The FID can then be analysed into components to determine the extent of spin-diffusion occurring. This may seem identical to a standard single-pulse experiment with a solid-echo but there may be some effect from the successive use of a $90°_{-x}$ followed by a $90°_{x}$ within the pulse sequence on the resultant FID detected which simulates more accurately the 3-pulse Goldman-Shen experiment. The results were denoted GGOLD2

GSHENGSE - this also is the same as the Goldman-Shen sequence except that the magnetisation is stored in the negative z-axis (by use of a $90°_{+x}$ as the second pulse) before being translated into the detection axis (by a $90°_{-x}$ as the third pulse). This is used in comparison with the GSHENSE FID to try to eliminate or investigate the T_1 effects that occur in conjunction with spin-diffusion processes. The results were denoted GGOLD3

To try and remove multiple quantum transitions the three above Goldman-Shen programs were also rewritten incorporating phase cycling into the sequences. These sequences were denoted GSHENSECYC (storing the magnetisation in the positive z-direction using phase-cycling and a solid-echo pulse - results called GCYC1), GSHENMSECYC (same as GSHENSECYC but with no mixing time - results called GCYC2), GSHENGSECYC (storing the magnetisation in the negative z-direction but phase-cycled and incorporating a solid-echo pulse - results called GCYC3) and GSEPMSECYC (same as GSENMSECYC but with the magnetisation stored in the positive z-direction - results called GCYC4).

The results of these Goldman-Shen experiments have been summarised in the following table which show the first detected point in each FID acquired as absolute populations-

Spectrum 4.3 GGOLD1 - Goldman-Shen Experiment With a Solid-echo Pulse.

Spectrum 4.4 GGOLD2 - Goldman-Shen Experiment With a Solid-echo Pulse and No Mixing Time.

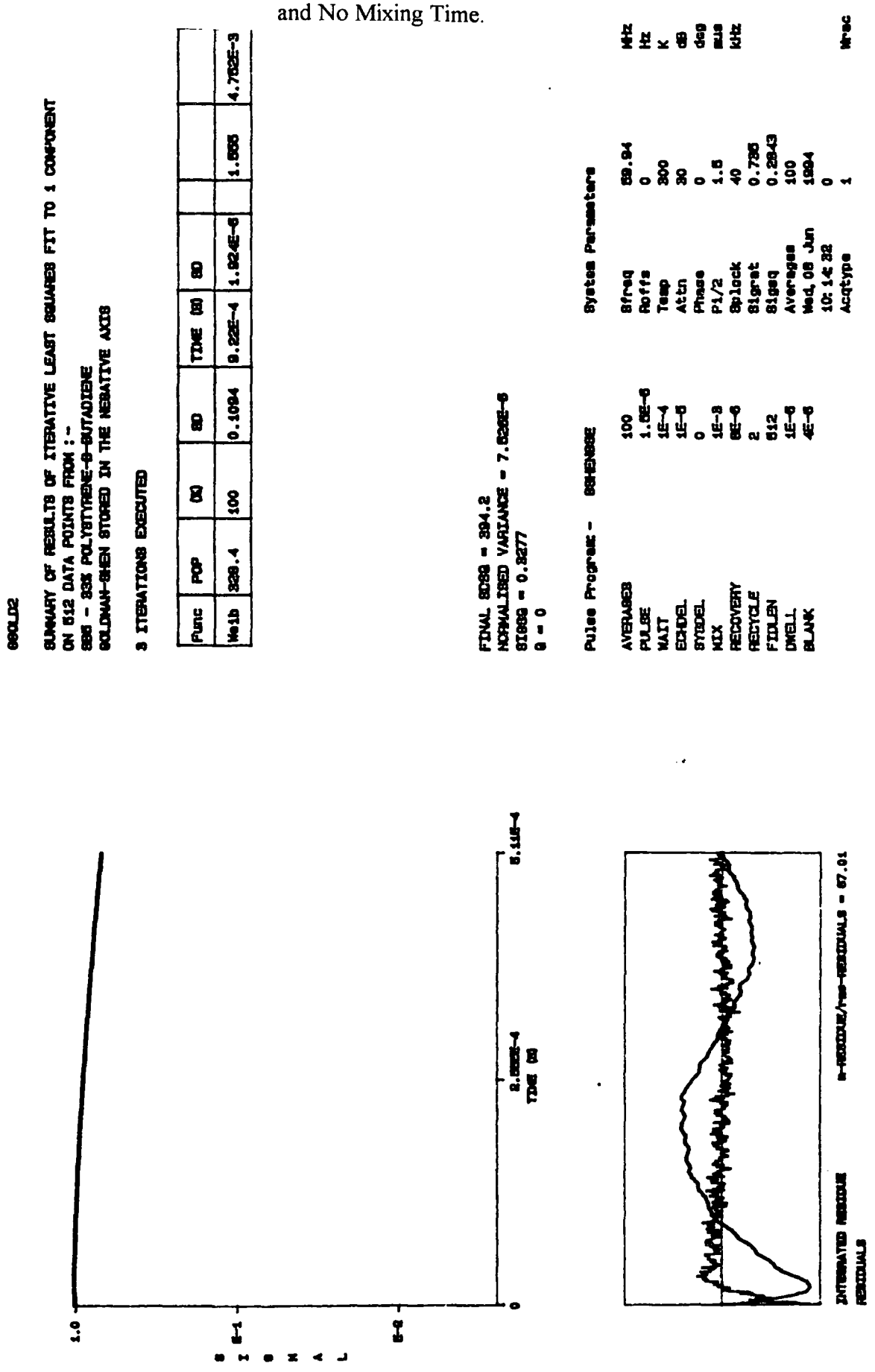

Spectrum 4.5 GGOLD3 - Goldman-Shen Experiment With a Solid-echo Pulse and the Magnetisation Stored in the Negative z-axis.

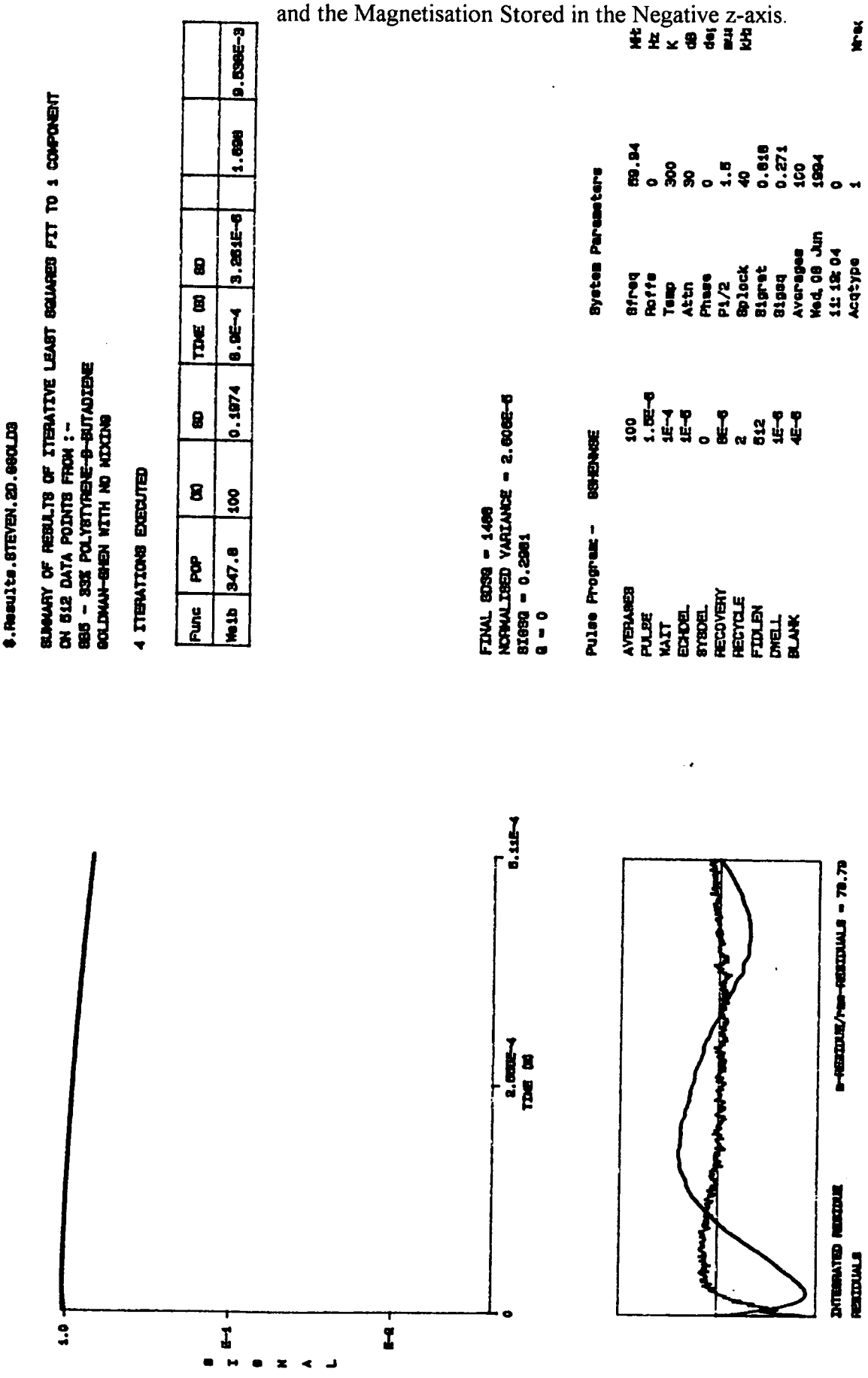

Spectrum 4.6 GCYC1 - Phase Cycled Goldman-Shen Experiment, With a Solid-echo Pulse.

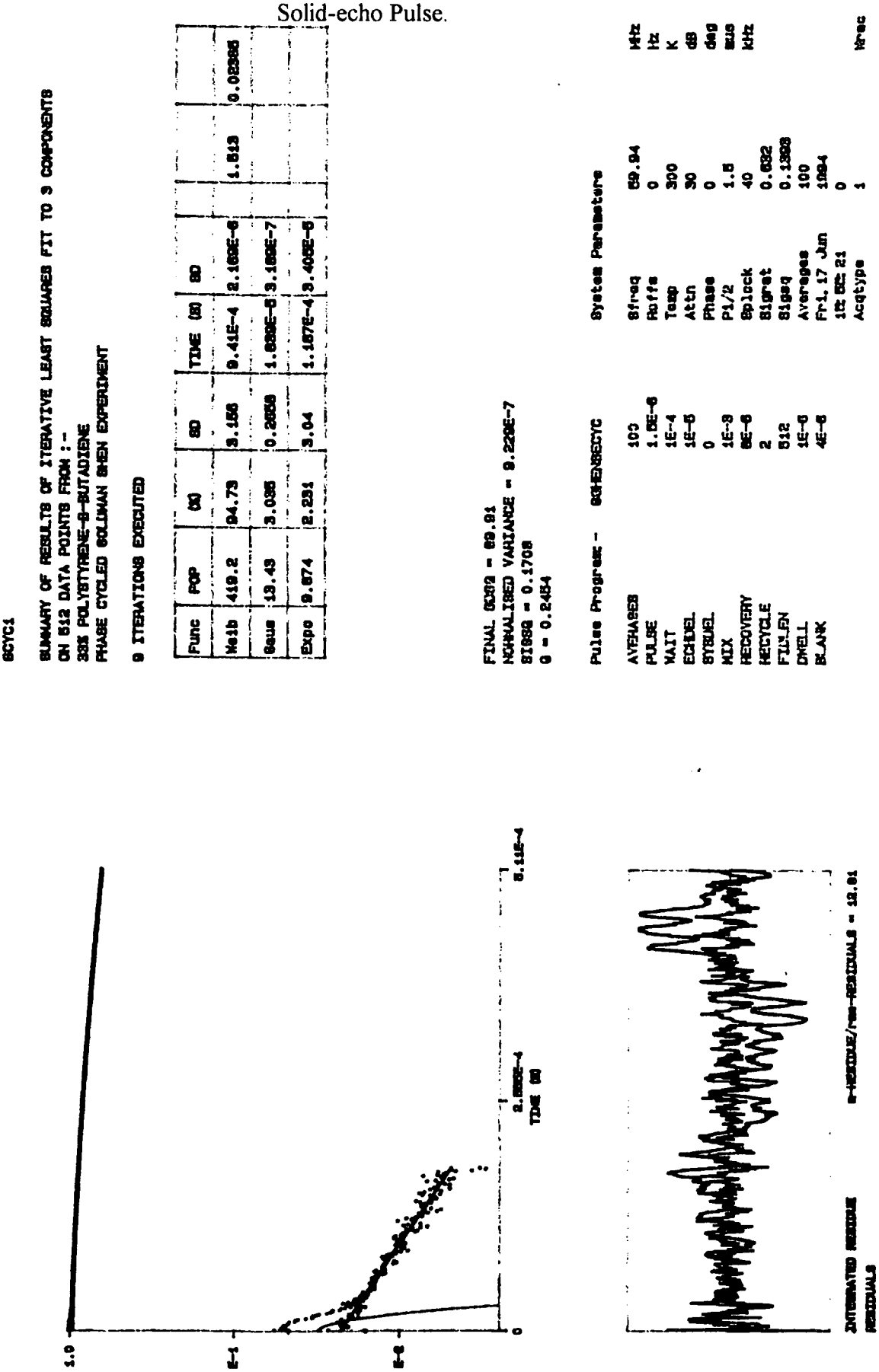

Spectrum 4.7 GCYC2 - Phase Cycled Goldman-Shen Experiment With a Solid-echo Pulse and No Mixing Time.

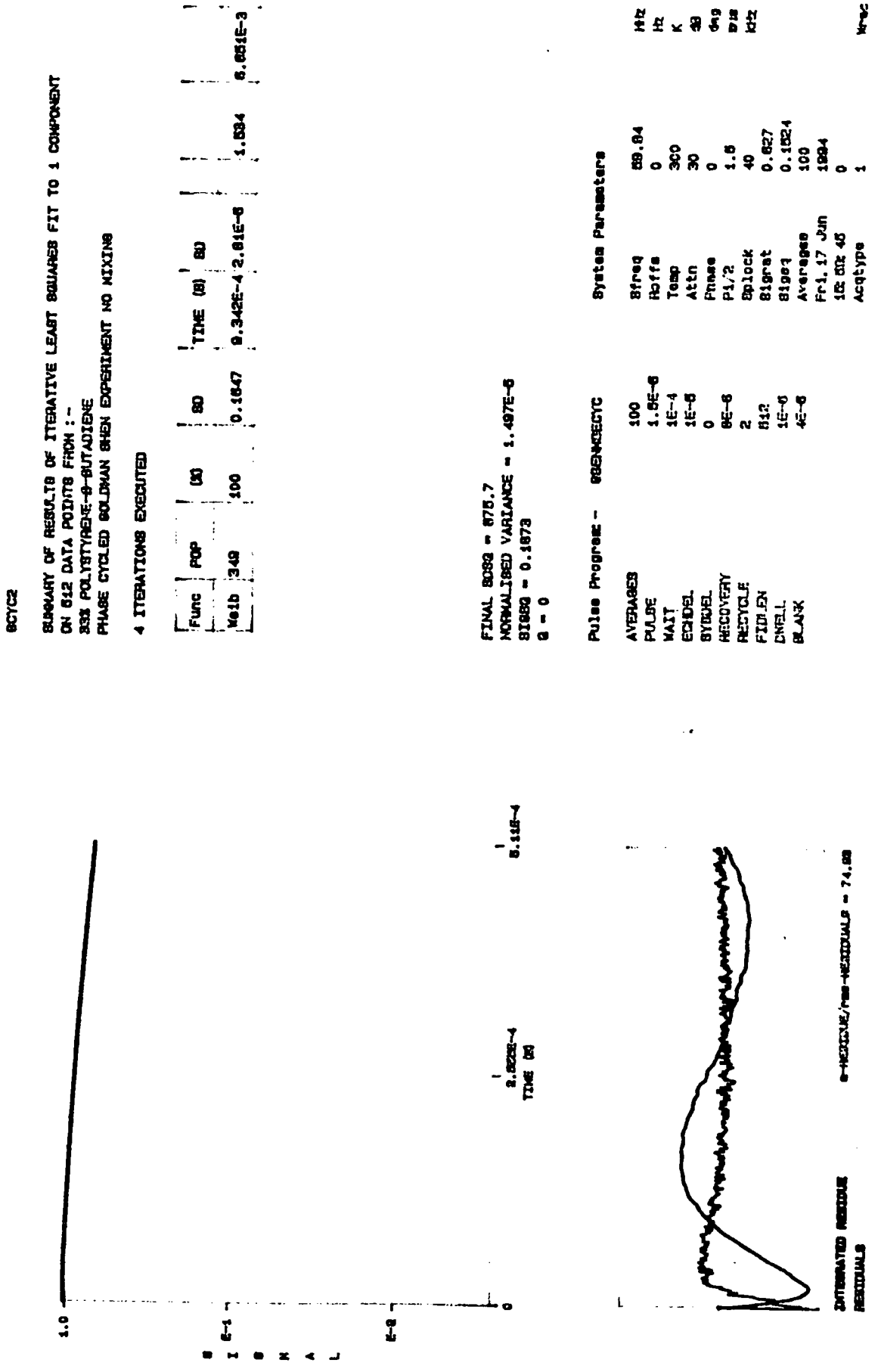

Spectrum 4.8 GCYC3 - Phase Cycled Goldman-Shen Experiment With a Solid-echo Pulse and the Magnetisation Stored in the Negative z-axis.

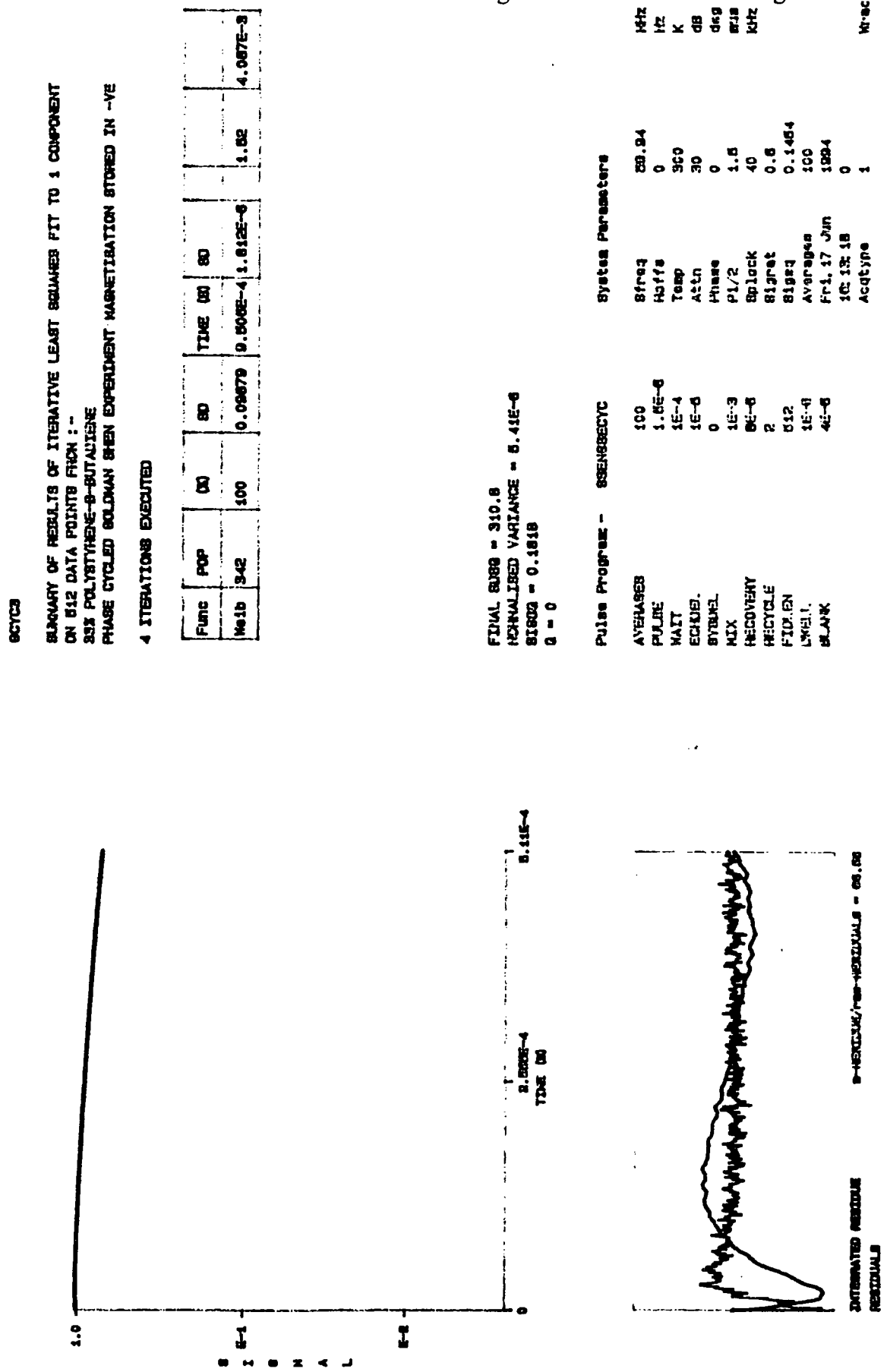

Experiment	Weibullian	Time ms^{-1}	Gaus+exponential
GGOLD1	403.1	9.0	20.6
GGOLD2	328.4	8.9	---
GGOLD3	347.8	9.2	---
GCYC1	418.2	9.4	23.3
GCYC2	349	9.3	---
GCYC3	342	9.5	---
GCYC4	400	9.7	35.2

Table 4.5 Effect of solid-echo pulse and phase-cycling on the Goldman-Shen experiment. The sequences involving a mix time had t_m = 1 ms and a wait time t_w = 10 ms.

Results from the standard Goldman-Shen sequence, but with the application of a solid-echo pulse, (GGOLD1) show that a small fraction of the original Gaussian+exponential components does indeed recover from spin-diffusion but the effect of no mixing time (GGOLD2) shows that the faster decaying component (Gaussian+exponential) has decayed effectively to zero, so proving that the fast decaying component detected in experiment GGOLD1 does result from spin-diffusion. Interestingly, storing the magnetisation in the negative z-axis (GGOLD3) shows that the faster decaying component is not detected after the mix time. This represents the situation where longitudinal (T_1) relaxation occurs during the mixing time so competing with the process of spin-diffusion, resulting in the loss of the faster decaying Gaussian+exponential components and the reduction in the signal internsity detected from the longer decaying Weibullian component.

This same pattern is repeated with the analogous phase-cycled Goldman-Shen experiments and the final experiment - GCYC4, where the magnetisation is stored in the positive z-direction but with no mix time, shows that less of an effect of T_1 relaxation occurs so that there is still a considerable signal from the Weibullian component but

spin-diffusion does occur resulting in the appearance of the faster decaying Gaussian+exponential component.

Unfortunately, these experiments are only qualitative, so a final pulse sequence was written to acquire a sequence of points as a function of the mixing time. There were the boundary conditions that needed to be fulfilled-

1 The signal obtained from both types of magnetisation storage must start with the same initial signal population (amplitude) values.

2 The sequence needed to sample enough points to obtain information about the process of spin-diffusion as a function of the mixing time.

3 The signal at the end of each experiment needed to reach the same level of intensity - needed to see that the magnetisation had reached its equilibrium value.

All these conditions required sampling of the signal at short, medium and long mixing times so the program was written incorporating sampling of the signal at concatenated (uneven) mixing times. To prevent inaccuracies during the experiments the sequence detected half of the sampled points using the experiment with storage of the magnetisation in the positive z-direction and half with the magnetisation in the negative z-direction.

The results obtained do follow the three boundary conditions and have now been used in a simulation designed by Alan Kenwright and Barry Say to determine a microdomain size. Graphically they can be seen in Graph 4.1-

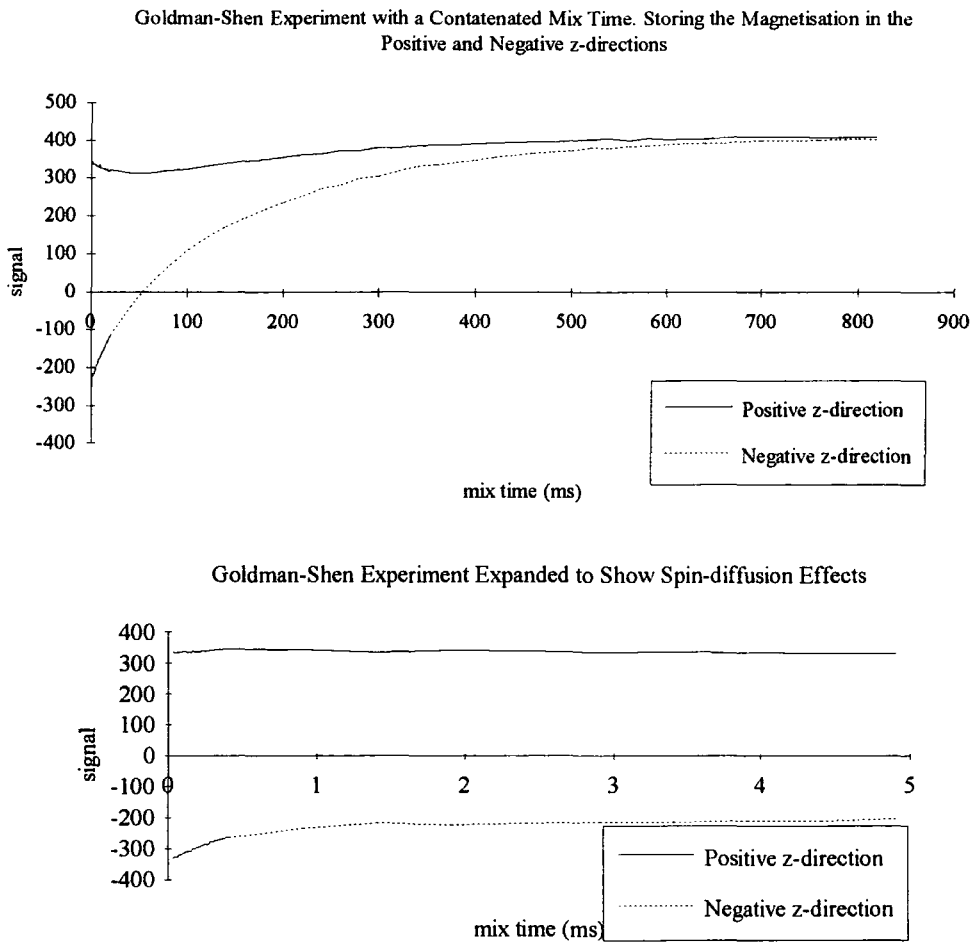

Graph 4.1 Two graphs showing the effect of T_1 relaxation and spin-diffusion on the positively- and negatively-stored magnetisation. The expanded graph highlights the effect of spin-diffusion recovering part of the magnetisation stored in the positive z-direction.

Clearly it can be seen that T_1 relaxation starts to really dominate over the effects of spin-diffusion at approximately 40 ms. Prior to this time spin-diffusion recovers some of the positively stored magnetisation hence increasing the signal intensity. Unfortunately, time constraints have prevented the completion of this work in terms of obtaining a domain size but these data are of sufficient quality to obtain some quantitative values on microdomain sizes since the distance between microdomains is proportional to the rate of spin-diffusion.

4.3 References

1 Goldman M., Shen L., 'Spin-spin Relaxation in LaF_2', *Phys. Rev.*, **1966,** 14, P321.

2 Powles J. G., Strange J. H., 'Zero Time Resolution Nuclear Magnetic Resonance Transients in Solids', *Proc. Phys. Soc.*, **1963**, 82, P6.

3 Baurn J. Munowitz. M, Garroway A. N. and Pines A., 'Multiple-quantum dynamics in solid state NMR', *J. Chem. Phys.*, **1985**, 83 (5), P2015.

4 Rosen M. E., 'Selective Detection in NMR by Time-Domain Digital Filtering', *J. Mag. Res.*, **1994** Series A 107, P119.

5 Ravikumar M., 'The Effect of a Single Non-selective Radiofrequency Pulse on the Creation of Multiple Quantum Coherences and on Coherence Transfer', *Chem. Phys. Lett*, **1988**, 144, P521.

6 Blechta V. and Schraml J., 'Spectral Artifacts Resulting from Multiple-Quantum Coherence Transfers by Spin Decoupling During Acquisition.', *J. Mag. Res.*, **1993**, Series A 101, P47.

7 Wokaun A. and Ernst R. R., 'Selective Detection of Multiple Quantum Transitions in NMR by Two-dimensional Spectroscopy', *Chem. Phys. Lett.*, 1977, 52, P407.

8 Bodenhausen G., Kogler H. and Ernst R. R., 'Selection of Coherence-Transfer Pathways in NMR Pulse Experiments.', *J. Mag. Res.*, **1984**, 58, P370.

9 Lynden-Bell R. M. and Bulsing J. M., 'A Vector Description of Multiple-Quantum Coherence in AX_n Spin Systems.', *J. Mag. Res.*, **1983**, 55, P128.

10 Bodenhausen G., 'Multiple-Quantum NMR', *Prog. NMR Spec.*, **1981**, 14, P137.

11 Bodenhausen G., Vold R. L. and Vold R. R., 'Multiple Quantum Spin-Echo Spectroscopy', *J. Mag. Res.*, **1980**, 37, P93.

12 Ernst R. R., Bodenhausen G. and Wokaun A., 'Principles of Nuclear Magnetic Resonance in One and Two Dimensions', Oxford Science Publications, **1991**.

13 Packer K. J. and Pope J. M., 'The distortion of NMR Spectra by Multiple Quantum Coherence Effects Resulting from Goldman-Shen and Related Pulse Sequences Applied to Heterogeneous Solids', *J. Mag. Res.*, **1983**, 55, P378.

14 Kenwright A. M. and Packer K. J., 'On T_1 Cancellation schemes in Goldman-Shen-type Experiments', *Chem. Phys. Lett.*, **1990**, 173, P471.

5.1 Introduction

The study of carbon in the solid-state can be extremely informative. The unfortunate attributes of ^{13}C nuclei are its low relative abundance compared to ^{1}H nuclei, i.e. 1.1%, and its low magnetogyric ratio which makes it more difficult to study compared to protons. As mentioned in the introduction, the use of magic-angle spinning, proton decoupling and cross-polarisation facilitate the study of ^{13}C nuclei. However, there are a number of important aspects of cross-polarisation dynamics that need to be considered.

5.1.1 Cross-polarisation Dynamics

The standard pulse sequence for cross-polarisation is as follows-

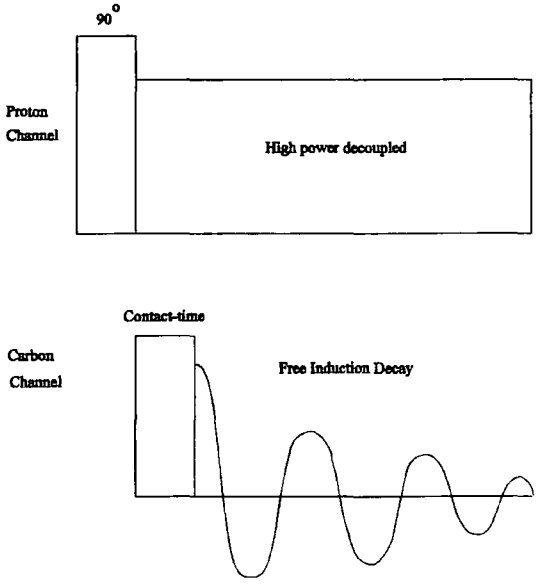

Figure 5.1 Pulse sequence used for cross-polarisation.

It consists initially of a 90° pulse on the proton channel which places the proton magnetisation into the xy-plane in the rotating frame of reference where it is spin-locked by a second pulse 90° out of phase with the first pulse. The dilute-spin channel

radiofrequency is switched on and transfer of magnetisation occurs from the abundant spin to the dilute-spin system during the contact-time. The evolution of the dilute-spin magnetisation can be derived if the spin-temperature of the system is considered. The inverse spin-temperatures of the abundant and rare spins - β_I and β_S - are proportional to the xy-plane magnetisation in the rotating frame. Assuming the exchange of magnetisation is energy-conserving in the rotating frame then-

$$\frac{d\beta_I}{dt} + \varepsilon\alpha^2 \frac{d\beta_S}{dt} = 0 \qquad \text{Eqn. 5.1}$$

$$\varepsilon = \frac{N_S S(S+1)}{N_I I(I+1)} \qquad \text{Eqn. 5.2}$$

$$\alpha = \frac{\gamma_S B_S}{\gamma_I B_I} \qquad \text{Eqn. 5.3}$$

where N is the number of spins and S/I are the angular momentum operators, γ is the magnetogyric ratio and B is the radiofrequency magnetic field in the rotating frame for both spin systems. ε is the relative amount (including spin factors) of the nuclei and α is the mismatch parameter which is based upon the Hartmann-Hahn matching condition. The rate that the magnetisation crosses over from the abundant to the rare-spin system is given by T_{IS}. However, the two respective spin systems decay whilst being spin-locked in their respective rotating frames, i.e. with characteristic times $T_{1\rho}$. Therefore, the overall differential equations describing the transfer of magnetisation are given by-

$$\frac{d\beta_S}{dt} = -\frac{(\beta_S - \beta_I)}{T_{IS}} - \frac{\beta_S}{T_{1\rho}{}^S} \qquad \text{Eqn. 5.4}$$

$$\frac{d\beta_I}{dt} = -\varepsilon\alpha^2 \frac{(\beta_I - \beta_S)}{T_{IS}} - \frac{\beta_I}{T_{1\rho}{}^I} \qquad \text{Eqn. 5.5}$$

There are boundary conditions necessary for the solution of these partial differential equations- $\beta_S(0) = 0$ and $\beta_I(0) \neq 0$, i.e. the rare spin system is not polarised at time zero. The resultant solutions were quoted by Mehring[1] and are as follows-

$$\beta_S(t) = \beta_I(0)\frac{1}{a_+ - a_-}\left\{\exp\left(\frac{-a_- t}{T_{IS}}\right) - \exp\left(\frac{-a_+ t}{T_{IS}}\right)\right\} \qquad \text{Eqn. 5.6}$$

$$\beta_I(t) = \beta_I(0)\frac{1}{a_+ - a_-}\left\{(1-a_-)\exp\left(\frac{-a_- t}{T_{IS}}\right) - (1-a_+)\exp\left(\frac{-a_+ t}{T_{IS}}\right)\right\} \qquad \text{Eqn. 5.7}$$

$$\text{Where } a_\pm = a_0\left(1 \pm \sqrt{1 - b/a_0^2}\right) \qquad \text{Eqn. 5.8}$$

$$a_0 = \tfrac{1}{2}\left(1 + \varepsilon\alpha^2 + \frac{T_{IS}}{T_{1\rho}{}^I} + \frac{T_{IS}}{T_{1\rho}{}^S}\right) \qquad \text{Eqn. 5.9}$$

$$b = \frac{T_{IS}}{T_{1\rho}}\left(1 + \frac{T_{IS}}{T_{1\rho}{}^S}\right) + \varepsilon\alpha^2\frac{T_{IS}}{T_{1\rho}{}^S} \qquad \text{Eqn. 5.10}$$

The development of the S-spin magnetisation - $M_S(t)$ - during the contact-time is proportional to the ratio of the spin-temperatures and $M_S(0)$ but the gyromagnetic ratios cancel (refer to Eqn. 5.3), i.e.-

$$M_S(t) = M_S(0)\alpha\frac{\gamma_I}{\gamma_S}\frac{\beta_S(t)}{\beta_I(0)} \qquad \text{Eqn. 5.11}$$

Placing equations 5.6 and 5.7 into equation 5.11 gives a more accurate description of the dynamics involved. However, there are certain simplifications that can be made. The Hartmann-Hahn matching will be exact so $\alpha = 1$, the S-spin system will be dilute so $\varepsilon \sim 1$ and the rotating frame longitudinal relaxation will only be significant for the abundant nuclei - $1/T_{1\rho}{}^S = 0$. This results in the following simplified equations-

$$b = \frac{T_{IS}}{T_{1\rho}^{I}} \qquad \text{Eqn. 5.12}$$

$$a_0 = \tfrac{1}{2}\left(1 + \frac{T_{IS}}{T_{1\rho}^{I}}\right) \qquad \text{Eqn. 5.13}$$

$$a_+ = 1 \qquad \text{Eqn. 5.14}$$

$$a_- = \frac{T_{IS}}{T_{1\rho}^{I}} \qquad \text{Eqn. 5.15}$$

This simplifies equations 5.6 and 5.7 into-

$$\beta_S(t) = \beta_I(0)\frac{1}{1 - T_{IS}/T_{1\rho}^{I}}\left\{\exp\left(\frac{-t}{T_{1\rho}^{I}}\right) - \exp\left(\frac{-t}{T_{IS}}\right)\right\} \qquad \text{Eqn. 5.16}$$

$$\beta_I(t) = \beta_I(0)\exp\left(\frac{-t}{T_{1\rho}^{I}}\right) \qquad \text{Eqn. 5.17}$$

Placing equations 5.16 and 5.17 into equation 5.11 gives a much simpler equation describing the dynamics of the cross-polarisation process-

$$M_S(t) = M_S(0)\frac{\gamma_I}{\gamma_S}\left[\frac{1}{1 + T_{IS}/T_{1\rho}^{I}}\left(\exp\left(\frac{-t}{T_{1\rho}^{I}}\right) - \exp\left(\frac{-t}{T_{IS}}\right)\right)\right] \qquad \text{Eqn. 5.18}$$

In what follows, $T_{1\rho}^{I}$ will be abbreviated as $T_{1\rho}$. Equation 5.18 can be simulated and looks like the following graph-

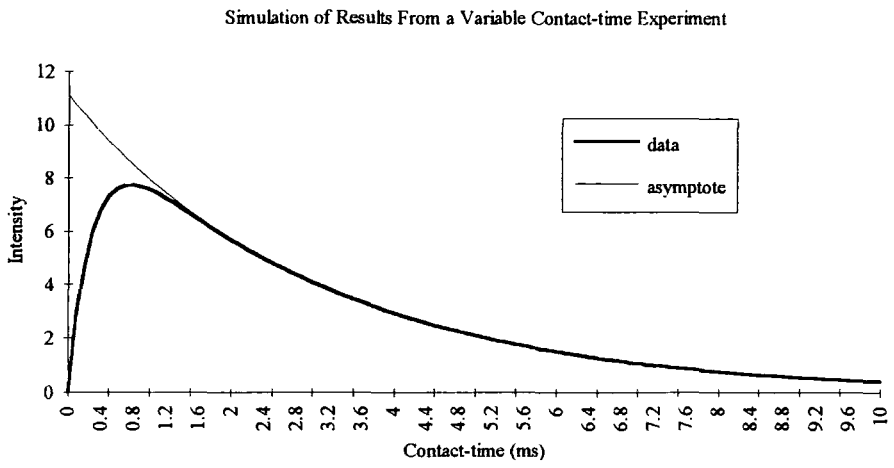

Figure 5.2 The $T_{1\rho}$ value was set at 3 ms and $T_{IS}=T_{1\rho}/10$. The asymptote was obtained from the equation $M_t = M_0 \exp(-t/T_{1\rho})/(1-T_{IS}/T_{1\rho})$.

M_0 is quantitative and is directly proportional to the number of active nuclei in the sample, while $T_{1\rho}$ can divulge information about the proton source of the cross-polarisation.

The cross-polarisation time T_{IS} is a measure of the efficiency of the cross-polarisation process, i.e. efficient cross-polarisation occurs between close nuclei that are not too mobile. T_{IS} can also be described as a ratio of the second moments (M_2) of the homo- and heteronuclear dipolar couplings and also varies with the sixth root of the hetero-internuclear distance, i.e-

$$\frac{1}{T_{IS}} \propto \frac{M_2^{IS}}{\sqrt{M_2^{II}}} \propto r_{IS}^{-6} \qquad \text{Eqn. 5.19}$$

There have been many assumptions used, such as the minimum value of T_{IS} occurring as the Hartmann-Hahn condition ($\alpha = 0$). If the system consists of a dilute rare-spin nucleus and the proton source is distinct from other sample protons then rapid magic-angle spinning can modulate the behaviour of T_{IS} from the Hartmann-Hahn matching condition. Such effects have been observed with systems with mobile/dilute

protons where homonuclear dipolar interactions are weak, i.e. Stejskal[2] et al. for ^{13}C CP/MAS NMR of adamantane.

There has also been observed modulation in the intensities obtained as a function of contact-time on a much longer time-scale compared to the weak homonuclear dipolar interaction effect, but on a short time-scale from the effects of directly-bonded nuclei. This is thought to be due to rapid spin-diffusion and resonance offset effects. Walther[3] et. al. reported this oscillatory behaviour and quoted the following equation-

$$M_t = \frac{M_0}{\lambda}\left[\exp\left(\frac{-t}{T_{1\rho}}\right) - a\exp\left(\frac{-t}{T_{IS}}\right) - [1-a]\left(\tfrac{1}{2}\exp\left(\frac{-t}{T_{II}}\right) + \tfrac{1}{2}\exp\left(\frac{-3t}{2T_{II}}\right)\cos\left(\tfrac{1}{2}bt\right)\right)\right] \quad \text{Eqn 5.20}$$

Where the spin-diffusion rate is denoted by the time constant T_{II}, $\lambda = (1-T_{IS}/T_{1\rho})$ and the fraction of protons which contribute as the main proton source is denoted by the parameter a. If a has a small value then oscillatory behaviour is dominant. The values of relaxation times T_1, T_{IS} and $T_{1\rho}$ will be compared to those values obtained from proton solid-state studies on the WRAC and will contribute to a more coherent understanding of the mobilities and interactions present in the diblock copolymers under investigation.

5.1.2 The CMX200 Spectrometer - Setup and Referencing

An rf pulse is generated by the synthesizer and transmitted through the rf cables via the broadband transmitter. After being amplified by the high-power amplifier the pulse is sent through a series-diode, a T-junction and a bidirectional coupler to the probe. This carrier pulse irradiates the spinning sample and certain nuclear transitions occur resulting in a small rf signal being carried back to the bidirectional coupler. Most of the carrier signal is blocked-out by the series diode and travels into the $\lambda/4$ cable. This cable's length is designed to destructively interfere for the carrier signal, leaving

the probe signal to reach the pre-amplifier and then be transmitted into the multichannel receiver where the final signal is again amplified and detected.

This can be clearly seen in the diagrammatic representation of the CMX200 schematics-

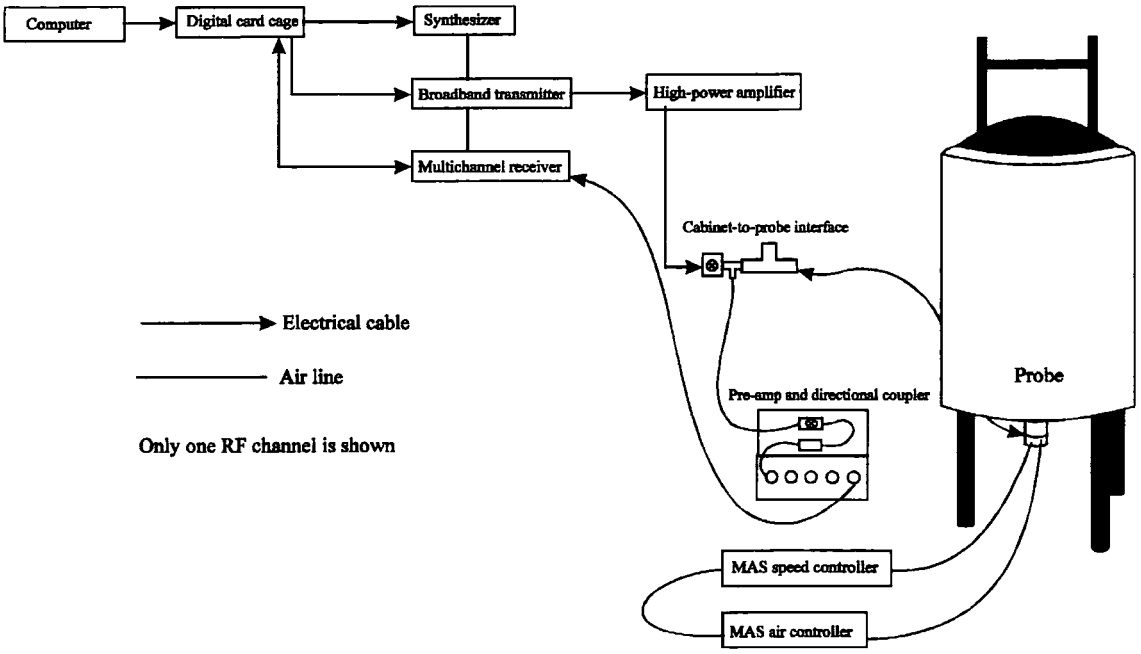

Figure 5.3 The CMX200 Spectrometer.

The sequence of events leading to the acquisition of a ^{13}C NMR spectrum are as follows-

1 The proton 90° pulse-duration is set using PDMSO (polydimethylsiloxane). This is achieved by setting the proton power to a value where a 9 μs pulse-duration produces a null-signal so that the 90° pulse-duration is at 4.5 μs.

2 The magic angle is set using KBr (detecting ^{79}Br) where a manifold of sidebands can be seen clearly producing spikes in the FID. Setting of the magic angle results in the optimum observation of these spikes. Alternatively, ammonium nitrate can be used (detecting ^{15}N) where the magic angle results in an isotropic powder pattern line-shape in the transformed spectrum, i.e. the peak-to-peak-width-at-half-height ($\nu_{\frac{1}{2}}$) is less than 7 Hz.

3 Finally the probe is referenced to adamantane (C_9H_{16}). This involves tuning and matching of the reflected power through the bidirectional coupler. This minimizes the reflected power of the carrier signal detected. Subsequently, the power levels for the proton and carbon channels are set to the Hartmann-Hahn optimum so that Eqn 5.21 is satisfied-

$$B^H\gamma^H = B^C\gamma^C \qquad \text{Eqn. 5.21}$$

where B is the resonance frequency of the nucleus and γ is its magnetogyric ratio. Analysis of the transformed spectrum of adamantane shows two peaks. The low frequency peak is set to 38.4 ppm which results in a referenced spectrum.

Once this procedure is complete the sample, containing carbon, under investigation can easily be analysed to give a referenced spectrum with correct chemical shifts.

5.2 Experimental Investigations

5.2.1 One-dimensional ^{13}C Spectra

Cross-polarisation Experiments

The pulse sequence used in this investigation involves cross-polarisation with a flip-back pulse which enables the magnetisation to reach the +z-axis after the delay of substantially less than $5T_1$ between each transient, provided $T_{1\rho}$ is sufficiently long. For heterogeneous samples the delay time may need to be carefully adjusted to prevent saturation of any signals which would affect the relative intensities of the peaks observed.

Spectra of the polyisoprene (TK124) and polybutadiene (SB5) copolymers were obtained (Spectra 5.1 to 5.3) and the following assignments were determined-

Table 5.1 ^{13}C CP/MAS Results for TK124 - Polystyrene-b-isoprene (Spectrum 5.1)

CHEMICAL SHIFT/ppm	ASSIGNMENT
23.8	cis isoprene CH_3 group
40	cis/trans backbone CH_2 of polyisoprene
63.2	CH_2 of polystyrene
73.9	CH of polyisoprene
84.65	CH of polystyrene
126.3	aromatic/C=C of polystyrene/polyisoprene
145.39	aromatic quaternary carbon in polystyrene
226.1	SSB

Spectrum 5.1 ^{13}C CPMAS spectrum of TK124 (Polystyrene-b-polyisoprene). Conditions used were a pulse delay of 5 s, the number of acquisitions were 792, a contact-time of 700µs and a spinning frequency of 5 kHz.

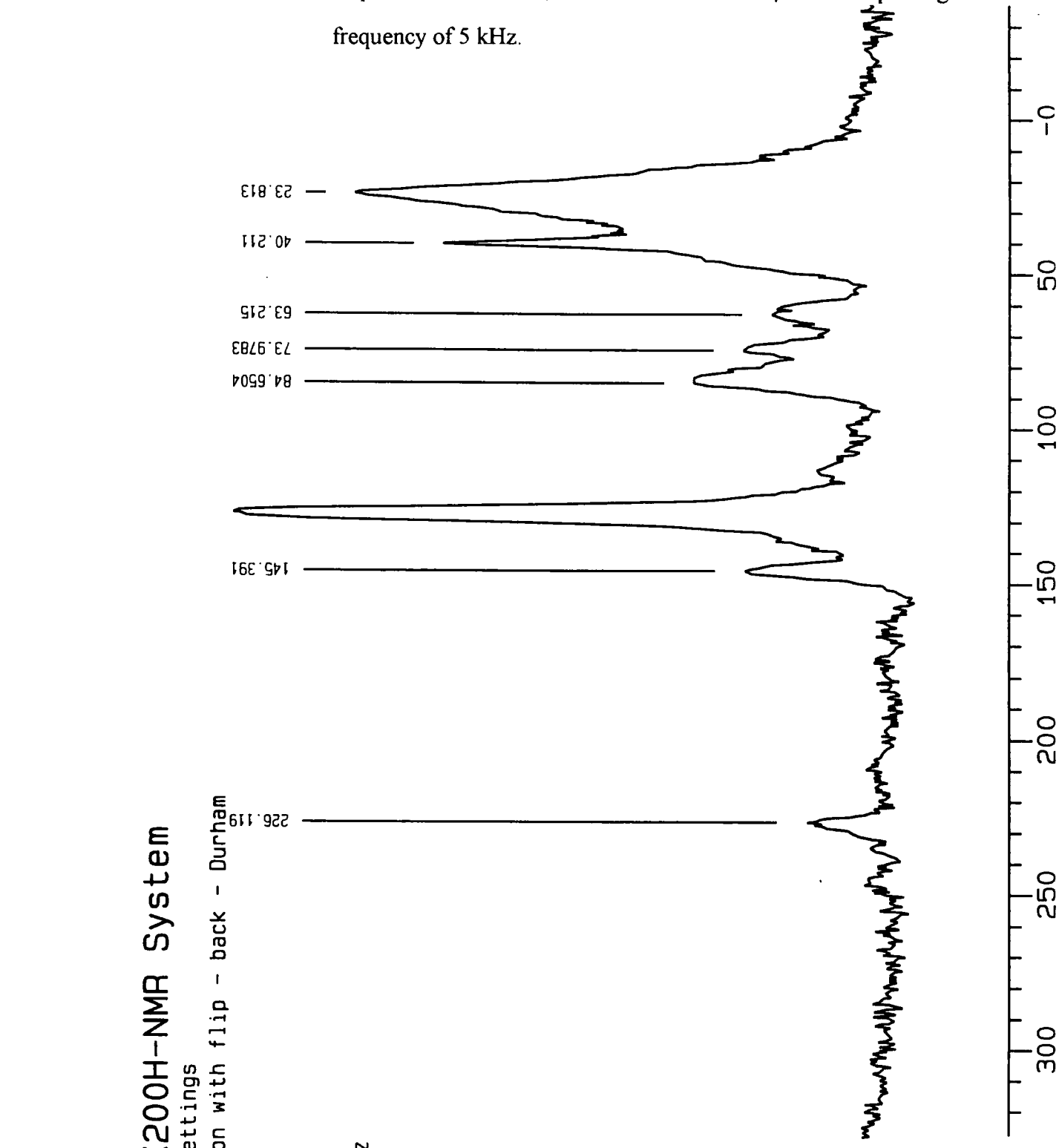

Spectrum 5.2 ^{13}C CPMAS spectrum of SB5 (Polystyrene-b-polybutadiene). Conditions used were a pulse delay of 5 s, the number of acquisitions were 800, a contact-time of 2 ms and a spinning frequency of 3 kHz.

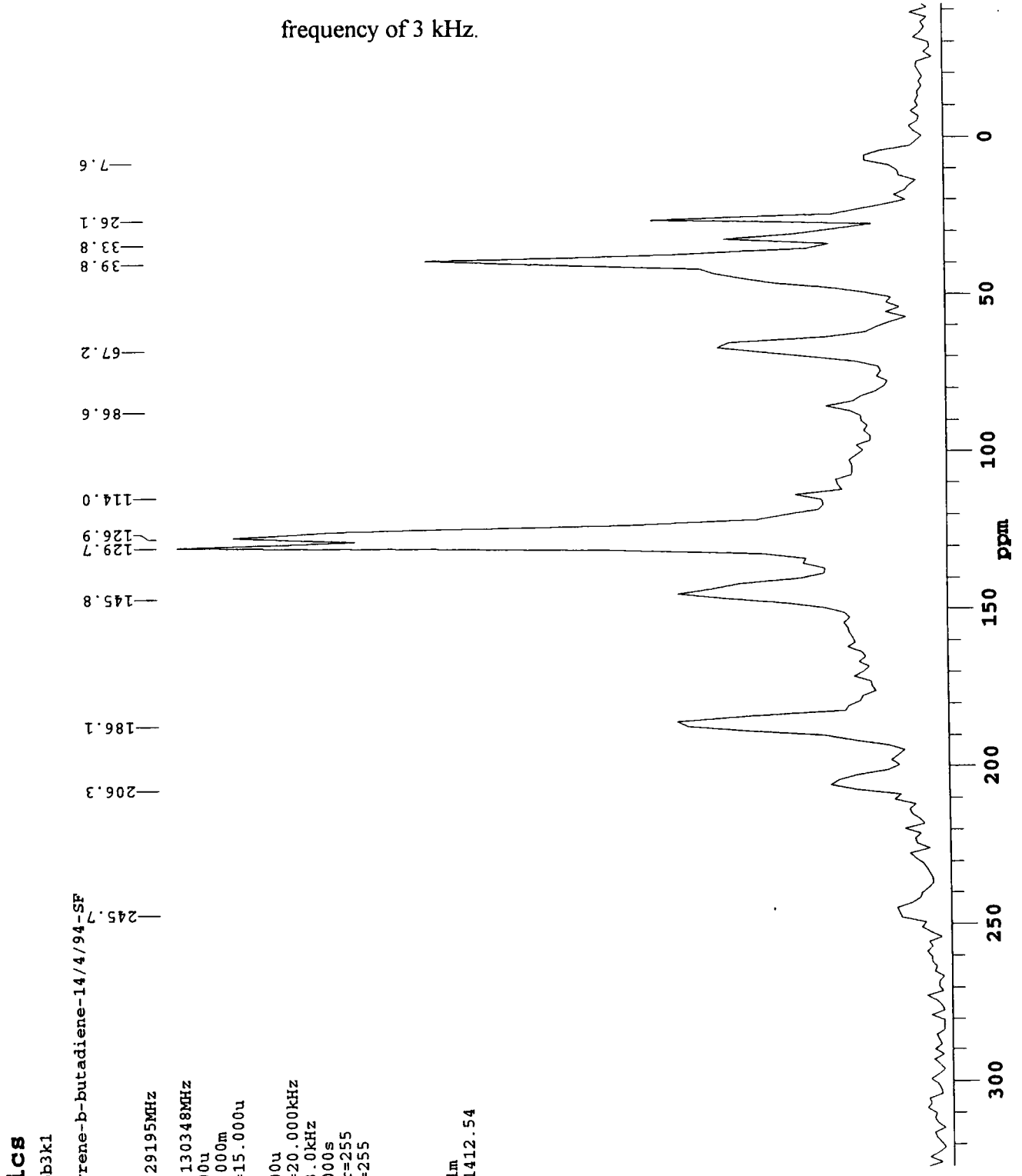

Spectrum 5.3 ^{13}C CPMAS spectrum of SB5 (Polystyrene-b-polybutadiene). Conditions used were a pulse delay of 5 s, the number of acquisitions were 800, a contact-time of 2 ms and a spinning frequency of 5 kHz.

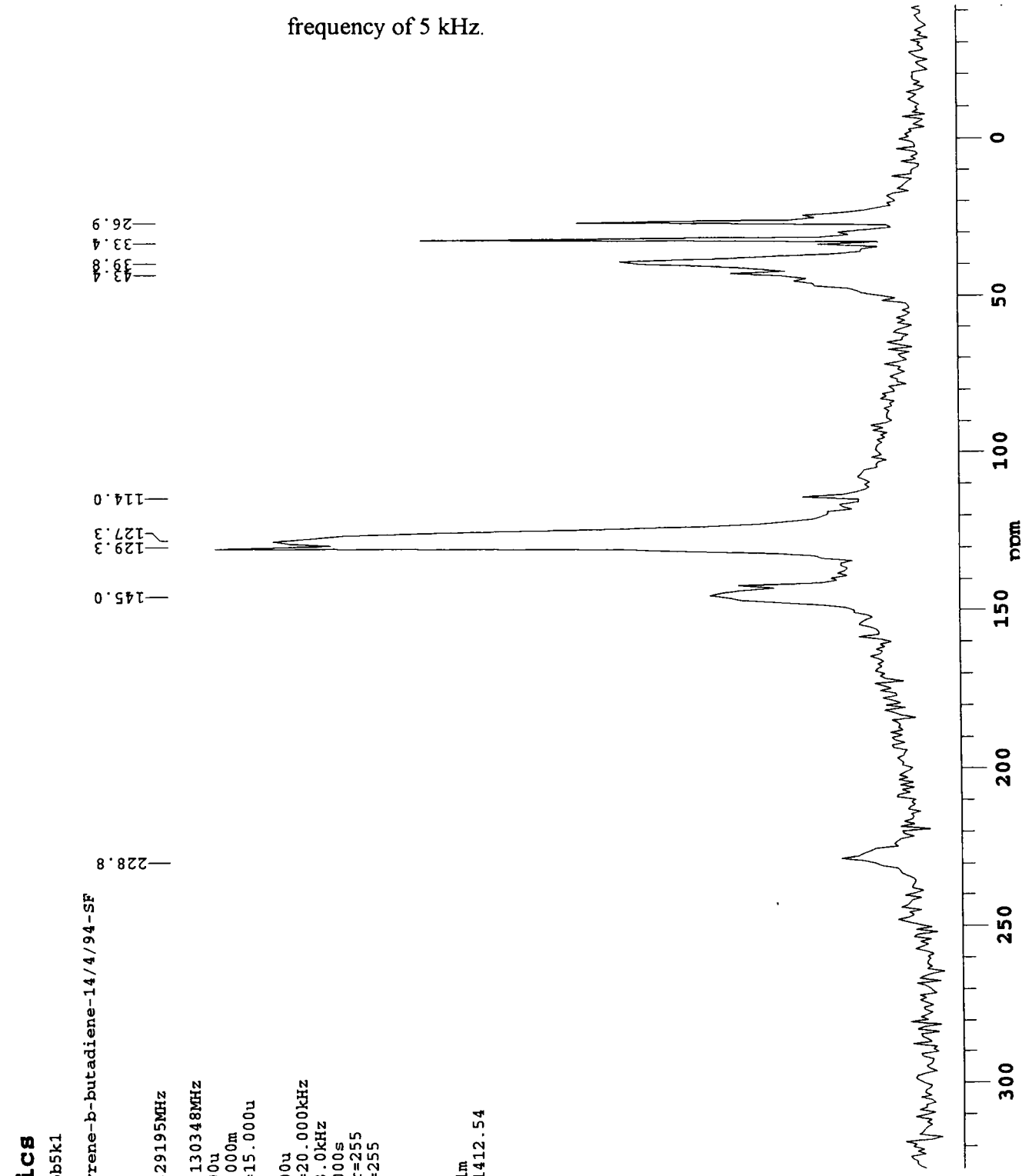

Chemagnetics
filename=sb1pspb5k1
ppfn=cpflip
com=SB1-polystyrene-b-butadiene-14/4/94-SF
ac=800
# acq's=800
ppg ch1=1
spect freq=50.329195MHz
ppg ch2=2
spect freq=200.130348MHz
pulse width=4.00u
contact time=2.000m
receiver delay=15.000u
dwell=50.000u
acq delay=15.000u
spectrum width=20.000kHz
filter width=13.0kHz
pulse delay=5.000s
H 90 & CP power=255
H decpl. power=255
rec. phase=157
acq length=512
dummy pulses=0
dim2 length=1
acq time=25.601m
receiver gain=1412.54

Table 5.2 ^{13}C NMR Results of SB5 (Spectra 5.2 and 5.3) - Polystyrene-b-butadiene (the gyroid structure)

Chemical Shift (ppm)	Assignment
28	butadiene methylene - cis conformation
33.4	butadiene methine - trans conformation
40.5	styrene methylene
67	SSB styrene
87	SSB styrene
128.5	styrene aromatic
130	butadiene vinyl
146.3	styrene quaternary aromatic carbon
187	SSB styrene
206	SSB styrene

The spinning-sidebands (SSB) were elucidated from analysis of the spectra using variable spinning frequencies - and the use of different contact-times determined that they were resulting from the rigid styrene moiety.

A series of experiments was completed to analyse the relaxation characteristics of the two polymers. These were-

i) VCT - variable contact-time experiment - to determine $T_{1\rho}$ indirectly

ii) Delayed contact-time (without spin-locking) - to determine T_2^*.(effective T_2, but magnetic field inhomogeneities fall within experimental error so will just consider T_2) and polymer mobilities

iii) Direct measurement of proton T_1 (by inversion-recovery) and $T_{1\rho}$

i) Variable Contact-time Experiments of TK124 and SB5

These experiments were used to study the cross-polarisation dynamics in both polymers and to measure indirectly some relaxation characteristics. The results are summarised in Table 5.3-

Peak	M_0	$T_{1\rho}$ ms^{-1}	T_{CP} μs^{-1}
Arom quaternary	18 (±2)	9 (±3)	39 (±1)
Arom/C=C polyisoprene	75 (±6)	10 (±4)	67 (±2)
CH polystyrene	22 (±1)	6 (±1)	197 (±5)
ssb polystyrene	16 (±1)	6 (±2)	17 (±44)
CH_2 polystyrene	11 (±1)	6 (±3)	12 (±5)
CH_2 polyisoprene	50 (±3)	8 (±2)	45 (±23)
CH_3 polyisoprene	62 (±4)	7 (±2)	7 (±2)

Table 5.3 Relaxation Times Resulting From Variable Contact-time Experiment of The Sample TK124 (Polystyrene-b-polyisoprene)

An important observation about these data is the consistency of the M_0 values in that those for the polystyrene are a third of those for the polyisoprene moiety which is consistent with the values obtained from the integrals in the solution-state NMR, i.e. the polystyrene CH group has a value of 22 and the CH_3 group of the polyisoprene has a value of 62. The M_0 values for the polystyrene quaternary (4C) and aromatic carbons are not correct since the spinning sidebands also contain some of the original intensity.

The $T_{1\rho}$ values for the blocks are very similar, indicating that rapid spin-diffusion is occurring so that on the timescale of analysis the spin-lock relaxation times are averaged. This may also be a result of intimate mixing. However, the polyisoprene group has a methyl group that can undergo rapid rotation about its 3-fold axis. This can act as a relaxation sink and cause the slowly decaying isoprene to increase its relaxation near to the rate of the polystyrene. The relaxation can be seen more clearly in the

graphs of the normalised signals obtained during the variable contact-time experiment - Graph 5.1 and Graph 5.2. The WRAC determined a value for $T_{1\rho}$, measured directly, of 6 ms which does fit within the experimental error of the indirect method.

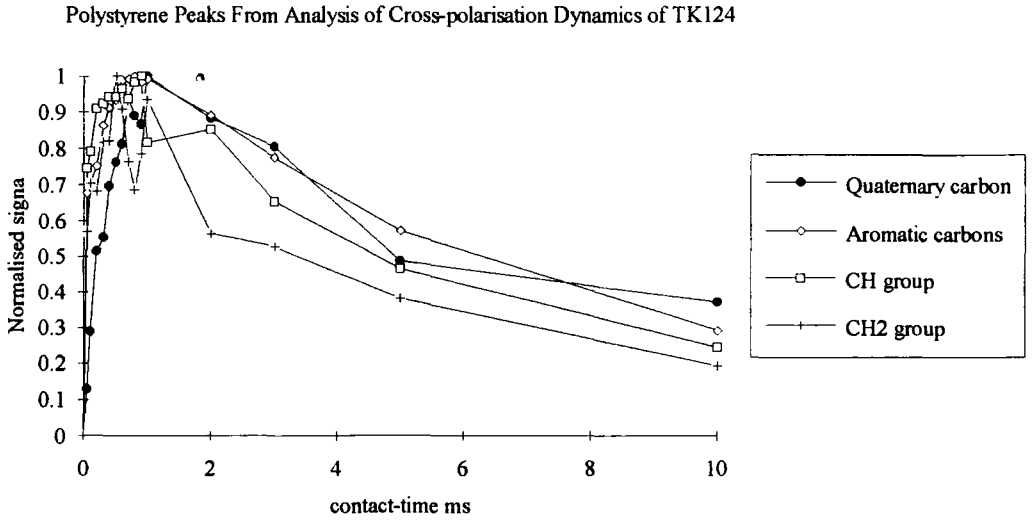

Graph 5.1 Variable contact-time experimental results of polystyrene peaks.

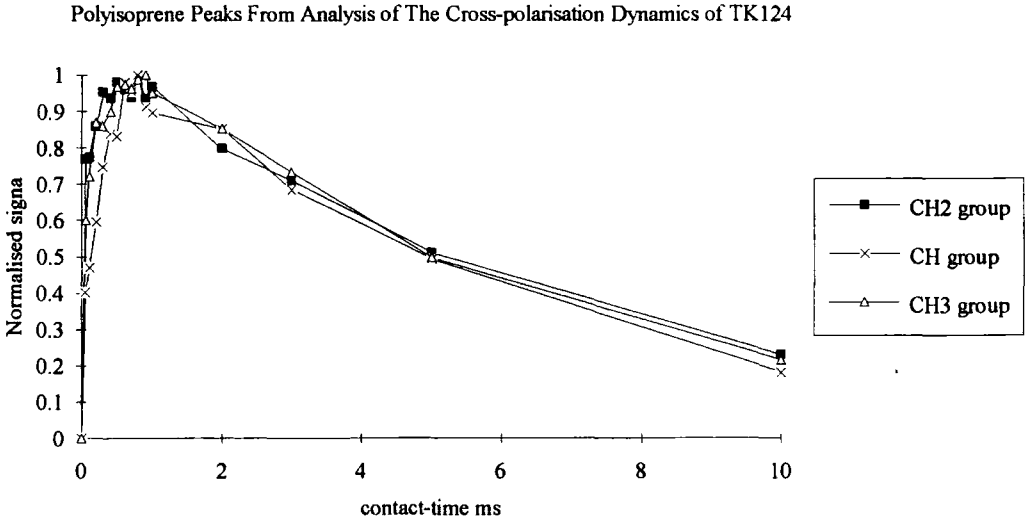

Graph 5.2 Variable contact-time experimental results of polyisoprene peaks.

Spectrum 5.4

^{13}C CP/MAS Variable Contact-time Stacked Plot of TK124 (Polystyrene-b-polyisoprene). Conditions used were a pulse delay of 5 s, the number of acquisitions were 792 per contact-time, a contact-time ranging from 0.1 ms to 10 ms and a spinning frequency of 5 kHz.

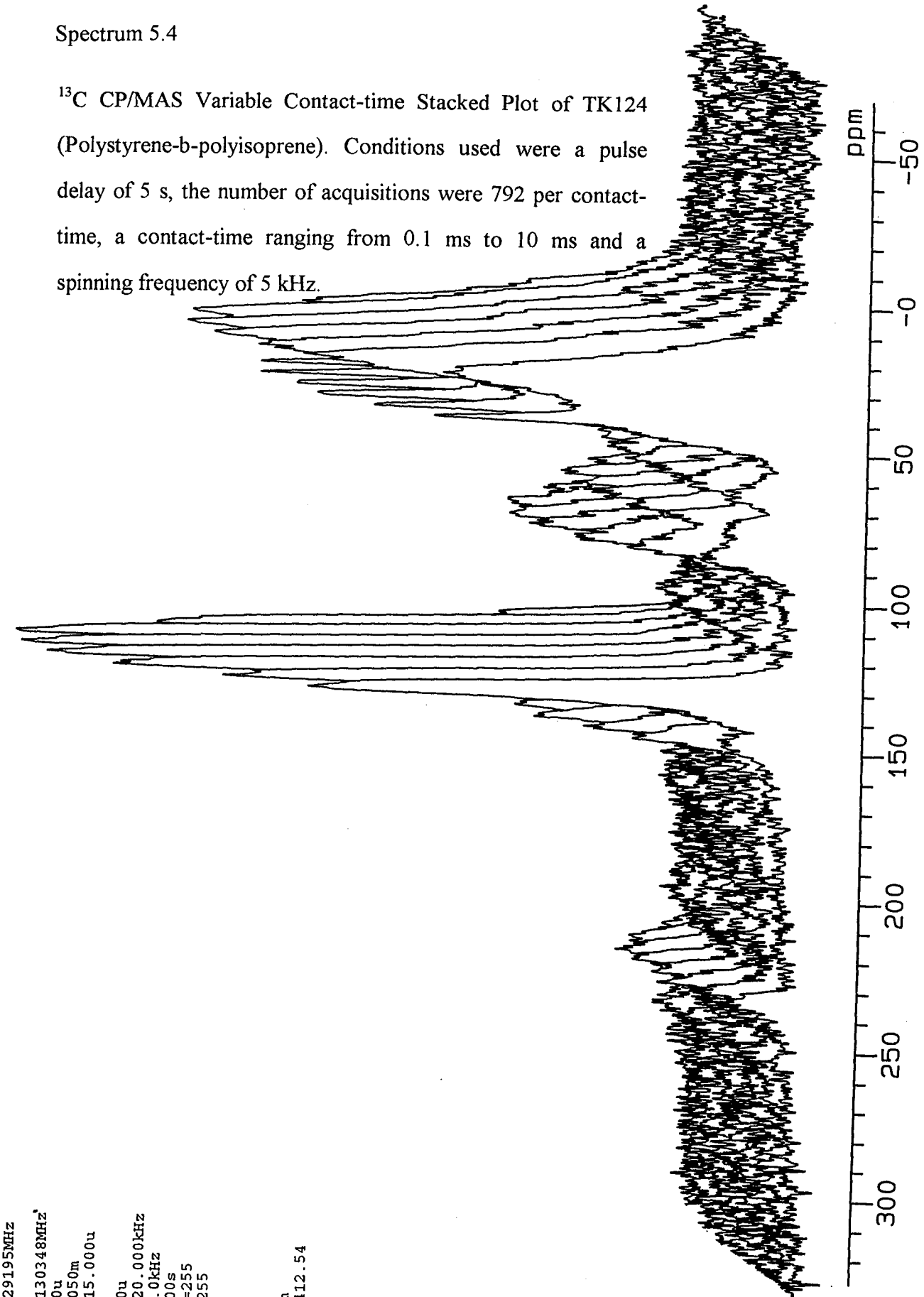

Chemagnetics

```
filename=13CVCT
ppfn=cpflip
com=Durham Initial Settings
ac=792
# acq's=792
ppg ch1=1
spect freq=50.329195MHz
ppg ch2=2
spect freq=200.130348MHz
pulse width=4.00u
contact time=0.050m
receiver delay=15.000u
dwell=50.000u
acq delay=15.000u
spectrum width=20.000kHz
filter width=13.0kHz
pulse delay=5.000s
H 90 & CP power=255
H decpl. power=255
rec. phase=157
acq length=512
dummy pulses=0
dim2 length=15
acq time=25.601m
receiver gain=1412.54
```

Table 5.4 Results From A Variable Contact-time Experiment For The Sample SB5 - polystyrene-b-polybutadiene

Peak	M_0	$T_{1\rho}$ ms^{-1}	T_{CP} μs^{-1}
polystyrene quaternary	39 (±1)	7 (±1)	3 (±5)
PBd vinyl + PSt arom	127 (±6)	9 (±1)	19 (±7)
polystyrene CH_2 + CH	98 (±1)	7 (±1)	18 (±8)
polybutadiene CH_2 (trans)	28 (±1)	47 (±16)	4 (±1)
polybutadiene CH_2 (cis)	14 (±1)	23 (±9)	2 (±2)

There is a marked difference between the $T_{1\rho}$ values of the polystyrene and polybutadiene blocks. This is due to the difference in their inherent mobilities - polystyrene is a rigid glass and so has a short $T_{1\rho}$ value, whilst polybutadiene is a mobile rubber and so has a longer $T_{1\rho}$ value. These data also show that spin-diffusion is not efficient enough to average the $T_{1\rho}$ values unlike the case for the polyisoprene analogue. Graphs 5.3 and 5.4 indicate the dramatic difference between the relaxation behaviour of the polystyrene and polybutadiene peaks. Notice, in particular, that the T_{CP} values are dramatically different between the two blocks. The polybutadiene block has a less effecient rate of cross-polarisation (T_{CP} is 2-4 μs) whereas the polystyrene block has a value of 18-19 μs. However, the polystyrene quaternery has a T_{CP} value of 3 μs which is consistent since the carbon has no directly-bonded protons so the rate of cross-polarisation will be dramatically smaller compared to the protonated polystyrene carbon atom analogues.

Due to the overlap of polybutadiene vinyl and polystyrene aromatic peaks and polystyrene CH and CH_2 peaks the modelling had to be made on the total of the peak heights. The values of M_0 should show a ratio of 3:1 in intensity for the polybutadiene:polystyrene, but this is not apparent from the data. This may be a direct result from a modulation in the observed amplitudes during the longer contact-times in the experiment, which could be a result of chemical shift modulation in the proton dimension, which results from the narrow separated resonances observed in the proton spectrum.

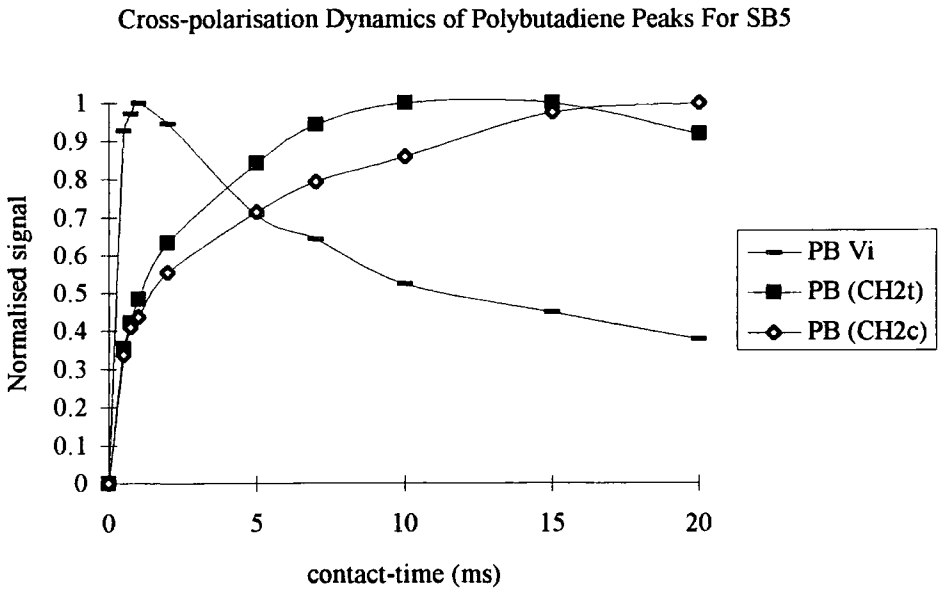

Graph 5.3 Variable contact-time results of polybutadiene peaks.

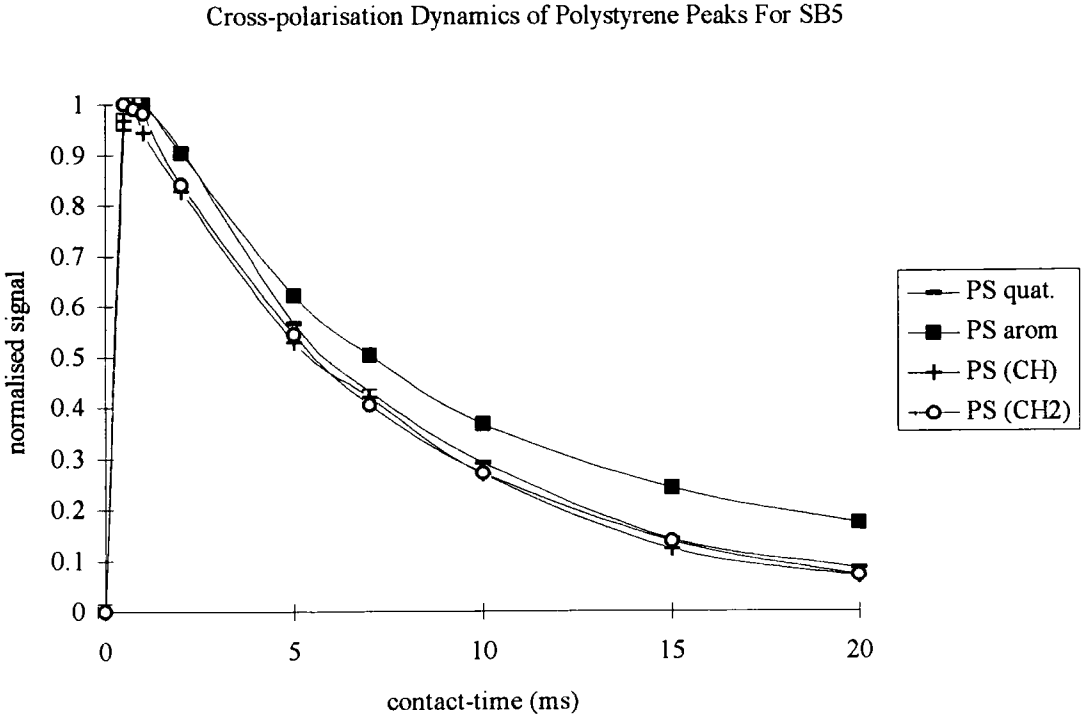

Graph 5.4 Variable contact-time results of polystyrene peaks.

The results from the direct measurement on the WRAC for polystyrene-b-butadiene show that the polystyrene $T_{1\rho}$ was 6 ms, which is comparable to the values obtained by the variable contact-time method. The $T_{1\rho}$ value for polybutadiene was measured as 24 ms, which is comparable to the value of 23 ms obtained for the cis methylene group. However, there is a large inconsistency with the trans peak which is also reflected by the large error associated with the result. This error derives directly from variations in matching conditions that occur during long contact-time cross-polarisation experiments. The original macro used analyses the signal intensity during each contact-time but this is not as accurate as measuring the area under each peak since the system under investigation has a large variation in the peak linewidth - between lorentzian and gaussian lineshapes. Another error results from the large degree of peak overlap in the spectra, which could be resolved if the spectra were deconvoluted and then each peak's integral measured.

ii) Delayed Contact-time Experiment Without Spin-locking

The delayed contact-time experiment was used to try and study T_2 relaxation during the delay before the contact-time between the proton and carbon channels. This experiment yields information about proton transverse relaxation via monitoring ^{13}C resonances. Spectrum 5.5 and Graphs 5.6 and 5.7 show how the ^{13}C resonances decay as a function of the delayed contact-time and comparison to their simulations are tabulated below:-

Peak	M_0	T_2 μs^{-1}	E (Weibullian index)
polybutadiene vinyl	54 (±40)	25 (±24)	1.0 (±1.2)
polystyrene quaternary	82 (±30)	15 (±4)	1.1 (±0.7)
polystyrene CH	14 (±5)	15 (±4)	1.7 (±1.2)
polystyrene CH_2	44 (±11)	14 (±3)	1.4 (±0.6)
polybutadiene CH_2 (trans)	9 (±3)	411 (±44)	1.0 (±2.0)
polybutadiene CH_2 (cis)	16 (±3)	810 (±100)	1.0 (±1.7)

Table 5.5 Results From The Delayed Contact-time Experiment For The Sample SB5 - Polystyrene-b-polybutadiene

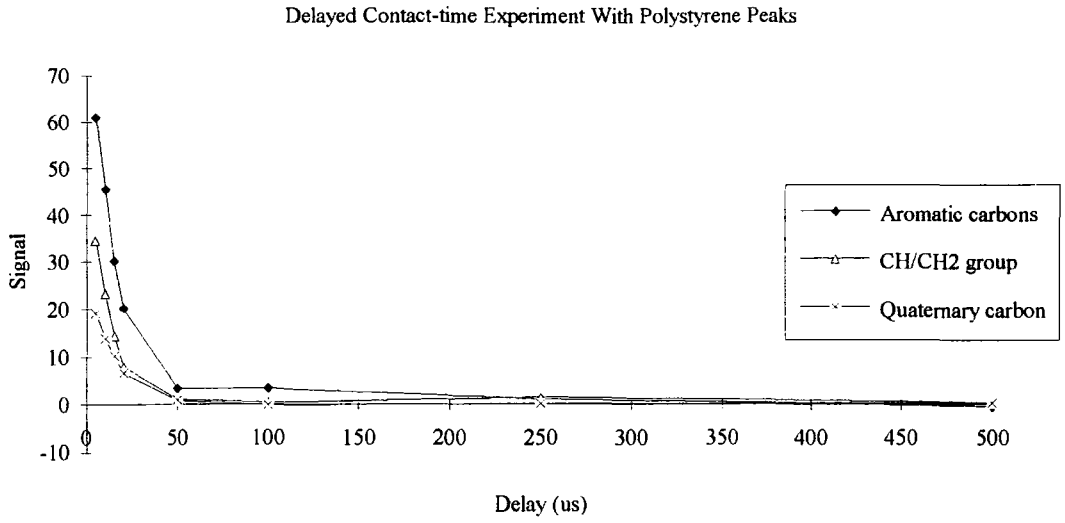

Graph 5.6 Delayed contact-time experimental intensities for polystyrene peaks.

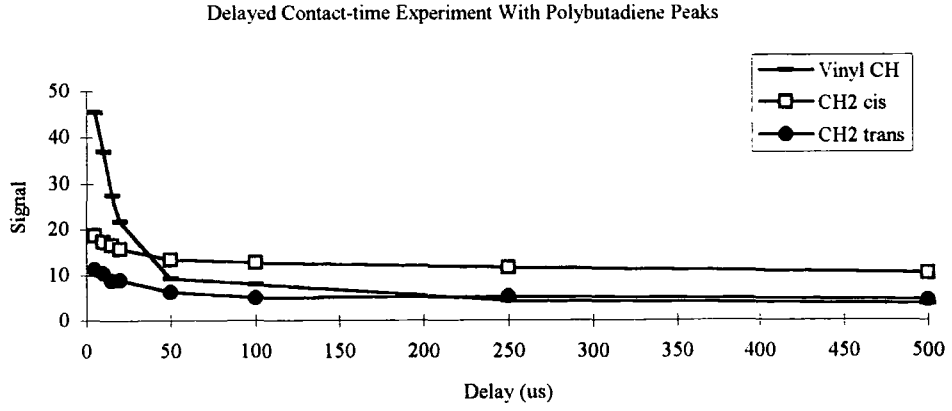

Graph 5.7 Delayed contact-time experimental intensities for polybutadiene peaks.

Spectrum 5.5 ^{13}C CP/MAS Delayed Contact-time Stacked Plot of SB5 (Polystyrene-b-polybutadiene). Conditions used were a pulse delay of 5 s, the number of acquisitions were 792 per contact-time, a contact-time delay ranging from 10 μs to 500 μs and a spinning frequency of 5 kHz.

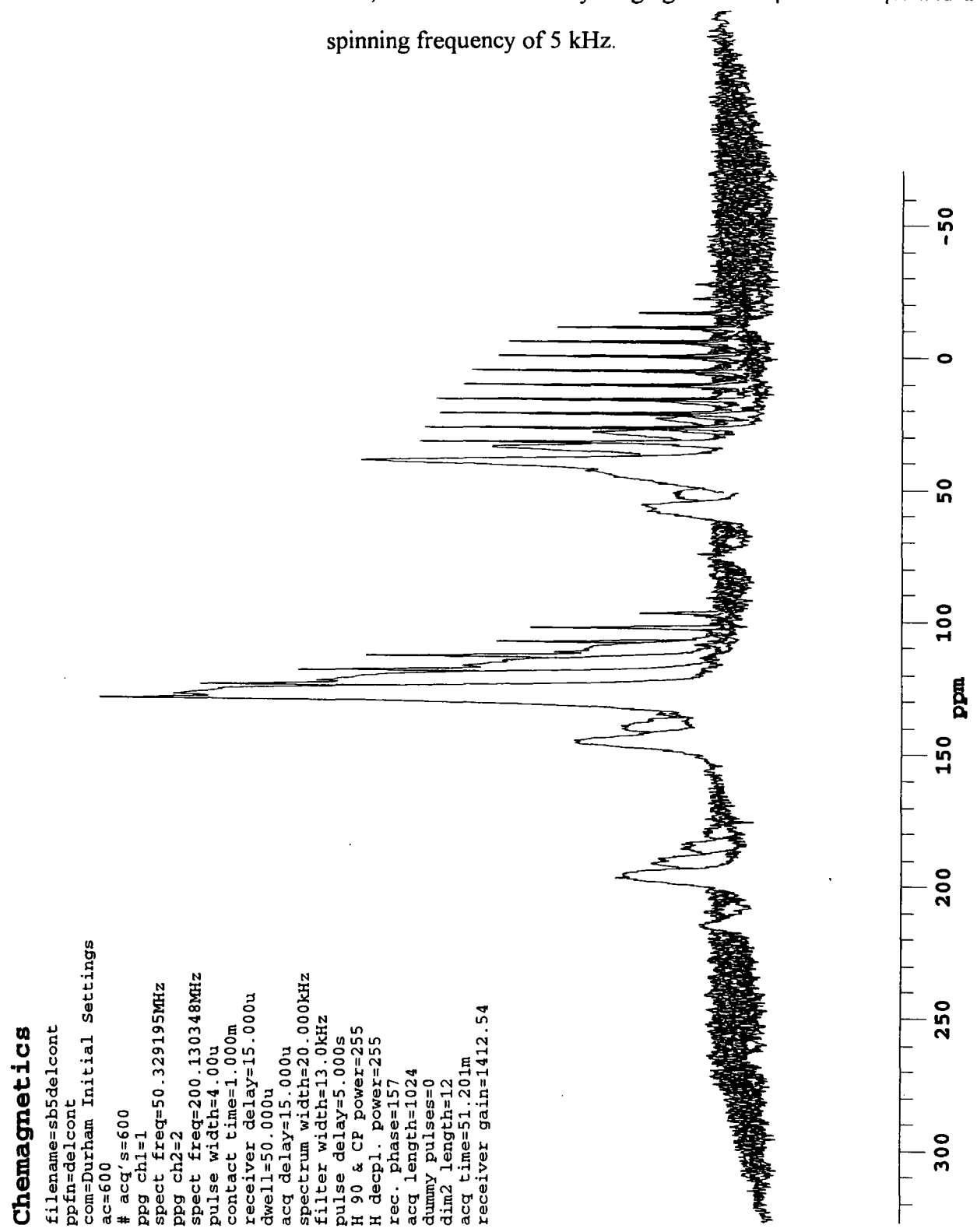

These data were obtained by trying to fit the spectral peak intensities to the equation for T_2 relaxation-

$$M_t = M_0 \exp\left(\frac{-t}{T_2}\right)^E \qquad \text{Eqn. 5.22}$$

The values of T_2 are relatively consistent with each of the peaks obtained from the polystyrene blocks with an average of 16 μs. The values of T_2 for the polybutadiene block are not consistent with each other - values of 25 μs for the vinyl moiety and 441 μs/810 μs for the trans/cis CH_2 moieties. This is due to the fact that the CH_2 peaks for the polybutadiene show little decay during the sequence so making it difficult to obtain an accurate value of T_2.

The Weibullian indices show that the polystyrene peaks are more gaussian (broader) than the polybutadiene peaks (if the Weibullian index is near 2 then the lineshape is described as Gaussian (more rigid) and if nearer 1 then the lineshape is described as Lorenztian (more mobile)).

Spectrum 5.6 and Graph 5.8 show how the ^{13}C resonances decay as a function of the delayed contact-time for sample TK124:-

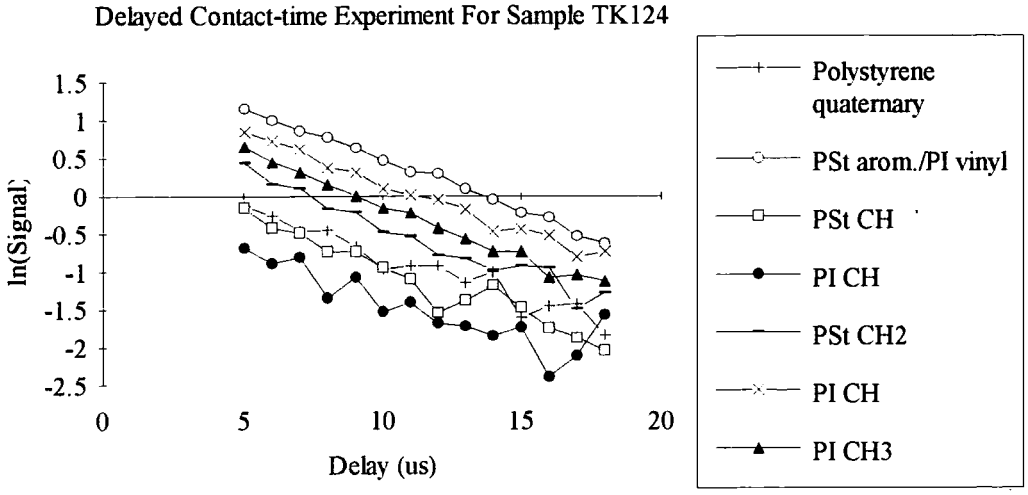

Graph 5.5 Delayed contact-time results for the peaks of sample TK124.

Spectrum 5.6 ^{13}C CP/MAS Delayed Contact-time Stacked Plot of TK124 (Polystyrene-b-polyisoprene). Conditions used were a pulse delay of 5 s, the number of acquisitions were 792 per contact-time, a contact-time delay ranging from 5 μs to 18 μs and a spinning frequency of 5 kHz.

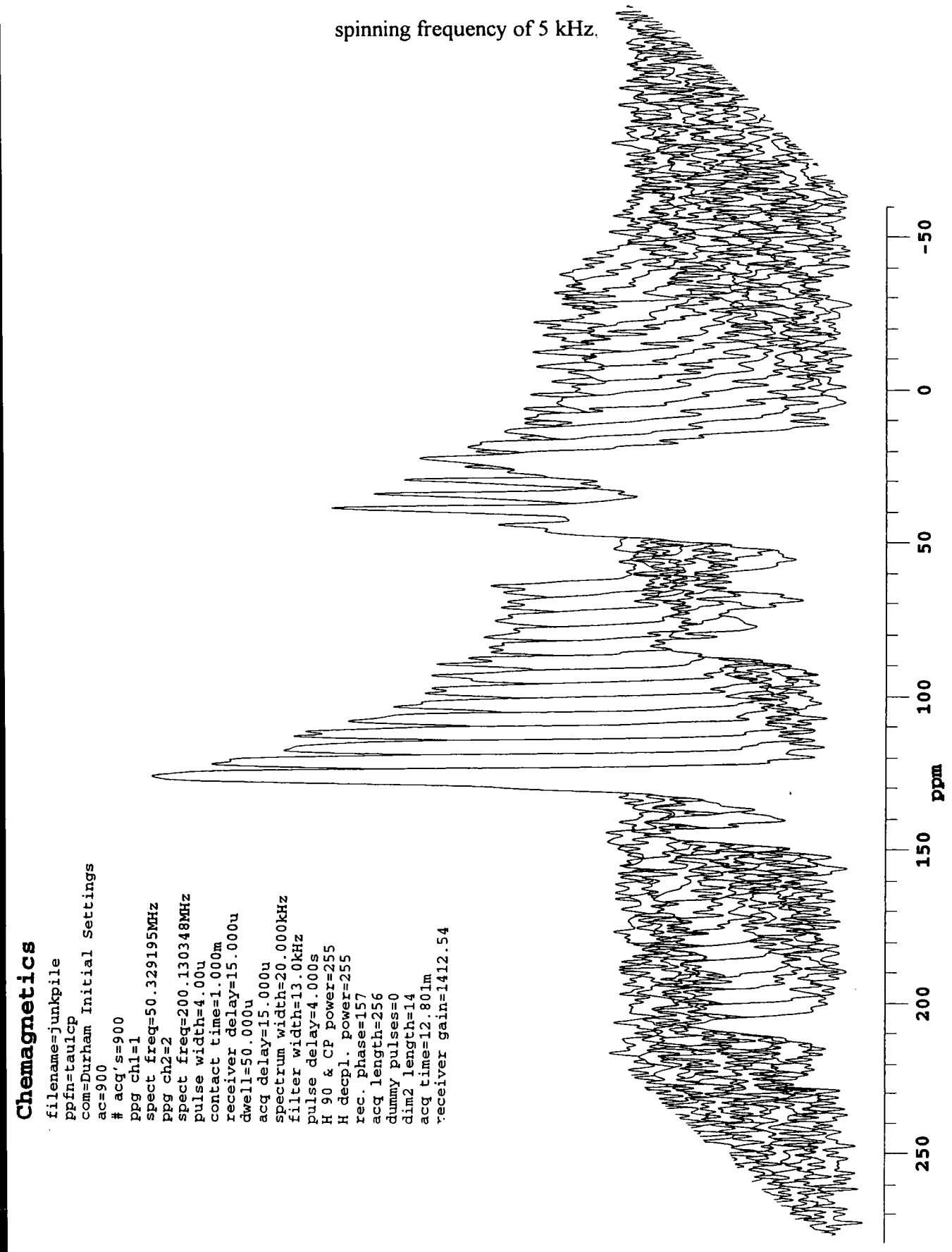

These results clearly show that there is rapid spin-diffusion occurring between the polystyrene and polyisoprene carbons. The T_2 values for all the detected carbon peaks vary between 6.7 ms to 8.2 ms with an error of a maximum of 0.5 ms. Again this perhaps shows the effect of the methyl group rotation allowing an efficient route for averaging-out the relaxation of the protons in both the polystyrene and polyisoprene.

iii) Direct Measurement of T_1 and $T_{1\rho}$

This was obtained from direct measurement of peak heights from the inversion-recovery sequence of transformed proton spectra (T_1) and transformed carbon spectra obtained at different spin-lock time increments ($T_{1\rho}$). These results should correspond to those values obtained from the WRAC. This is to test the validity of the data from both machines.

Table 5.6 Direct measurement of T_1 and $T_{1\rho}$ on the CMX200.

Experiment	TK124 Result (ms)	SB5 Result (ms)
Direct $T_{1\rho}$	----	26 ± 3
T_1^H by inversion-recovery	649 ± 50	279 ± 5 (CH_2) 253 ± 6 (pendant CH=CH)

The measurement of $T_{1\rho}$ directly for SB5 resulted in only the slowly decaying component being monitored. This is due to the fact that the polystyrene moiety could not be monitored because the linewidth of the transformed spectrum on the CMX200 is too broad to give a quantitative measure of its relaxation characteristics. The value of 26 ms is comparable to the WRAC value of 24 ms, but the WRAC also obtained a value for the faster decaying component of ca. 5 ms.

T_1 by inversion-recovery results in only one relaxation time detected for TK124, which is not surprising due the effect of spin-diffusion averaging all the rates of motion. Comparison to the result from the WRAC, which was 720 ms, shows that there may be

a small effect caused by the different field-strengths used by the two spectrometers. The CMX200 has a field-strength equivalent to 200 MHz while the WRAC has a field-strength equivalent to 60 MHz. The larger field-strength should result in a longer T_1 value but is not clearly seen, i.e. a value of 649 ms compared to the 720 ms obtained by the WRAC, however, these results do fall within each others respective errors.

The results for the polybutadiene moiety show that there may be a slight difference in the relaxation of the backbone CH_2 group and the pendant vinyl group found in the 1,2 adduct. The WRAC results showed a single value, for the polybutadiene CH_2 group, of 186 ms which is very different from the value ca. 270 ms from the CMX200. This is not surprising since the CMX200 value should be longer than the value obtained by the WRAC.

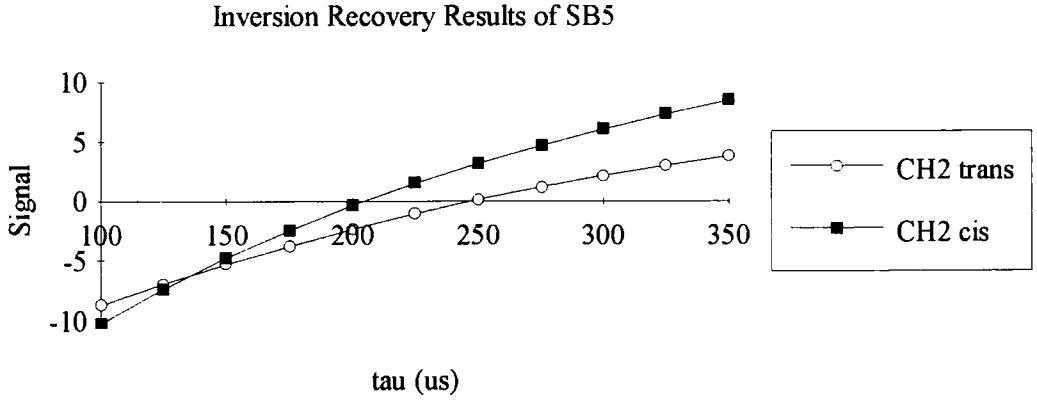

Graph 5.7 Signal intensities obtained from an inversion-recovery experiment on SB5.

Spectrum 5.7 Inversion-recovery Proton Spectrum For Sample SB5 - Polystyrene-b-polybutadiene. Conditions used were a pulse delay of 5 s, 8 acquisitions per recovery time and a range of recovery times (tau) from 100 μs to 350 μs .

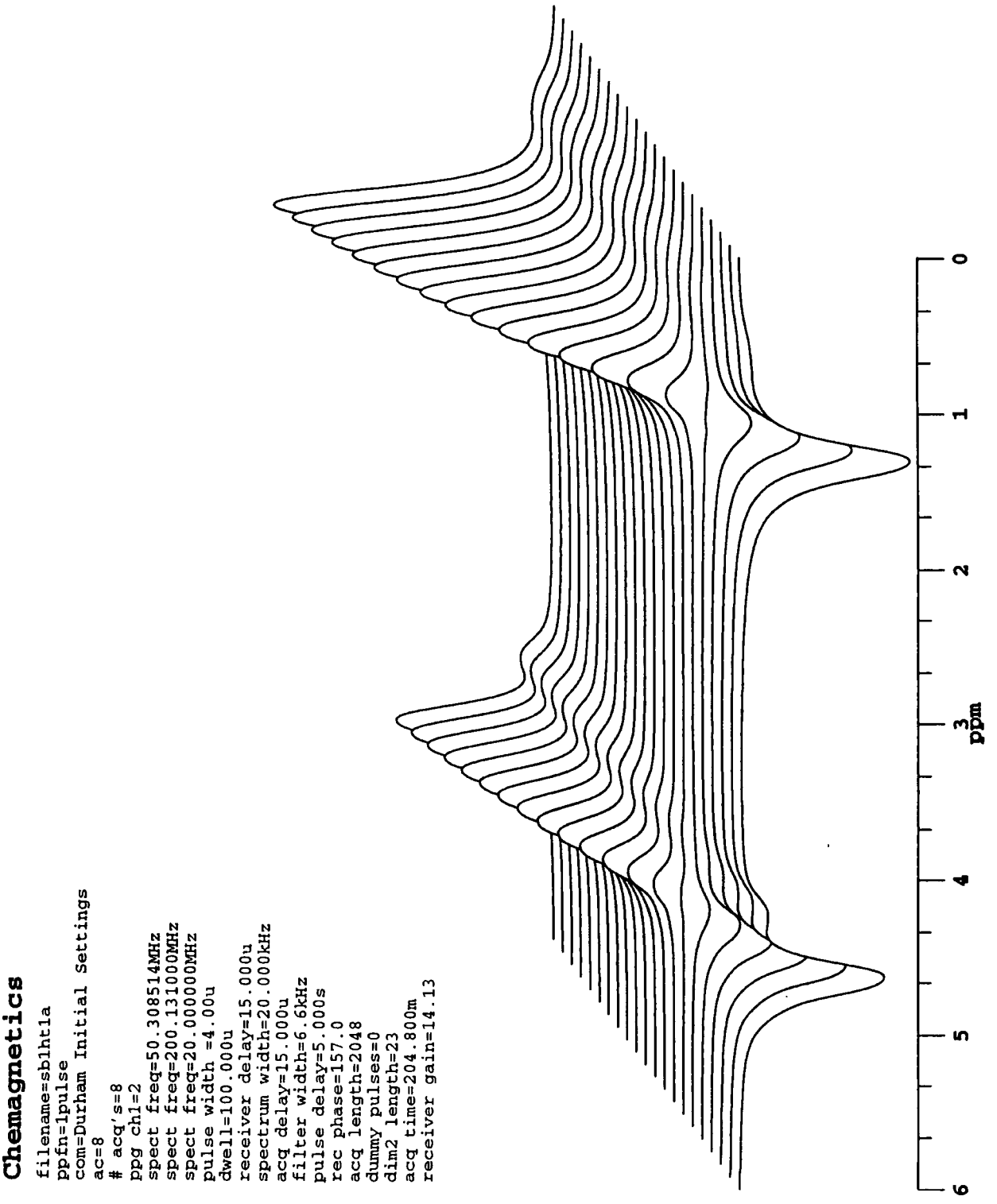

5.2.2 Correlated Spectroscopy, Especially The WISE Experiment[4]

Before describing research into the two-dimensional WISE experiment, a description of the problems associated with acquisition of two-dimensional data sets is introduced.

5.2.2 (a) Problems Associated With Two-dimensional NMR - A Description of the One-dimensional Case Detailing the Types of Analysis to Detect the Real (Absorption) Component of the Audio Signal

1 Off-resonance Single-channel Detection[5]

The carrier frequency is placed to one side of the spectrum so that all the detected resonances are either positive or negative with respect to the carrier frequency-

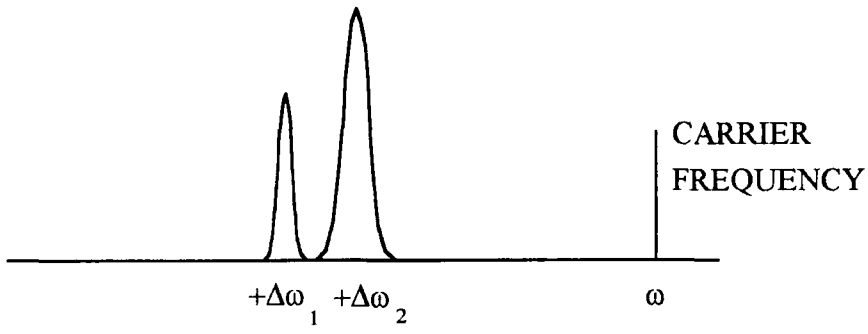

Figure 5.4 Off-resonance detection of the frequency-domain.

Unfortunately, this system of detection results in a dramatic reduction in the signal-to-noise ratio because the spectral width is double that for the case when the carrier frequency is in the centre of the spectrum.

2 Quadrature Detection[5]

One way to determine the sign of the precession of the magnetisation is to use quadrature detection. This involves the use of mixers to select only the real component of the resultant audio-signal with subsequently symmetrization of the data. Quadrature detection is needed when digitising the frequency oscillations - and the use of audio filters allows only the lowest frequencies through without amplifying noise. Quadrature detection thus helps determine the sign of the frequency oscillations-

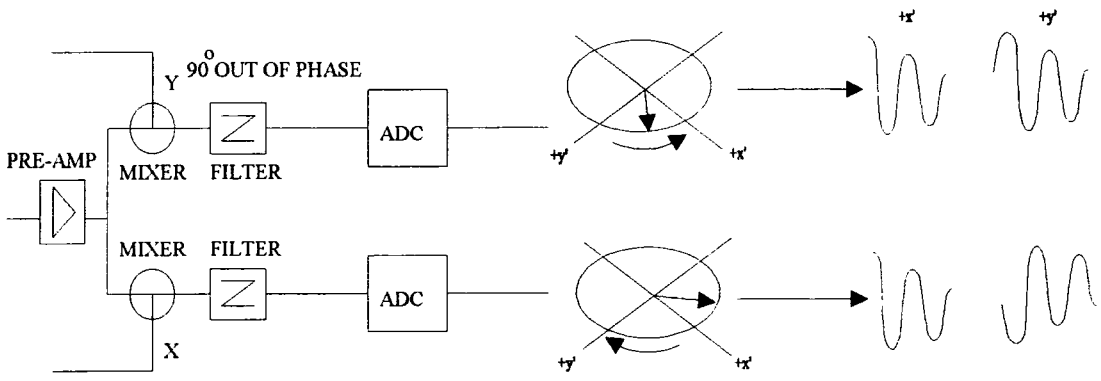

Figure 5.5 The setup used for quadrature detection.

The vector precesses in the rotating frame with a frequency offset of $+\Delta\omega$ from the transmitter carrier so the signal induced is $F(t) = \cos\Delta\omega t$. Thus, upon Fourier transformation this gives the response-

$$F(\omega) = \tfrac{1}{2}[\mathrm{Abs}(+\Delta\omega) + i\mathrm{Dis}(+\Delta\omega) + \mathrm{Abs}(-\Delta\omega) + i\mathrm{Dis}(-\Delta\omega)] \qquad \text{Eqn. 5.23}$$

This results in a transformed spectrum with resonance lines at $\pm\Delta\omega$. However, quadrature detection is undertaken by a shifter channel which causes a phase-shift in the channel to detect $i\sin(\Delta\omega t)$ so that the detected signals combined are-

$$F(t) = \cos\Delta\omega t + i\sin\Delta\omega t \qquad \text{Eqn. 5.24}$$

so transforming this gives-

$$F(\omega) = Abs(+\Delta\omega t) + iDis(+\Delta\omega t) \qquad \text{Eqn. 5.25}$$

Notice that the sign of the precession is now known. Thus, the real signal can be easily distinguished and should be in full absorption mode.

3 TPPI - Time-proportional Phase Increment[5]

This applied whilst acquiring points of the FID - it is a phase increment between acquired points and not between transients (as in CYCLOPS/Phase Cycling). TPPI creates off-resonance conditions whilst having the first sampling phase on-resonance! This results in the carrier frequency sitting at one side of the spectral window and allows determination of the sign (direction) of the precessional frequency-

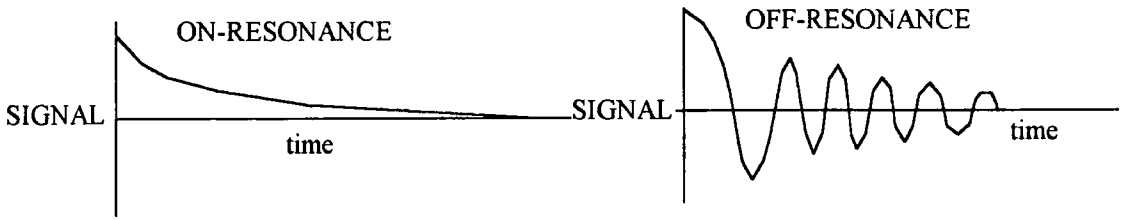

Figure 5.6 On- and Off-resonance Detection

5.2.2 (b) A Brief Description of Two-dimensional NMR[6]

This is different from the one-dimensional case in that there are two time-domains and the second pulse is applied to a spin system that is not in thermal equilibrium. The sequence can be described by four regions-

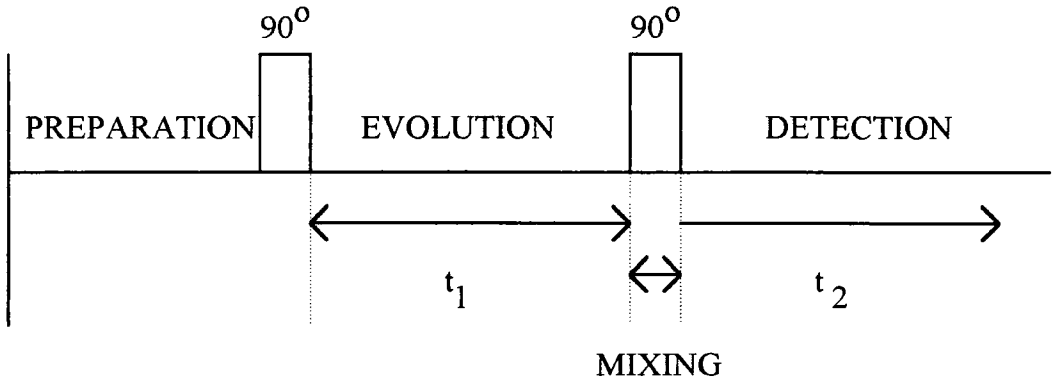

Figure 5.7 The sequence of events involved during acquisition of a generalised two-dimensional spectrum.

1 The Preparation Period - this involves the creation of the transverse magnetisation

2 The Evolution Period - this is where the spin-system evolves for a period of time - t_1 - which is varied.

3 The Mixing Period - during this time the transfer of coherences and magnetisation occurs.

4 The Detection Period - the transverse magnetisation is created in the second dimension by the second pulse during the time t_2. Thus, an FID is obtained during the time t_2 for each time period - t_1. It is easy to phase the t_2-dimension to obtain a purely absorption component but it is more difficult to phase the t_1-dimension.

(i) The Removal of the Dispersive Components in Two-dimensional Spectra.

There are three methods available[7]-

1 Shifting the phase of the receiver and all the pulses preceding t_1 by $\pi/2$ radians. Signals are selected which have identical signs in the ω_1- and ω_2-dimensions. If the receiver and pulses are of opposite phase then this results in signals of signs in the ω_1-dimension which are opposite to those found in the ω_2-dimension. These are called anti-echo- (p-type) and echo- (n-type) peaks, respectively. However, this results in a phase-twist lineshape due to phase modulation during the t_1-domain.

2 Generation of complex data with respect to the t_1-domain.

3 Real Fourier transformation with respect to the t_1-domain.

(ii) Frequency Discrimination

The general amplitude- (cosine) modulated time-domain signal is described as-

$$S_c(t_1,t_2) = \sum_i a^{(i)} \cos\left(\Omega_1^{(i)} t_1\right) \exp\left(-t_1 / T_{2,1}^{(i)}\right) \exp\left(\Omega_2^{(i)} t_2\right) \exp\left(-t_2 / T_{2,2}^{(i)}\right) \exp\left(i\phi_2^{(i)}\right)^2 \quad \text{Eqn. 5.26}$$

$\Omega_1^{(i)}$ and $\Omega_2^{(i)}$ are the resonance frequencies in the ω_1- and ω_2-dimensions of peak i.

$T_{2,1}^{(i)}$ and $T_{2,2}^{(i)}$ are the spin-spin relaxation time constants during the periods t_1 and t_2.

$\phi_2^{(i)}$ is the phase factor for phase errors in the pulse sequence used.

$a^{(i)}$ is an intensity factor.

The result of one Fourier transformation is a damped oscillator function-

$$FT\left\{\exp\left(i\Omega_2 t\right)\exp\left(-t / T_2\right)\right\} = \tfrac{1}{2}\left\{\left(A_2 + iD_2\right)\left(\exp\left(i\Omega_1 t_1\right) + \exp\left(-i\Omega_1 t_1\right)\right)\right\} \quad \text{Eqn. 5.27}$$

Where $A_2(\omega) = \frac{T_2}{\left[1+(\omega_2-\Omega_2)^2 T_2^2\right]}$ Eqn. 5.28

And $D_2(\omega) = \frac{(\omega_2-\Omega_2)T_2^2}{1+(\omega_2-\Omega_2)^2 T_2^2}$ Eqn. 5.29

A_2 and D_2 are the absorption and dispersion Lorentzians at frequency Ω_2 in the ω_2-frequency domain. A second transformation in the ω_1-dimension (with no sign discrimination) gives-

$$s_c(\omega_1,\omega_2) = \tfrac{1}{2}\left[\left(A_1^+ - iD_1^+ + A_1^- + iD_1^-\right) + \left(A_2 - iD_2\right)\right] \quad \text{Eqn. 5.30}$$

This leaves the real component as-

$$\mathrm{Re}\left[s_c(\omega_1,\omega_2)\right] = \tfrac{1}{2}\left[\left(A_1^+A_2 - D_1^+D_2\right) + \left(A_1^-A_2 - D_1^-D_2\right)\right] \quad \text{Eqn. 5.31}$$

This real component of the overall spectrum contains both absorption and dispersion components. This is known as the phase-twist lineshape. This can be converted to a double absorption lineshape by folding the data points around $\omega_1 = 0$ and ignoring the imaginary components from the transformation resulting in the real part of the spectrum becoming-

$$\mathrm{Re}\left[s_c(\omega_1,\omega_2)\right] = \tfrac{1}{2}\left[\left(A_1^+A_2\right) + \left(A_1^-A_2\right)\right] \quad \text{Eqn. 5.32}$$

Notice there is still no sign discrimination in the ω_1-dimension. An initial solution implemented to solve this problem was to use phase-cycling during the t_1-time period but this method reintroduces the phase-twist.

(iii) Techniques Used to Obtain Pure Two-dimensional Spectra

1 Echo and Anti-echo (p- and n-type) Selection

This involves discriminating the frequency in the ω_1-domain by recording a second amplitude-modulated component as a sine modulation-

$$s_c(t_1, t_2) = \sin(\Omega_1 t_1)\exp(i\Omega_2 t_2) \qquad \text{Eqn. 5.33}$$

This is achieved by shifting the phase of all of the pulses by 90° for single-quantum coherences. The sine and cosine signals are combined in the receiver as a part of the normal phase-cycling procedure. The receiver also has a 90° phase shift resulting after Fourier transformation in the real part of the spectrum as-

$$\mathrm{Re}[s(\omega_1,\omega_2)] = (A_1^+ A_2 - D_1^+ D_2) \qquad \text{Eqn. 5.34}$$

This has created the unfavourable phase-twist lineshape but has discriminated the sign of Ω_1. However, prior to detection of the t_2-domains, if the imaginary parts are discarded and the real parts combined, then this results after a second Fourier transformation in-

$$\mathrm{Re}[s(\omega_1,\omega_2)] = \mathrm{Abs}(\omega_1)\mathrm{Abs}(\omega_2) \qquad \text{Eqn. 5.35}$$

This final transformation is called the Hypercomplex Fourier Transformation.

2 Retention of Absorption Lineshapes with Sign Discrimination Using Complex Transformations[8]

The sine and cosine signals need to be kept separate. A processing procedure is applied to the sine and cosine two-dimensional data sets so that the sine function is an odd function. Therefore, the two resultant absorption-mode peaks will be negative so that upon recombination one of the peaks cancels, leaving only one peak. This enables frequency discrimination and maintains the pure absorption lineshape.

3 Real Fourier Transformation with Respect to t_1

This involves the use of Redfield's method of quadrature detection using one ADC (analog-to-digital-converter) or TPPI (time proportional phase increment) and is similar to the previous method in that combination of the points results in removal of the dispersive components.

5.3 The WISE (WIdeline SEparation) Experiment[4]

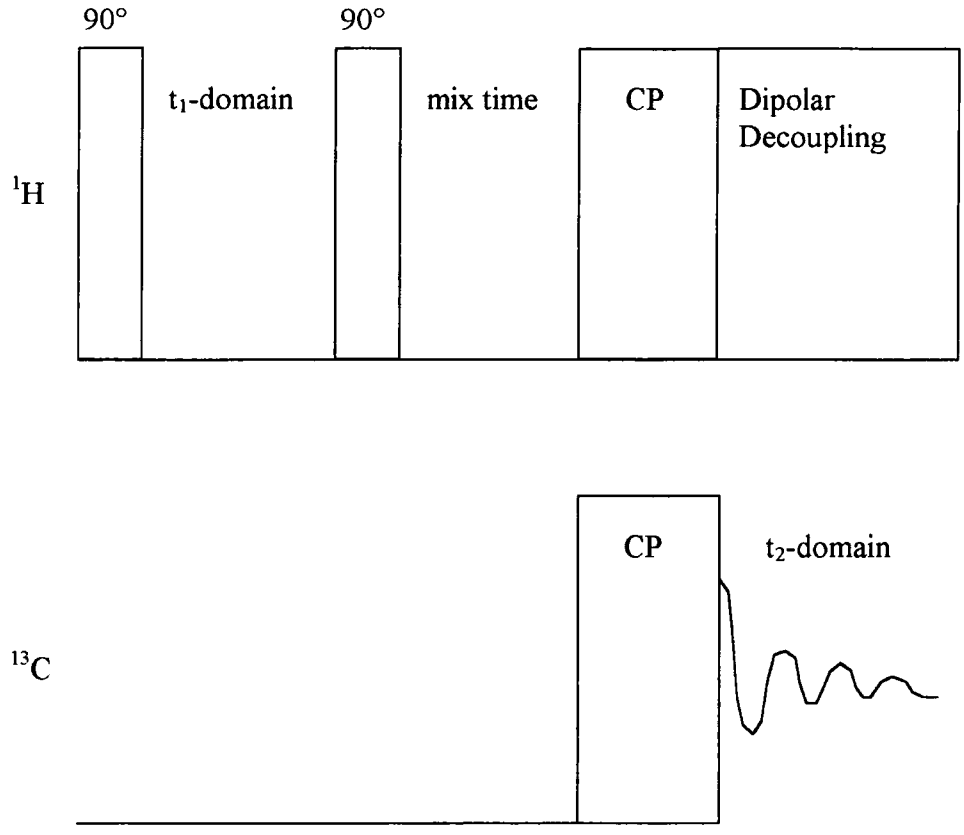

Fig. 5.8 Diagram of the WISE Pulse Sequence.

This experiment is used to try and observe the mobility of each polymer component as a function of proton linewidth at particular carbon resonances - hence the experiment is called the proton wideline separation experiment. The time denoted t_1 is set to probe the proton domain. The 'mix' time is set to try and watch the recovery of the faster decaying component's magnetisation through the mechanism of spin-diffusion (a particular dipolar interaction).

The sequence used on the CMX200 did have the time 'mix' involved within the sequence but was set to zero so as to not lose too much information about the faster decaying component's magnetisation. However, there are problems inherent to this sequence-

1 There is no quadrature detection in the t_1- or proton-dimension since only a sequence of point-amplitudes are detected. This results in phase and amplitude modulation within the second time-domain so that upon Fourier transformation the resulting lineshape has a phase-twist - Spectrum 5.8 (a combination of absorption and dispersive components in the proton-dimension lineshape).

There are several ways to overcome these problems

1) p- and n-type selection
2) quadrature detection using a Redfield shift
3) acquisition of hypercomplex data

The method of preference has been the determination of quadrature detection using the Redfield method. This is where two two-dimensional data sets are obtained with a 90° phase difference in the initial nutating pulse (or the same is obtained using a 90° phase difference in the spin-lock fields) between the two experiments. This results in detection of a cosine and sine periodic FID function. Combination of the two sets of data results in the cancellation of the imaginary parts of the data, so removing the problem of the phase-twist. This also helps maintain quadrature detection and so allows discrimination of the sign of the precession of the magnetisation.

Due to the dramatic difference in the rates of relaxation of the polystyrene and polybutadiene blocks under T_2 conditions the t_1-domain had a dwell time of 10 μs in order to show the full spectral width of the transformed polystyrene proton peaks (ca. 500 ppm). However, this results in truncation of the polybutadiene moiety signal and only samples a small number of data points for the polystyrene moiety in the FID. Due to the restrictions on spectrometer time the pulse delay (time between acquisitions) was dropped from 5 s to 3 s. This results in only a small amount of saturation. The t_1-domain only has 64 slices (points) so to get a more pleasing spectrum a multiplying factor of 4 was applied to increase the number of detected points. This was achieved by

Spectrum 5.8 WISE Spectrum of Polystyrene-b-polybutadiene Showing the Phase-twist. The solid lines represent positive peaks and the dotted lines represent the negative peaks.

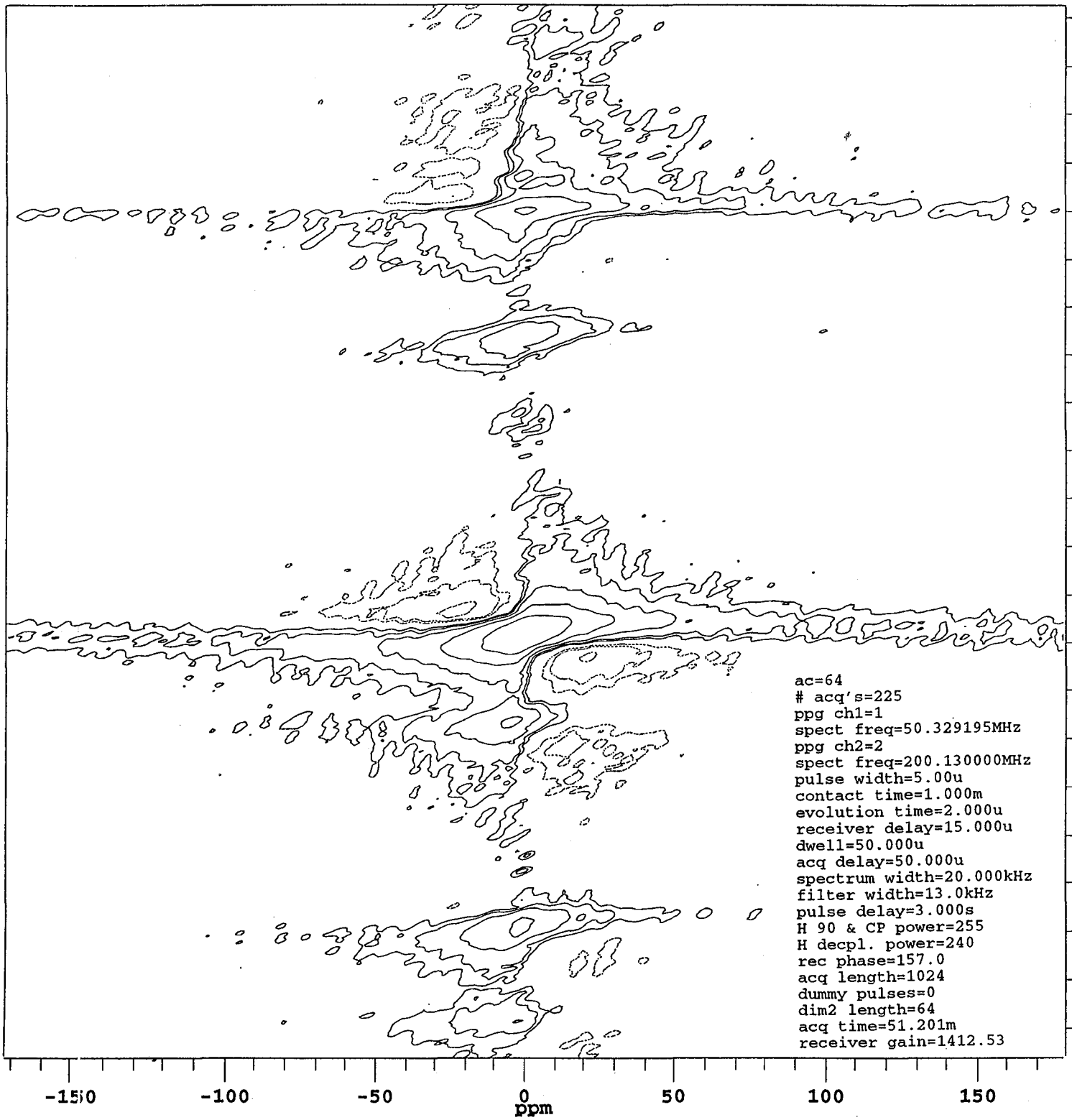

a process known as zero-filling, which literally just adds a series of zeros to the end of the FID in the proton-dimension.

There is also a well known distortion that occurs in two-dimensional spectroscopy[9]. The original continuous time signal is zero at negative times (before acquisition) and positive at time t = 0. Thus, there is a discontinuity that can lift the baseline or give spurious ridges in the two-dimensional spectrum (Spectrum 5.9). This is why the first data point is multiplied by 0.5 to reduce the magnitude of the discontinuity.

The first attempts in the use of this sequence relied on the use of acquiring a two-dimensional data set and deleting the imaginary component. Subsequently, the real components left had to be symmetrised around the carrier frequency to obtain a pure absorption mode in the second dimension - in this experiment it was the proton-dimension that was symmetrised. This method unfortunately resulted in the loss of information from the imaginary component of the non-transformed time-domain signal so the Redfield method has become the method of choice.

Inspection of the combined spectrum 5.10 shows that the proton-dimension is symmetrised. This means that the proton resonance detected from the sample is not distinguished from the spectrometer carrier frequency. This is not surprising since the spectral width of the proton-dimension (t_1-dimension) is 50 kHz. The signal obtained from the 90° shifted detector only contained noise hence proving there is no advantage in trying to maintain the imaginary component of the two-dimensional data set.

The resultant WISE spectra show that the mobility of the carbon atoms is probed in the proton-dimension and that the broad resonances in the proton-dimension are with the styrene carbons and the narrower linewidths are associated with the more mobile polybutadiene peaks. Spectra 5.11 shows cross sections of both the carbon- and proton-dimensions.

Analysis of the peak-widths-at-half-height ($\Delta\nu_{1/2}$) show more quantitatively the differences in mobility between the polystyrene and polybutadiene peaks in the ^{13}C spectrum. Using the equation-

Spectrum 5.9 WISE Spectrum Showing the Effect of not Using the First-point Multiplying Technique to Prevent Peak Baseline Distortions.

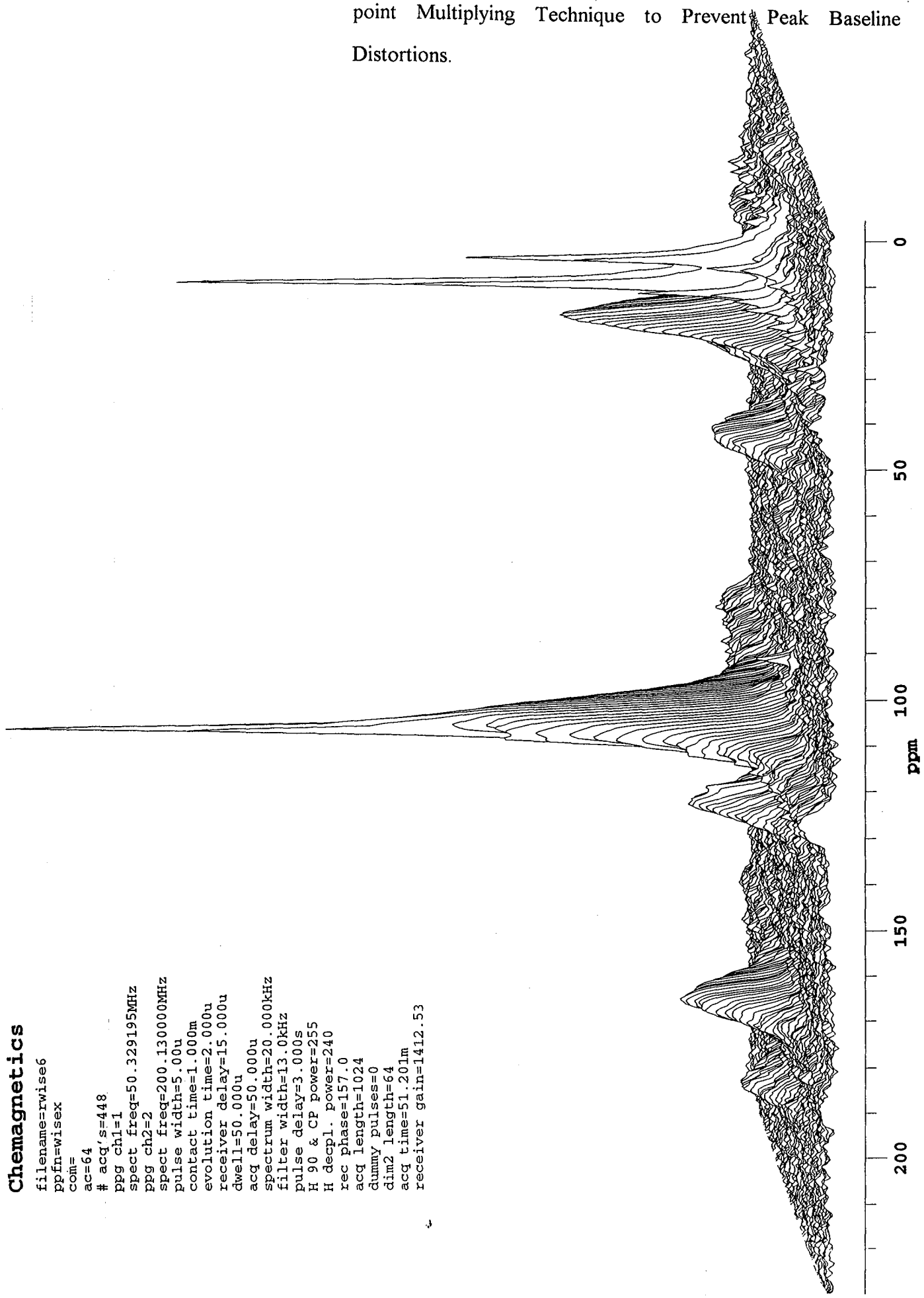

Spectrum 5.10 WISE Spectrum Using the Redfield Method of Phase Detection. The Scale Shown is of the ^{13}C-dimension.

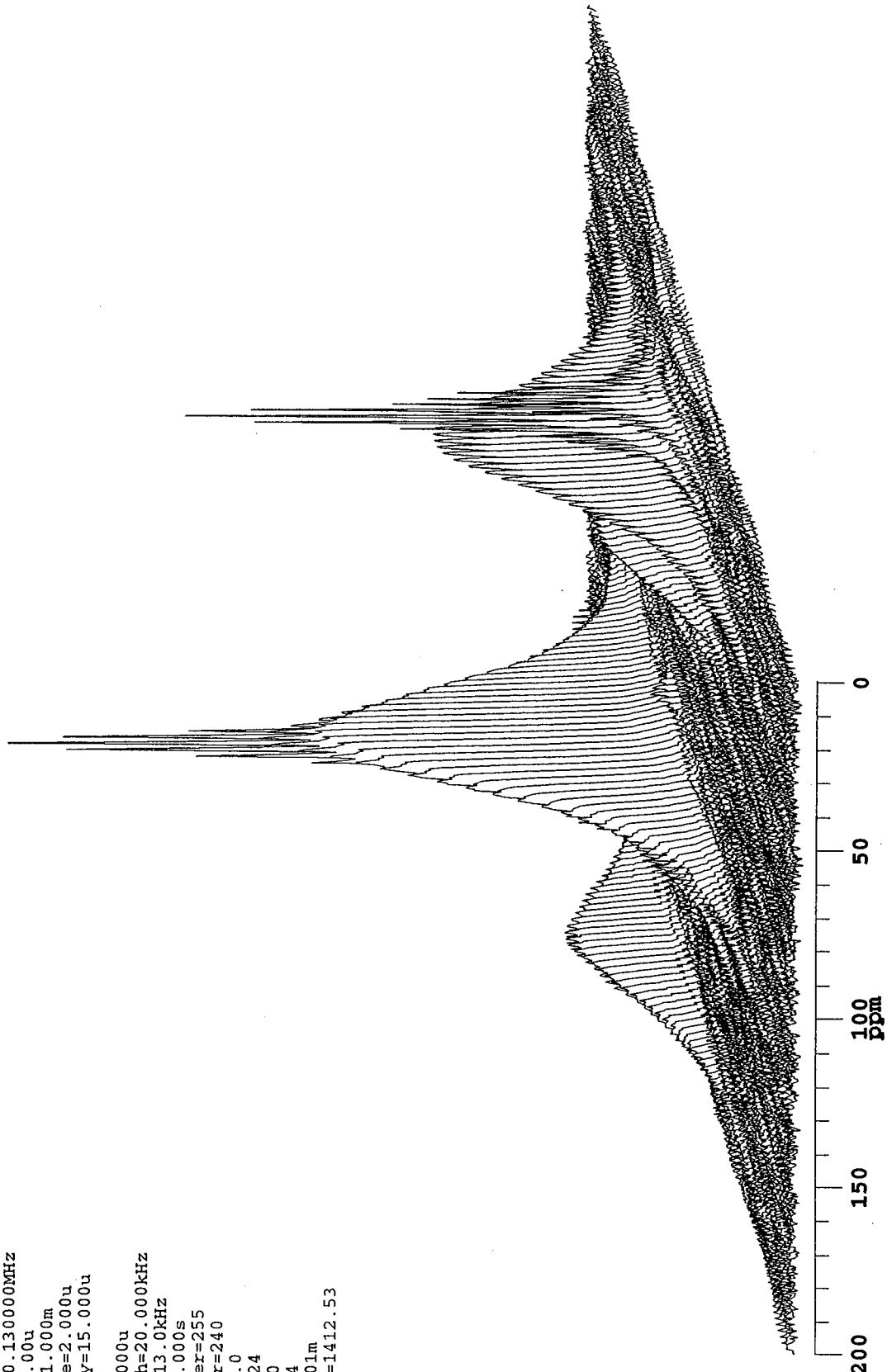


```
Chemagnetics
filename=rwise6
ppfn=wisex
com=
ac=64
# acq's=448
ppg ch1=1
spect freq=50.329195MHz
ppg ch2=2
spect freq=200.130000MHz
pulse width=5.00u
contact time=1.000m
evolution time=2.000u
receiver delay=15.000u
dwell=50.000u
acq delay=50.000u
spectrum width=20.000kHz
filter width=13.0kHz
pulse delay=3.000s
H 90 & CP power=255
H decpl. power=240
rec phase=157.0
acq length=1024
dummy pulses=0
dim2 length=64
acq time=51.201m
receiver gain=1412.53
```

Spectra 5.11 Selection of Proton- and Carbon-dimension Slices of Spectrum 5.11 Indicating the Differences in Peak-width-at-half-height for the Two Polymer Blocks.

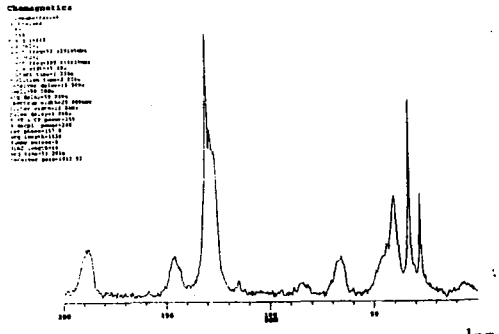

^{13}C Spectral Slice Through 0 ppm in the ^{1}H-dimension

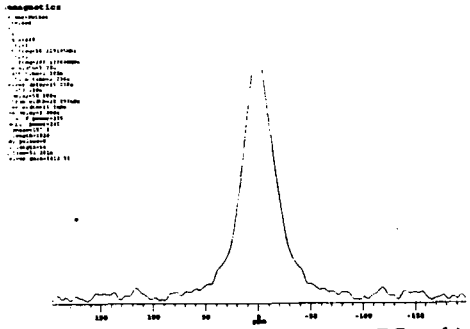

^{1}H Spectral Slice Through 10 ppm (PSt ssb) in the ^{13}C-dimension

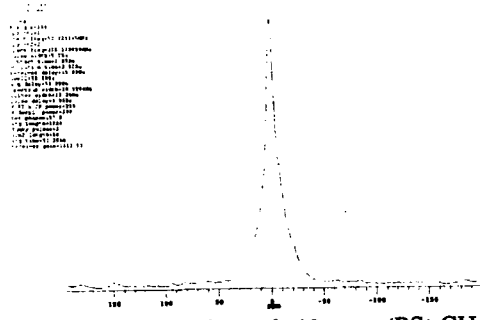

^{1}H Spectral Slice Through 40 ppm (PSt CH_2) in the ^{13}C-dimension

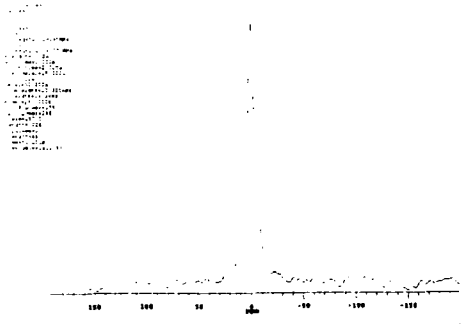

^{1}H Spectral Slice Through 30 ppm (cis PBd CH_2) in the ^{13}C-dimension

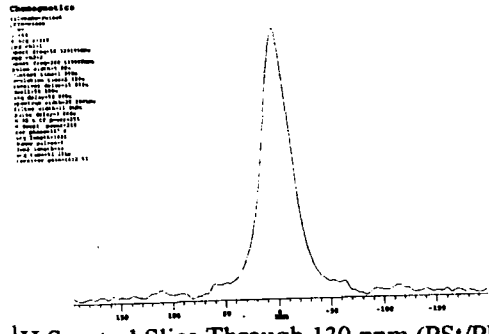

^{1}H Spectral Slice Through 130 ppm (PSt/PBd vinyl) in the ^{13}C-dimension

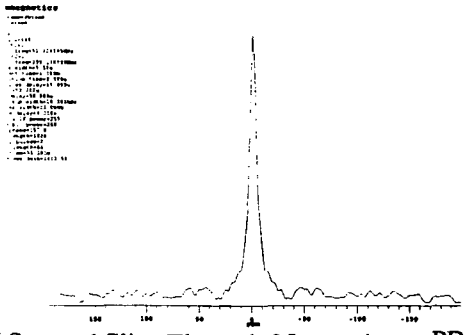

^{1}H Spectral Slice Through 35 ppm (trans PBd CH_2) in the ^{13}C-dimension

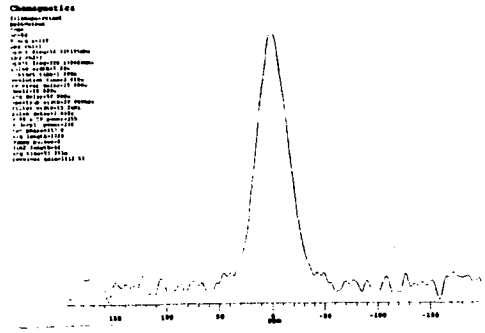

^{1}H Spectral Slice Through 145 ppm (PSt Quat.) in the ^{13}C-dimension

$$\Delta\nu_{1/2} = 1/\pi T_2 \qquad \text{Eqn. 5.36}$$

gives a relationship between the peak-width-at-half-height value for each proton linewidth and its corresponding spin-spin relaxation rate (and hence its mobility)[6]. Table 5.1 summarises the full linewidth analysis-

Peak (ppm)	$\Delta\nu_{1/2}$ (ppm)	$\Delta\nu_{1/2}$ (Hz)	T_2 (μs)
10 (PSt. ssb)	33.7	6754	47
30 (PBd. CH_2 cis)	7.5	1501	212
35 (PBd. CH_2 trans)	7.5	1501	212
40 (PSt. CH_2)	11.2	2251	141
130 (PSt./PBd. CH vinyl)	30	6004	53
145 (PSt. quaternary)	32.8	6566	48

Table 5.1 Summary of Linewidth Data from Spectrum 5.11 and Spectra 5.12 and their calculated T_2 relaxation times.

The CH polystyrene side-arm peak (45 ppm) has not been peak-picked due to the overlap with the CH_2 polystyrene peak at 40 ppm. The vinyl peaks of polystyrene and polybutadiene also overlap so were not individually peak-picked.

The T_2 values of the CH_2 polybutadiene peaks are no more accurate than the values from the delayed contact-time experiment since the modelling was inaccurate in the delayed contact-time experiment and a large degree of truncation results in the WISE spectrum for the polybutadiene peaks. The polystyrene T_2 values are double those in the delayed contact-time experiment and from the WRAC models. This may be due to the lack of acquired points for the polystyrene decay in the FID since the dwell time was 10 μs. Also, Eqn. 5.36 only models well Lorenztian lineshapes and poorly to broader Gaussian lineshapes as with the polystyrene peaks.

Unfortunately, due to time constraints, the effect of mixing time on the recovery of polystyrene peaks in the WISE experiment (from spin-diffusion) could not be completed and so a model of microdomain sizes in these copolymers was not deduced.

5.4 References

1 Mehring M., "Principles in High-Resolution NMR in Solids", Springer Verlag, Berlin, **1983**.

2 Stejkal E. ., Schaefer J. and Waugh J. S., *J. Mag. Res.*, **1977**, 28, P105.

3 Walther K. L., Wokaun A., 'Characterisation of Porous Silica Gels Prepared Via the Sol-Gel Process by ^{29}Si CP/MAS Solid-State NMR Spectroscopy', *Molecular Physics*, **1990**, 71, P760-780.

4 Schmidt-Rohr K., Clauss J. and Spiess H. W., 'Correlation of Structure, Mobility and Morphological Information in Heterogeneous Polymer Materials by Two-dimensional Wideline-separation NMR Spectroscopy', *Macromolecules*, **1992**, 25, P3273-3277.

5 Derome A. E., 'Modern NMR Techniques of Chemistry Research', Pergammon Press, Oxford, **1987**.

6 Homans W., 'A Dictionary of Concepts in NMR', Oxford University Press, **1991**.

7 Keeler J., Neuhaus D., 'Comparison and Evaluation of Methods for Two-Dimensional NMR Spectra With Absorption-Mode Lineshapes', *J. Mag. Res.*, **1985**, 63, P454-472.

8 States D. J., Haberkorn R. A. and Ruben D. J., ' A Two-Dimensional Nuclear Overhauser Experiment With Pure Absorption Phase In Four Quadrants', *J. Mag. Res.*, **1982**, 48, P286-292.

9 Ernst R. R., Bodenhausen G. and Wokaun A., 'Principles of NMR in One and Two Dimensions', Clarendon Press, Oxford, **1987**.